

Comparison of ^{13}CO Line and Far-Infrared Continuum Emission as a Diagnostic of Dust and Molecular Gas Physical Conditions:

I. Motivation and Modeling

W. F. Wall

*Instituto Nacional de Astrofísica, Óptica, y Electrónica, Apdo. Postal 51 y 216, Puebla,
Pue., México*

wwall@inaoep.mx

ABSTRACT

Determining temperatures in molecular clouds from ratios of CO rotational lines or from ratios of continuum emission in different wavelength bands suffers from reduced temperature sensitivity in the high-temperature limit. In theory, the ratio of far-IR, submillimeter, or millimeter continuum to that of a ^{13}CO (or C^{18}O) rotational line can place reliable upper limits on the temperature of the dust and molecular gas. Consequently, far-infrared continuum data from the *COBE/DIRBE* instrument and Nagoya 4-m ^{13}CO $J = 1 \rightarrow 0$ spectral line data were used to plot $240\ \mu\text{m}/^{13}\text{CO}$ $J = 1 \rightarrow 0$ intensity ratios against $140\ \mu\text{m}/240\ \mu\text{m}$ dust color temperatures, allowing us to constrain the multiparsec-scale physical conditions in the Orion A and B molecular clouds.

The best-fitting models to the Orion clouds consist of two components: a component near the surface of the clouds that is heated primarily by a very large-scale (i.e. $\sim 1\text{ kpc}$) interstellar radiation field and a component deeper within the clouds. The former has a fixed temperature and the latter has a range of temperatures that varies from one sightline to another. The models require a dust-gas temperature difference of $0\pm 2\text{ K}$ and suggest that 40-50% of the Orion clouds are in the form of dust and gas with temperatures between 3 and 10 K. These results have a number implications that are discussed in detail in later papers. These include stronger dust-gas thermal coupling and higher Galactic-scale molecular gas temperatures than are usually accepted, an improved explanation for the $\text{N}(\text{H}_2)/\text{I}(\text{CO})$ conversion factor, and ruling out one dust grain alignment mechanism.

Subject headings: ISM: molecules and dust — Orion

1. Introduction

Development of a complete theory of star formation requires understanding the physical conditions of the molecular gas in which stars form, both on sub-parsec and multi-parsec scales. On the latter size scales, observations of molecular clouds can provide insights into large-scale patterns of star formation such as in spiral arms, rings, or in starburst regions of external galaxies (e.g., see Rand et al. 1992; Vogel et al. 1988; Aalto et al. 1999; Kuno et al. 1995; Wong & Blitz 2000; Sheth et al. 2000; Seaquist et al. 1998; Kikumoto et al. 1998; Paglione et al. 1997; Güsten et al. 1993; Rieu et al. 1992; Wild et al. 1992; Harris et al. 1991; Tilanus et al. 1991; Turner et al. 1991; Verter and Rickard 1989; Lo et al. 1987; Sorai et al. 2000; García-Barrillo et al. 2000; Harrison et al. 1999; Wall et al. 1991; Sage et al. 1991; Scoville et al. 1985; Nishiyama and Nakai 2001; Nishiyama et al. 2001; Kennicutt 1989; Martin and Kennicutt 2001; Rownd & Young 1999; Bryant and Scoville 1999; Mulchaey and Regan 1997; Aalto et al. 1995; Wall et al. 1993; Puxley et al. 1990; Verter 1987, 1988). The diagnostics of molecular cloud physical, or excitation, conditions are usually obtained from observed molecular spectral lines. Despite being composed almost entirely of molecular hydrogen, only very warm ($\gtrsim \text{few} \times 100$ K) gas in interstellar molecular clouds is sampled *in emission* with the purely rotational lines of H_2 (Rodríguez-Fernández et al. 2001; Rosenthal et al. 2000; Wright et al. 1999; Parmar et al. 1991) and the ro-vibrational lines sample even warmer ($\gtrsim 2000$ K) or fluorescently excited H_2 (e.g., Takami et al. 2000; Fuente et al. 1999; Moorwood and Oliva 1990, 1988; Black and van Dishoeck 1987). This is because the purely rotational transitions are quadrupolar and only occur between widely spaced ($h\nu/k \geq 510$ K) levels (for a more detailed discussion, see Wall 1999, and references therein). Consequently, estimating the properties of the bulk of the molecular gas, which is cold (kinetic temperatures of $\sim 5\text{--}20$ K, see, e.g., Sanders et al. 1985), requires observing lines of trace molecules with dipole transitions and closely spaced levels. The molecule CO and its isotopologues, like ^{13}CO and C^{18}O , are the usual molecules of choice for estimating the large-scale properties of molecular clouds, because the most common isotopologue of CO — $^{12}\text{C}^{16}\text{O}$ — is the most abundant molecule after H_2 , the levels are closely spaced ($h\nu/k = 5.5$ K for $J = 1 \rightarrow 0$ of $^{12}\text{C}^{16}\text{O}$), and the critical density of the lowest transition is low (i.e. $n(\text{H}_2) \simeq 3 \times 10^3 \text{ cm}^{-3}$ for $J = 1 \rightarrow 0$). These characteristics of CO ensure that the lines are often strong — with radiation temperatures or T_{R} (i.e., Rayleigh-Jeans brightness temperatures as opposed to Planck brightness temperatures) of a few Kelvins — for $^{12}\text{CO } J = 1 \rightarrow 0$ observations of clouds in our Galaxy, (e.g., Sanders et al. 1985) and occur throughout most of the molecular ISM. Observations of lines of other molecules are also important for coming to a holistic picture of molecular clouds. For example, the rotational lines of CS sample the dense gas ($n(\text{H}_2) \gtrsim 10^5 \text{ cm}^{-3}$) most directly associated with star formation (Lada 1992). Nevertheless, because the rotational lines of CO sample the

excitation conditions in the bulk of the molecular gas, these lines provide insights into the environment in which the star-forming dense gas exists and, consequently, providing insights into star formation on the scales of many parsecs. Multi-parsec-scale observations of the lines of CO and its isotopologues, ^{13}CO and C^{18}O , are carried out on external galaxies (e.g., see the references listed near the beginning of this paragraph) or by low-resolution (few arcminutes), wide-coverage (many degrees) mapping of Galactic molecular clouds (e.g., see Lee et al. 2001; Dame et al. 2001, 1987; Dame and Thaddeus 1994; Grabelsky et al. 1988; Bronfman et al. 1988; Cohen et al. 1986; Sakamoto et al. 1995; Robinson et al. 1988; Sanders et al. 1984; Tachihara et al. 2000; Mizuno et al. 1998; Kawamura et al. 1998; Heyer et al. 1998; Boulanger et al. 1998; Onishi et al. 1996; Oka et al. 1998; Nagahama et al. 1998; Sakamoto et al. 1997a, 1994; Bally et al. 1987; Maddalena et al. 1986).

Besides the usually observed main isotopologue ^{12}CO (written this way to explicitly distinguish it from the rarer isotopologues), the lines of the rarer isotopologues ^{13}CO (short for $^{13}\text{C}^{16}\text{O}$) and C^{18}O (short for $^{12}\text{C}^{18}\text{O}$) furnish very important additional information on molecular cloud structure. The lower-J lines of ^{12}CO are often optically thick and cannot probe deeply into the substructures, such as clumps or filaments, of molecular clouds. Also, the opacity of the ^{12}CO lines reduces their sensitivity to the effects of changing density and changing radiative trapping. Therefore, the lines of ^{13}CO or C^{18}O are crucial for realistically constraining the molecular cloud excitation conditions, because these lines, being from lower abundance isotopologues, are often optically thin on multi-parsec scales. This greater sensitivity of the ^{13}CO and C^{18}O lines to cloud structure and physical properties makes them capable of identifying interesting regions within molecular clouds. Of particular interest is locating regions of warm (e.g., $\gtrsim 50\text{--}100\text{ K}$) molecular gas, because energetic events and massive stars associated with recent star formation heat the surrounding molecular gas. Such gas is sometimes identified from ratios of strengths of CO rotational lines (e.g., Wilson et al. 2001; Plume et al. 2000; Howe et al. 1993; Graf et al. 1993, 1990; Boreiko and Betz 1989; Fixsen et al. 1999; Harris et al. 1985; Harrison et al. 1999; Wall et al. 1991; Güsten et al. 1993; Wild et al. 1992; Harris et al. 1991).

Examples of how two of the line ratios involving the three lowest rotational lines of CO vary with gas kinetic temperature, T_{K} , in local thermodynamic equilibrium or LTE are shown in Figure 1. All the curves in Figure 1 show the same trend: the line ratios lose their sensitivity to T_{K} in the high- T_{K} , or Rayleigh-Jeans, limit. This is a consequence of the line ratios depending on ratios of two Planck functions at different frequencies. The maximum T_{K} to which a given line ratio is sensitive can be quantified by adopting a calibration uncertainty for the line ratios. If we adopt the optimistic value of 20% for the uncertainties in the ratios, then a ratio that has an observed value $\simeq 80\%$ of its asymptotic value in the Rayleigh-Jeans limit is observationally indistinguishable from this asymptotic value. Similarly, the value of

the kinetic temperature at this 80% level is the maximum kinetic temperature for which the given ratio is sensitive. Two important conclusions can be drawn from the plots of Figure 1:

1. Optically thin lines, like those of ^{13}CO , have a greater range of sensitivity to T_{K} than do optically thick lines, like those of ^{12}CO . Specifically, $T_{\text{R}}(J = 2 \rightarrow 1)/T_{\text{R}}(J = 1 \rightarrow 0)$ loses T_{K} sensitivity above 46 K in the optically thin case and above 10 K in the optically thick case.
2. Ratios involving higher-J lines have a greater range of temperature sensitivity than those with lower-J lines. For $T_{\text{R}}(J = 3 \rightarrow 2)/T_{\text{R}}(J = 2 \rightarrow 1)$ the maximum T_{K} values are 73 K and 13 K for the optically thin and thick cases respectively. These values are higher than the corresponding values for the $T_{\text{R}}(J = 2 \rightarrow 1)/T_{\text{R}}(J = 1 \rightarrow 0)$ ratio, especially for the optically thin case.

It is clear then that unambiguous identification of warm molecular gas requires observations of high-J lines of ^{12}CO and, sometimes, the optically thin lines of ^{13}CO (see references cited at the end of the previous paragraph). (It should be mentioned that simply observing the optically thick lines of ^{12}CO does not automatically give the kinetic temperature, because the observed lines are not necessarily thermalized and the gas does not necessarily fill the beam in the velocity interval about the line peak.)

However, identifying warm gas in this manner can be complicated. One complication is that observing higher and higher lines up the rotational ladder becomes increasingly difficult with ground-based observations, because the atmosphere becomes increasingly opaque, on average, and because sub-millimeter receivers become increasingly noisier with decreasing observational wavelength. Another complication is that non-LTE effects become more important higher in the rotational ladder: distinguishing between the density effects on the line ratios and kinetic temperature effects becomes difficult. One way to separate such effects is to observe many CO rotational lines, but this can be observationally intensive — especially if high-J ^{13}CO lines are also observed. Another approach to finding warm gas is using the $^{12}\text{CO}/^{13}\text{CO}$ intensity ratio. This ratio is very sensitive to the molecular gas kinetic temperature in the LTE, high- T_{K} limit. For example, the $^{12}\text{CO } J = 1 \rightarrow 0 / ^{13}\text{CO } J = 1 \rightarrow 0$ intensity ratio in LTE goes like T_{K}^2 to within 25% for $T_{\text{K}} \geq 20$ K. While the advantage of this ratio is that it only requires two lines with very similar frequencies, the considerable disadvantage is that the ^{12}CO and ^{13}CO lines occur in very different optical depth regimes. This results in three problems. One is that the ^{12}CO line will be effectively probing a different volume of gas from that of the ^{13}CO line. Another is that the levels of radiative trapping will be very different between the ^{12}CO and ^{13}CO lines, resulting in some sensitivity to density for the $^{12}\text{CO}/^{13}\text{CO}$ intensity ratio. The third problem caused by the very different opacities in the

^{12}CO and ^{13}CO lines is that the $^{12}\text{CO}/^{13}\text{CO}$ intensity ratio will have some dependence on gas column density; indeed, in LTE this ratio is the inverse of the optical depth of the ^{13}CO line (for the ^{12}CO line in the optically thick limit and ^{13}CO in the optically thin limit). While the problems above are not necessarily prohibitively difficult, it would be helpful nonetheless to have two optically thin tracers with very different dependences on temperature, with relative insensitivity to gas density, and that are ubiquitous in the molecular ISM. The use of such tracers would complement the use of lines of CO and of other molecules in diagnosing the presence of warm molecular gas simply and unambiguously.

Another way to trace molecular gas, and interstellar gas in general, is to observe the continuum emission from the dust grains found throughout most of the ISM. This continuum emission is usually observed at mid-IR, far-IR, submillimeter, and millimeter wavelengths. On parsec scales, dust continuum emission is usually optically thin for wavelengths $\gtrsim 15\ \mu\text{m}$. All-sky surveys like IRAS and *COBE/DIRBE* cover specific IR wavelengths from the mid-IR to far-IR and near-IR to far-IR, respectively (IRAS Explanatory Supplement 1988; *COBE/DIRBE* Explanatory Supplement 1998). Surveys at such wavelengths in the continuum are valuable for probing the structure and excitation of the ISM (see, for example, Dupac et al. 2000; Wall et al. 1996; Bally et al. 1991; Zhang et al. 1989; Werner et al. 1976; Heiles et al. 2000; Reach et al. 1998; Boulanger et al. 1998; Lagache et al. 1998; Goldsmith et al. 1997; Sodroski et al. 1994; Boulanger et al. 1990; Sellgren et al. 1990; Scoville & Good 1989; Sodroski et al. 1989; Leisawitz & Hauser 1988). Ratios of continuum intensities at different wavelengths, for instance, can constrain estimates of dust grain temperatures. A physical model that includes dust-gas thermal coupling could then, in theory, constrain gas temperatures (e.g., Weingartner & Draine 2001; Mochizuki & Nakagawa 2000; Hollenbach 1989; Tielens & Hollenbach 1985; Burke & Hollenbach 1983). Optically thin dust continuum intensity is $\tau_\nu B_\nu(T_d)$, where τ_ν is the optical depth at frequency ν , and $B_\nu(T_d)$ is the Planck function evaluated at frequency ν and dust temperature, T_d . In the far-infrared, the optical depth is often approximated as a power-law $\tau_\nu \propto \nu^\beta$, where the emissivity index β depends on the size and optical properties of the grains. Consequently, as with CO rotational lines, the ratio of continuum intensities at different wavelengths loses sensitivity to dust temperature in the Rayleigh-Jeans limit. As an example, we will consider the ratio of continuum intensities (per unit frequency) at the wavelength of $450\ \mu\text{m}$ to that at $850\ \mu\text{m}$, i.e. $I_\nu(450\ \mu\text{m})/I_\nu(850\ \mu\text{m})$, and adopt a 20% calibration uncertainty for this ratio. We will also adopt $\beta = 2$, which is a reasonable number for wavelengths longer than about $100\ \mu\text{m}$ (Andriesse 1974; Seki & Yamamoto 1980; Wall et al. 1996). These adopted values imply that the $I_\nu(450\ \mu\text{m})/I_\nu(850\ \mu\text{m})$ ratio loses sensitivity to dust temperature for $T_d > 37\ \text{K}$ (again from adopting 80% of the asymptotic value in the Rayleigh-Jeans limit). This maximum T_d can be improved by roughly a factor of 2 by combining the $450\ \mu\text{m}$ observations

with observations at wavelengths longer than $850\,\mu\text{m}$, but real improvement over this 37 K limit requires observations at wavelengths even shorter than $450\,\mu\text{m}$. Observations at such short wavelengths must deal with increased atmospheric opacity and sometimes must be space-based (e.g., IRAS and *COBE*).

A more direct ground-based approach is suggested by the work of Schloerb et al. (1987), who show that a direct comparison of optically thin CO line emission with submillimeter continuum can provide temperature estimates of the dust and molecular gas in molecular clouds (see also Swartz et al. 1989). Schloerb et al. (1987) derive an expression for the sub-millimeter continuum to integrated C^{18}O $J = 1 \rightarrow 0$ line strength ratio, $I_\nu(\text{submm})/I(\text{C}^{18}\text{O } J = 1 \rightarrow 0)$, which goes like $T_K T_d$ in the high-temperature limit. For similar gas and dust temperatures, this means that the $I_\nu(\text{submm})/I(\text{C}^{18}\text{O } J = 1 \rightarrow 0)$ ratio and, similarly, the $I_\nu(\text{submm})/I(^{13}\text{CO } J = 1 \rightarrow 0)$ ratio are actually *more sensitive to temperature as that temperature increases*. This is in stark contrast to ratios of rotational lines of a given isotopologue of CO and to ratios of continuum intensities at different frequencies, which, as discussed above, *lose* sensitivity to temperature in the high-temperature limit. In addition, comparing the continuum intensity with that of a low-J line like the $J = 1 \rightarrow 0$ line of ^{13}CO (or of C^{18}O) reduces the sensitivity of the continuum-to-line ratio to gas density. In short, the intensity ratio of the submillimeter continuum to an optically thin CO line may be the sought-for alternative diagnostic of molecular gas temperature that was mentioned above.

Despite the potential diagnostic advantages of the continuum-to-line ratio [e.g., $I_\nu(\text{submm})/I(^{13}\text{CO } J = 1 \rightarrow 0)$], interpretation of this ratio and its spatial variations assumes the following:

- *The ratio of the mass of ^{13}CO to that of dust does not vary spatially.* Even though the gas-to-dust mass ratio may vary, the ^{13}CO -to-dust mass ratio may not vary significantly within a single source, but may vary by up to an order of magnitude from source to source (Swartz et al. 1989).
- *The gas along a given line of sight is predominantly molecular.* Appreciable quantities of atomic or ionized gas and their associated dust would complicate the interpretation of $I_\nu(\text{submm})/I(^{13}\text{CO } J = 1 \rightarrow 0)$. This is because the submillimeter continuum emission would *not* originate in dust *only* associated with molecular gas, but the ^{13}CO emission *would* originate only from the molecular gas. Consulting HI 21-cm and radio continuum data can check this assumption.
- *The molecular gas density does not vary spatially.* If this assumption is false, then spatial gradients in the $I_\nu(\text{submm})/I(^{13}\text{CO } J = 1 \rightarrow 0)$ ratio may be probing spatial

gradients in the molecular gas density rather than in the molecular gas temperature. Again, observing the lower-J rotational lines of ^{13}CO , especially the $J = 1 \rightarrow 0$, line can minimize this problem.

- *The gas and dust temperatures have spatial gradients in the same direction.* Even if $T_{\text{K}} \neq T_{\text{d}}$, only assuming that the spatial gradients are in the same direction for both T_{K} and T_{d} is necessary. This is reasonable since both gas and dust are cooler with greater distance from heating sources, especially on multi-parsec scales.
- *Dust grain properties, like the dust mass absorption coefficient ($\kappa_{\text{d}\nu}$) and emissivity index (β), do not vary spatially.* Observations of Orion, for example, show that such variations do occur for β on sub-parsec scales (e.g., Johnstone & Bally 1999), but, to first order, adopting a single value on multi-parsec scales is possible.
- *The ^{13}CO line used in the comparison is truly optically thin.* If the ^{13}CO line opacity varies from optically thin to optically thick, the $I_{\nu}(\text{submm})/I(^{13}\text{CO})$ ratio would again show gradients. The cause of the opacity change could still be due to a change in temperature, but it could also be due to a change in column density (and even volume density). Observing the corresponding C^{18}O line can test this.
- *There is no temperature gradient along the line of sight.* Such a gradient would result in the submillimeter emission being biased toward the warmer regions along the line of sight and the ^{13}CO emission much less so biased (and even biased toward the colder regions if LTE applies). Even in the hypothetical case of $T_{\text{K}} = T_{\text{d}}$ at every point along the line of sight, these biases could lead the observer, armed with observations at additional frequencies, to believe that $T_{\text{K}} \neq T_{\text{d}}$. This could also lead to the erroneous result that comparisons from one line of sight to another show no coupling between gas and dust temperatures. The effects of gradients along the line of sight can be minimized by observing clouds on multi-parsec scales, where such gradients would be less extreme.
- *Thermal and non-thermal gas emission make a negligible contribution to the submillimeter continuum.* This should indeed be the case. In M 82, for example, Thronson et al. (1989) estimate that $\sim 30\%$ of the $1300\text{ }\mu\text{m}$ flux in the central $30\text{--}45''$ is due to gas emission. This would be even less at shorter wavelengths and in regions with no dominant supernova remnants nor HII regions.

These assumptions may be reasonable first approximations for observations on multi-parsec scales or, depending on the assumption, can be tested for each source observed.

Testing the overall validity of the above assumptions and, as a result, the behavior and effectiveness of the $I_\nu(\text{submm})/I(^{13}\text{CO})$ ratio as a diagnostic of molecular cloud physical conditions requires maps of a molecular cloud in the submillimeter or far-infrared (FIR) continuum, in the $^{13}\text{CO } J = 1 \rightarrow 0$ or $\text{C}^{18}\text{O } J = 1 \rightarrow 0$ spectral lines, and of dust or gas temperatures, all with resolutions at multi-parsec scales. The most reliable maps of temperatures associated with molecular clouds would be from ratios of FIR maps. Ignoring certain complications for the moment, such as line-of-sight gradients in dust properties (e.g., T_d), uncertainties in those properties (e.g., β), and dust grains *not* in thermal equilibrium, the ratio of the intensities of FIR maps at two different wavelengths gives reliable dust temperatures because such intensities are in the Wien limit of the Planck function. In this limit, the dust temperature derived from the observed intensity ratio is insensitive to that ratio. For example, the observed continuum intensity ratio of $I_\nu(140 \mu\text{m})/I_\nu(240 \mu\text{m}) = 1.66$ would imply $T_d = 20 \text{ K}$. A 10% uncertainty in that intensity ratio would imply only a 5% uncertainty in the derived dust temperature (or $\pm 1 \text{ K}$). One complication, that of stochastically-heated dust grains (i.e., grains *not* in thermal equilibrium), can be effectively avoided by using two FIR maps at wavelengths of $\gtrsim 100 \mu\text{m}$ (for example, see Désert et al. 1990; Wall et al. 1996). This, therefore, rules out using IRAS maps, whose nominal wavelengths do not go beyond $100 \mu\text{m}$. On the other hand, maps from the *DIRBE* instrument aboard the *COBE* spacecraft cover the whole sky in ten IR bands from $1.25 \mu\text{m}$ out to $240 \mu\text{m}$ (*COBE/DIRBE* Explanatory Supplement 1998). Two maps are at nominal wavelengths of longer than $100 \mu\text{m}$ (i.e., $140 \mu\text{m}$ and $240 \mu\text{m}$), making them virtually free of emission from stochastically-heated grains. Thus the *DIRBE* maps at $140 \mu\text{m}$ and $240 \mu\text{m}$ and their ratio can be compared with a map of $^{13}\text{CO } J = 1 \rightarrow 0$ (or $\text{C}^{18}\text{O } J = 1 \rightarrow 0$ if available) of a given molecular cloud. Maps of entire clouds in our Galaxy in $^{13}\text{CO } J = 1 \rightarrow 0$ have recently become available (e.g., see Lee et al. 2001; Mizuno et al. 1998; Kawamura et al. 1998; Nagahama et al. 1998). Therefore, the observational data exist to test the sensitivity and reliability to molecular cloud physical conditions of the ratio of the submillimeter or FIR continuum to ^{13}CO line intensities.

The appropriate molecular cloud, or clouds, for which this testing should be applied must satisfy a number of criteria:

- The test clouds should be bright in the desired tracers (i.e., FIR and ^{13}CO) and completely or nearly completely mapped in these tracers,
- largely mapped in tracers of atomic and ionized gas, such as HI 21-cm and radio continuum,
- out of the Galactic plane to reduce confusion with foreground and background material,

- several degrees in extent so as to accommodate many beams of the large *DIRBE* beam (0.7°),
- and should have as large a range of dust temperatures as possible at the *DIRBE* resolution.

The clouds of Orion most closely satisfy these criteria (see, e.g., Bally et al. 1991; Wall et al. 1996; Nagahama et al. 1998; Zhang & Green 1991; Green 1991; Chromey et al. 1989; Heiles & Habing 1974; Reich 1978; Berkhuijsen 1972; Haslam et al. 1970). While there are other clouds that *may seem* to satisfy these criteria as well (e.g., Chamaeleon-Musca, Mizuno et al. 1998), the Orion clouds have the largest range of dust temperatures at the *DIRBE* resolution (see Figure 2 of Lagache et al. 1998). The Orion A and B molecular clouds are bright in ^{13}CO $J = 1 \rightarrow 0$ (Nagahama et al. 1998), and in the FIR continuum at $140\,\mu\text{m}$ and $240\,\mu\text{m}$ (Wall et al. 1996), and has been completely or largely mapped in these tracers. Much of the Orion constellation has been mapped in HI (Zhang & Green 1991; Green 1991; Chromey et al. 1989; Heiles & Habing 1974) and radio continuum (Reich 1978; Berkhuijsen 1972; Haslam et al. 1970), thereby permitting tests of whether or not molecular gas dominates the cloud surface, or column, density for each line of sight. Much of Orion has also been mapped in ^{12}CO lines (Wilson et al. 2005; Lang et al. 2000; Ikeda et al. 1999; Sakamoto et al. 1997a, 1994; Maddalena et al. 1986), which can also provide crude estimates of the molecular gas column densities. Note that only Maddalena et al. (1986) have mapped the Orion all three major clouds: Orion A, Orion B and the λ Orionis ring. The Orion clouds are about $15\text{--}20^\circ$ out of the Galactic plane and about $6^\circ \times 3^\circ$ (or about $50\text{ pc} \times 25\text{ pc}$ for an adopted distance of 450 pc) in size, down to some ill-defined zero level. An additional advantage to the clouds of Orion is that these clouds have been surveyed at many other wavelengths on the scales of many parsecs, thereby providing further checks on models. These other wavelengths include, for example, the optical surveys of the Orion OB1 and λ Ori OB associations (Brown et al. 1995, 1994; Warren & Hesser 1978, 1977; Murdin & Penston 1977; Blaauw 1964), the near-IR to far-IR all-sky survey of *COBE/DIRBE* (Wall et al. 1996), the mid-IR to far-IR all-sky survey of IRAS (Bally et al. 1991), and submillimeter maps of small sections of Ori A and B (e.g., Johnstone et al. 2001; Mitchell et al. 2001; Johnstone & Bally 1999). Therefore, the Orion A and B molecular clouds were chosen for testing the behavior of the $I_\nu(\text{submm})/I(^{13}\text{CO})$ ratio, using the *DIRBE* maps at $140\,\mu\text{m}$ and $240\,\mu\text{m}$ and the ^{13}CO $J = 1 \rightarrow 0$ data of Nagahama et al. (1998).

The current paper, or Paper I, describes the one- and two-component modeling of the data. Paper II (Wall 2006) in this series confirms and, in some cases, modifies the model results using simulated data. Paper III (Wall 2006a) examines systematic effects not explicitly considered in the models and also discusses the scientific implications of the results.

2. Data Processing

2.1. DIRBE Data

Details of the *COBE* mission and *DIRBE* instrument can be found in Bogges et al. (1992), Silverberg et al. (1993), Hauser et al. (1998), and the *COBE/DIRBE* Explanatory Supplement (1998). Much in this section has been discussed in Wall et al. (1996) (hereafter referred to as W96) in Section 2.1 of that paper. The data in the current paper are from the 1998 release, whereas the data of W96 were of the 1993 release. Also, the current paper concentrates on Bands 9 (i.e. $\lambda = 140 \mu\text{m}$) and 10 ($\lambda = 240 \mu\text{m}$), while W96 discussed all 10 wavelength bands. Consequently, the data processing in this section largely concerns the maps in the $140 \mu\text{m}$ and $240 \mu\text{m}$ bands from the 1998-release of the *DIRBE* data.

While a number of *DIRBE* data products are available, the ZSMA (Zodi-Subtracted Mission Averaged) maps were the most relevant for the current research. (See the *COBE/DIRBE* Explanatory Supplement 1998, for more details of the *DIRBE* data products described in this paragraph.) These maps are the average sky brightnesses determined from averaging over the full 40 weeks of the *COBE* mission, thereby maximizing the signal-to-noise ratio of the data. Maximizing the signal-to-noise ratio is particularly important for the $140 \mu\text{m}$ and $240 \mu\text{m}$ bands, because these have the noisiest data. The average sky brightness in each wavelength band was determined after removal of the *DIRBE* interplanetary dust model for each of the ten wavelength bands, which effectively removes the zodiacal emission from the maps. The ZSMA maps are available in the form of FITS tables that include the pixel number, the intensity in that pixel in MJy/sr, and the noise in that pixel in MJy/sr. The FITS tables were converted into maps in the equal-area Mollweide projection using IDL routines available from NASA/GSFC through the worldwide web. The fxbopen and fxbread routines were used to open the FITS files and read in the data, respectively. The data included the pixel numbers, sky brightnesses, and noise levels. The pix2xy routine was used to create maps from the data in the *DIRBE* sky-cube format. This was followed by converting the sky-cube maps to maps in the Mollweide projection using the reproj routine. Maps of both the sky brightnesses and of the rms noise levels were created this way. The maps of the rms noise levels are hereafter referred to as the sigma maps.

After the creation of the Mollweide maps using the IDL routines from NASA/GSFC, the section of the all-sky maps corresponding to the Orion region was extracted. As was done in W96, a cosecant-law background of the form $a_{\text{csc}}(|b|)$ was subtracted from the sky-brightness maps, so as to remove foreground and background emission associated with the Galactic plane. The fitting procedure was virtually identical to that used in W96 with a slight change in the algorithm used to determine the Galactic latitude b from the pixel

position. The earlier paper used a simplistic linear interpolation for determining b in the cosecant-law fitting routine. The current paper uses the exact expression that was used in creating the maps in the Mollweide projection. Nevertheless, over the latitude range of the Orion maps (i.e. $b = -5$ to -31°), the improvement in the algorithm only contributes a 4% change to the scale factors, a_c . As stated in W96, the uncertainties in the map intensities due to the uncertainty in the background subtraction is about 10%. The effects of this subtraction on the results will be discussed in Paper II (Wall 2006).

These Orion maps were compared with those of the 1993 release of the *DIRBE* data. The brightnesses of the 140 and 240 μm maps were reduced by about 15% with respect to those of the 1993 maps made. Accordingly, luminosities and masses determined from these maps are also reduced by this amount. However, the 140 μm /240 μm dust color temperatures are virtually unchanged.

Before creating maps of the 140 μm /240 μm dust color temperatures, the 140 μm and 240 μm maps were smoothed, as was done in W96. Without smoothing these maps, the resultant dust temperature map appears to be very choppy: noticeable, large, and random variations that occur within a beam size. The maps were smoothed with a square flat-topped box that was 3 pixels \times 3 pixels in width. Since the *DIRBE* beam size is roughly the same size (about 2.3 pixels \times 2.3 pixels) and shape, the equivalent resolution after smoothing is roughly $\sqrt{2}$ larger than the original 42' or about 1°. The resultant maps of $I_\nu(140 \mu\text{m})$ and $I_\nu(240 \mu\text{m})$ are shown in Figure 2.

As with the intensity maps, the corresponding sigma maps must also be smoothed. Here, however, the smoothing procedure is not so straightforward. Suppose the smoothing box is n_x pixels \times n_y pixels and I_{ij} is the intensity at pixel ij in the unsmoothed map. Then the intensity in the smoothed map at the central pixel of the smoothing box, I_s , is

$$I_s = \frac{1}{N} \sum_{i=1}^{n_x} \sum_{j=1}^{n_y} I_{ij} \quad , \quad (1)$$

where $N = n_x n_y$ is the total number of pixels in the smoothing box. If the pixels are independent, then the rms noise level in the smoothed map at the central pixel of the smoothing box, σ_s , is

$$\sigma_s^2 = \frac{1}{N^2} \sum_{i=1}^{n_x} \sum_{j=1}^{n_y} \sigma_{ij}^2 \quad . \quad (2)$$

However, if the I_{ij} are already convolved with a beam the same size and shape as the smoothing box (i.e. n_x pixels \times n_y pixels), then σ_s can be approximated by

$$\sigma_s^2 = \frac{1}{2N} \sum_{i=1}^{n_x} \sum_{j=1}^{n_y} \sigma_{ij}^2 \quad . \quad (3)$$

Equation (2) states that the noise in the smoothed map is a factor \sqrt{N} below the quadrature average of the noise levels in the smoothing box. This is expected when the pixels are independent because the random walk applies. On the other hand, equation (3) states that the noise in the smoothed map is only a factor of $\sqrt{2}$ below the quadrature average of the noise levels in the smoothing box. This is because the area of the effective beam is roughly doubled (exactly doubled in the case of Gaussian smoothing and a Gaussian beam) after convolution with a smoothing box the same size as the original beam. Equation (3) has been tested with simulated maps of random noise. After discarding pixels along the map edges, it was found that for 99.9% of the pixels equation (3) must be either corrected downward or upward by up to 30%. This is not a large correction to random noise estimates. Therefore, equation (3) was used in smoothing the sigma maps.

The map of the dust color temperatures (which is the actual dust grain temperature for the large grains in thermal equilibrium in the case of homogeneous dust properties along the line of sight, assuming the spectral emissivity index is correct) is created in the same way as in W96. The dust temperature, T_d , is derived from inverting

$$\mathcal{R} = \frac{\nu_9^\beta B_{\nu_9}(T_d) K_{\nu_9}(T_d, \beta)}{\nu_{10}^\beta B_{\nu_{10}}(T_d) K_{\nu_{10}}(T_d, \beta)} \quad , \quad (4)$$

where $\mathcal{R} \equiv I_{\nu_9}/I_{\nu_{10}}$, I_{ν_9} and $I_{\nu_{10}}$ are the quoted *DIRBE* intensities at frequencies ν_9 and ν_{10} , ν_9 is the frequency at $\lambda_9 = 140 \mu\text{m}$, ν_{10} is the frequency at $\lambda_{10} = 240 \mu\text{m}$, $B_\nu(T_d)$ is the Planck function, and K_ν is the *DIRBE* band color correction. Even though these color corrections never vary by more than 8% from 1.0, their ratio, $K_{\nu_9}/K_{\nu_{10}}$, can vary by up to 14% from 1.0 in the temperature range, $T_d = 15\text{--}30 \text{ K}$. Consequently, the color corrections were necessary for obtaining accurate dust color temperatures. Although there is evidence that β can vary spatially by 10–20% on sub-parsec scales (e.g., see Johnstone & Bally 1999), adopting $\beta = 2.0$ is still valid on the scale of a few parsecs for the reasons given in W96. Equation (4) was solved for T_d by plotting T_d as a function of \mathcal{R} over the temperature range 2.1 K to 210 K, and fitting polynomials over three subranges within the full range. The polynomial fits have a typical accuracy 0.08 K and never deviate by more than 0.4 K, which occurs at $T_d = 2.1 \text{ K}$ and 45 K. The polynomial fits quickly determine T_d for each pixel. The T_d map is shown in Figure 3.

The 1998 release of the *DIRBE* data includes the sigma maps and this allows the computation of the map of random errors in T_d , i.e., a $\sigma(T_d)$ map. To compute this map rapidly and easily, the Wien approximation is applied to the Planck functions in equation (4). The Wien version of (4) is differentiated and rearranged to give the following simple expression:

$$\frac{\sigma(T_d)}{T_d} = \frac{T_d}{A} \frac{\sigma(\mathcal{R})}{\mathcal{R}} \quad , \quad (5)$$

where it was assumed that the color corrections are only weak functions of T_d and where $A = h(\nu_9 - \nu_{10})/k = 42.8$ K. The constants h and k are Planck’s constant and the Maxwell-Boltzmann constant, respectively. The relative error in \mathcal{R} , $\sigma(\mathcal{R})/\mathcal{R}$, was computed from the quadrature sum of the relative errors of the intensities in the $140\ \mu\text{m}$ and $240\ \mu\text{m}$ maps. It must be emphasized that even though the *uncertainties* in T_d are computed from an expression that is based on the Wien approximation — i.e., (5) — *no* such approximation was used in determining the T_d itself. Therefore, the T_d that appears in (5) was computed from (4) (or an accurate approximation of it), which includes the full Planck function and the color corrections. Using the accurately determined T_d improves the accuracy of the derived $\sigma(T_d)$ values. A detailed comparison with $\sigma(T_d)$ determined from a numerical differentiation of (4) shows that the $\sigma(T_d)$ derived from (5) only needs to be corrected upwards by 20–25% in the temperature range 15–30 K. Such a correction was not applied and makes little difference to the results. (This is discussed later in more detail.)

Besides the random uncertainties due to noise, there is the overall calibration or photometric uncertainty of the map in each wavelength band. These are 10.6% and 11.6% in the $140\ \mu\text{m}$ and $240\ \mu\text{m}$ bands, respectively (Hauser et al. 1998). How these systematic uncertainties affect the derived color temperatures, T_d , depends on the relative calibration uncertainty of the $140\ \mu\text{m}$ band with respect to the $240\ \mu\text{m}$ band. In W96 the calibration uncertainty in the $I_\nu(140\ \mu\text{m})/I_\nu(240\ \mu\text{m})$ ratio was specified as 6%. Adopting that value for the current paper gives an uncertainty of ± 0.4 K for $T_d = 15$ K and ± 1.6 K for $T_d = 30$ K. These uncertainties are small compared to the relevant range of values of T_d (i.e., 15–30 K) itself. Consequently, the systematic uncertainty in the $140\ \mu\text{m}/240\ \mu\text{m}$ color temperature is roughly equivalent to an upward or downward shift of about 1 K to the entire T_d map.

2.2. ^{13}CO Data

The ^{13}CO data were obtained with the Nagoya 4-m antenna and cover both the Orion A and Orion B clouds. The beamsize is $2''.7$ and Orion A was mapped with a $2'$ grid spacing. Full details of the Orion A observations are given in Nagahama et al. (1998). The Orion B cloud was mapped with an $8'$ grid spacing. The data consist of velocity-integrated intensities of the ^{13}CO $J = 1 \rightarrow 0$ line and were gridded to the *DIRBE* resolution in the Mollweide projection to allow comparison with the *DIRBE* data. The regridding procedure was a straightforward conversion from the galactic longitude and latitude of the central position of each pointing of the beam on the sky to *DIRBE* pixel coordinates in the Mollweide projection. These pixel coordinates were rounded off to the nearest whole number to give the *DIRBE* pixel that contains the center of the beam. This simple approach does not take into account the cases

where a given pointing of the $2'.7$ beam spills over the edges of given *DIRBE* pixel. However, this is not an important consideration given that the *DIRBE*-gridded map is then smoothed by $3 \text{ pixels} \times 3 \text{ pixels}$. Each *DIRBE* pixel was “hit” by a few pointings of the Nagoya beam and the corresponding intensities were averaged for each *DIRBE* pixel. The $1\text{-}\sigma$ noise level of the Nagoya integrated intensity map was $0.7 \text{ K} \cdot \text{km} \cdot \text{s}^{-1}$. After regridding to the *DIRBE* resolution, the noise-level was computed for each *DIRBE* pixel by dividing the Nagoya map noise-level by the square-root of the number of hits of the Nagoya beam in that pixel. Hence, the regridding process produced both an integrated intensity map of the $^{13}\text{CO } J = 1 \rightarrow 0$ line and a corresponding sigma map. As was done with the *DIRBE* maps, the ^{13}CO map was smoothed by $3 \text{ pixels} \times 3 \text{ pixels}$. The sigma map was smoothed using equation (2), since the pixels are independent in this case.

As mentioned above, the Orion B section of the original Nagoya map has an $8'$ grid spacing even though the beam is only $2'.7$ in size. This spacing gives gaps in the coverage. These gaps do not result in large systematic errors in the velocity-integrated intensities in the final map, largely because all the data were gridded to the *DIRBE* resolution. Systematic errors in the map intensities due to incomplete coverage can be estimated by comparing the Orion A observations on the grid with $2'$ spacing with those same observations on a grid with $8'$ spacing. Both the $2'$ grid and $8'$ grid Orion A data were regridded to the *DIRBE* resolution and then smoothed by $3 \text{ pixels} \times 3 \text{ pixels}$. The median of the intensities of the map that was originally on an $8'$ grid were 10–11% lower than that of the map that was originally on a $2'$ grid. Therefore, it is possible that the Orion B observations need to be corrected upwards by, on average, about 10%. Such a correction was not applied, because this is only a small change that will not affect the results significantly and because application of a single scale factor to *all* the Orion B intensities is overly simplistic.

A final consideration for comparison of the ^{13}CO data with the *DIRBE* data is whether background subtraction, as was done for the *DIRBE* data, is necessary. As was found in W96 for the ^{12}CO data, such background subtraction for molecular line data produced virtually no change in their intensities in the Orion fields. Consequently, no background subtraction was applied to the ^{13}CO map. The map of velocity-integrated radiation temperature of the $^{13}\text{CO } J = 1 \rightarrow 0$ line, or $I(^{13}\text{CO})$, is shown in Figure 4.

2.3. Other Datasets

Other datasets used in this research include the map of the integrated intensities of the $^{12}\text{CO } J = 1 \rightarrow 0$ line, the map of the integrated intensities of the H I 21-cm line, and the map of the peak $^{12}\text{CO } J = 1 \rightarrow 0$ radiation temperatures. The maps of the integrated intensities

of the $^{12}\text{CO } J = 1 \rightarrow 0$ line and of the HI 21-cm line were described in W96 (see also Dame et al. 1987; Maddalena et al. 1986; Heiles & Habing 1974). As in W96, an integrated CO line intensity to molecular gas column density, or X-factor, of $N(\text{H}_2)/\int T_{\text{R}} dv = 2.6 \times 10^{20} \text{ cm}^{-2} \cdot (\text{K} \cdot \text{km} \cdot \text{s}^{-1})^{-1}$ is assumed. Recent work by Dame et al. (2001) suggests that an X-factor of $\sim 2.2 \times 10^{20} \text{ cm}^{-2} \cdot (\text{K} \cdot \text{km} \cdot \text{s}^{-1})^{-1}$ is more appropriate for the Orion clouds. As will be discussed in Section 3.6, this is indeed a more appropriate value (at least for the one-component models fitted to the data), but the value of $2.6 \times 10^{20} \text{ cm}^{-2} \cdot (\text{K} \cdot \text{km} \cdot \text{s}^{-1})^{-1}$ is adopted for consistency with W96. After regridding the data to the *DIRBE* resolution and performing the usual 3 pixel \times 3 pixel smoothing, the noise levels in the CO and HI integrated intensity maps were estimated from the negative tails of the histograms. The 1- σ noise levels are 0.7 and 0.2 in units of 10^{20} cm^{-2} for the CO and HI, respectively. As described in W96, a smooth background representing large-scale background and foreground Galactic emission was subtracted from the HI map. No such background was subtracted from the CO map because it made little difference to the resulting intensities. Both the regridded CO and HI maps can be seen in Figure 3a of W96.

The peak $^{12}\text{CO } J = 1 \rightarrow 0$ radiation temperatures were provided by R. Maddalena and T. Dame (priv. comm.). As with the other datasets, these radiation temperatures were gridded to the Mollweide projection with the same pixels as in the *DIRBE* maps and then smoothed by 3 pixels \times 3 pixels. The negative tail of the histogram of the map of peak $^{12}\text{CO } J = 1 \rightarrow 0$ radiation temperatures suggests a noise level of 0.15 K. This is consistent with the noise level in the map of integrated CO brightnesses for line widths of about $2 \text{ km} \cdot \text{s}^{-1}$. As with the integrated CO map, background subtraction was not necessary. This map looks very similar to the integrated CO map and, consequently, is not shown.

3. Models and Results

The ratio $I_{\nu}(240 \mu\text{m})/I(^{13}\text{CO})$, abbreviated as r_{240} , is shown as a contour map in Figure 5 and is plotted against the $140 \mu\text{m}/240 \mu\text{m}$ color temperature, or T_{d} , in Figure 6. The points in Figure 6 represent the high signal-to-noise positions: those positions with signal at or above 5- σ in $I_{\nu}(140 \mu\text{m})$, $I_{\nu}(240 \mu\text{m})$, and $I(^{13}\text{CO})$. The total number of points in the plot is 674, but these are not totally independent. Given that the effective beamsize is about 3 pixels \times 3 pixels, the effective number of points is about 70. (This is actually a conservative estimate to the effective number of points, because, even though the pixels within the effective beam are not completely *independent*, neither are they completely *dependent*.) This number is important for assigning a confidence level to the model fits.

The physical models used to interpret Figure 6 include single-component LTE models,

single-component non-LTE models, and two-component non-LTE models. Except where mentioned otherwise, the models are based on the following assumption:

The only physical parameters that change from one line of sight to the next are the dust temperature, T_d , and the gas kinetic temperature, T_K , while maintaining a constant difference, $\Delta T \equiv T_d - T_K$. Other physical parameters such as gas density, dust-to-gas mass ratio, dust mass absorption coefficient, etcetera are assumed to be constant from position to position.

This will be referred to as the *basic assumption*. Obviously, this assumption is not strictly correct, but is nevertheless roughly correct in describing the overall trends in the data. Thus the χ^2 statistic that quantifies the goodness of the fit is not only measuring the scatter due to observational uncertainties, but also the scatter due to the real physical variations not accounted for in the basic assumption. The best fit of a certain class of models is found by adjusting a set of model parameters, a_j , so as to minimize the χ^2 . Because there are errors in both variables — i.e. x and y or, more specifically, T_d and r_{240} — the expression for χ^2 must reflect this:

$$\chi^2 = \sum_i d_i^2 \quad , \quad (6)$$

where

$$d_i^2 = \left[\frac{x_{oi} - x_{mi}(\{a_j\})}{\sigma(x_{oi})} \right]^2 + \left[\frac{y_{oi} - y_{mi}(\{a_j\})}{\sigma(y_{oi})} \right]^2 \quad , \quad (7)$$

and where (x_{oi}, y_{oi}) represents observed data point i , $(x_{mi}(\{a_j\}), y_{mi}(\{a_j\}))$ is the point on the model curve closest to data point i , the $\{a_j\}$ are the parameters that characterize the model curve, and $\sigma(x_{oi})$ and $\sigma(y_{oi})$ are the random errors for data point i in x and y , respectively. The closest point on the model curve to data point i is defined as that point on the curve that gives the minimum d_i^2 . Expressions (6) and (7) represent orthogonal regression, in which the fit seeks to minimize the perpendicular distance between each point and the model curve.

In the following sections, we examine the following cases: LTE, non-LTE one component, and non-LTE two components.

3.1. LTE Models and Results

In this section the $^{13}\text{CO } J = 1 \rightarrow 0$ line is assumed to be in LTE and optically thin. In practice, LTE means that the gas density is high enough that the line strength is not *explicitly* dependent on that density. The critical density of this line, at which the downward collisional transition rate is equal to the spontaneous radiative transition rate, is $3 \times 10^3 \text{ cm}^{-3}$. Hence,

this line is “close” to LTE for densities exceeding that critical density, or 10^4 – 10^5 cm^{-3} or higher. Assuming LTE has the advantage that it is only necessary to fit one parameter, $\Delta T \equiv T_d - T_k$. The model curve to be fit is

$$r_{240} = 69.2 \frac{Q(T_d - \Delta T)}{C_{BG}} \frac{\exp\left(\frac{5.28}{T_d - \Delta T}\right)}{\exp\left(\frac{59.9}{T_d}\right) - 1}, \quad (8)$$

where Q is the rotational partition function for ^{13}CO and C_{BG} is the correction for the cosmic background radiation. The reader is referred to Appendices A and B for details. Figure 7 shows the model curves of equation (8) for $\Delta T = -16$ to $+16 \text{ K}$.

The optimum value found for ΔT for the LTE models, i.e. $\Delta T = -4 \pm 1 \text{ K}$, is far from satisfactory: as is seen in Figure 8, even though this curve goes through the center of the triangular cluster of points, it is systematically too high for the points with $T_d > 20 \text{ K}$. Indeed, the chi-square per degree of freedom is $\chi_\nu^2 = 16.5$. Fitting only to the points with $T_d > 20 \text{ K}$ gives the result $\Delta T = +9 \pm 1 \text{ K}$ with $\chi_\nu^2 = 9.0$, but this curve is too low for the center of the triangular cluster of points. In addition, neither the $\Delta T = -4 \text{ K}$ curve nor the $\Delta T = +9 \text{ K}$ curve match the high- r_{240} or low- r_{240} points in the triangular cluster.

The uncertainties specified for the above ΔT value are the formal uncertainties due to the random errors. Normally, this uncertainty is determined by finding the values of ΔT for which the χ^2 value is increased by 1. However, this is appropriate only if the chi-square per degree of freedom, χ_ν^2 , is near 1 (see Press et al. 1992). This is not the case here: the χ_ν^2 is significantly greater than 1. Consequently, the uncertainty in ΔT was determined by finding the values of ΔT for which the χ^2 was increased by the value χ_ν^2 . This is a more conservative estimate of the error in the fitted quantity.

Larger than the random uncertainties are the systematic uncertainties; these uncertainties include the calibration errors in the data and the uncertainties in the assumptions used in comparing data with theory. These uncertainties are listed below:

1. The calibration of the observed r_{240} or $I_\nu(240 \mu\text{m})/I(^{13}\text{CO})$ ratio. The calibration uncertainty of $I_\nu(240 \mu\text{m})$ is 12% (Hauser et al. 1998) and that of $I(^{13}\text{CO})$ is less than 20% (Nagahama et al. 1998). Combining the two uncertainties quadratically would imply a calibration uncertainty of 24% for r_{240} . For simplicity, we adopt a calibration uncertainty of 20%.
2. The uncertainty in the dipole moment, μ , of CO. This uncertainty is 10% (CRC Handbook of Chemistry and Physics 1998-99), but the relationship between CO column density and CO brightness (see equation A25) depends on μ^2 ; this contributes a 20% uncertainty to the model curve.

3. The uncertainty in the abundance of ^{13}CO , $X(^{13}\text{CO})$. This affects the relationship between the CO column density and the H_2 column density. Again, 20% is adopted as the contribution to the uncertainty in the model curve.
4. The uncertainty in the dust optical depth to total gas column density, $\tau_\nu/N(\text{H})$. This affects the relationship of $I_\nu(240\ \mu\text{m})$ to $N(\text{H})$ (see equation B6). It is assumed that this contributes an uncertainty of 20% to the model curve.

For simplicity, all of the above have adopted uncertainties of 20%, which is a number that is roughly appropriate for the above cases. Also, these uncertainties are independent of one another, so that they should be added quadratically. This gives an overall uncertainty of 40% between the model curves and the data.

Note that the systematic and random uncertainties are treated separately. The systematic uncertainties represent a simple scaling up or down of the axes in plots of one quantity against another, while the overall distribution of points in a plot does not change. Hence, parameters determined from fits to the data, like line slopes, are simply scaled up or down accordingly. The random uncertainties, however, represent random reshaping of the distribution of points in a plot and must be included in the model fitting procedure.

To test the effect of the systematic uncertainties on the result, the model fitting is repeated after applying scale factors to the model curves. The scale factors used in the new model fits deviate by as much as 40% from unity and are in steps of 20%: 0.6, 0.8, 1.0, 1.2, and 1.4. As Figure 9 clearly shows, the total variation in the resultant ΔT values due to the systematic uncertainties is much larger than the error bars of the random or formal uncertainties. For the fits to all the high signal-to-noise positions, the ΔT varies from $-24\ \text{K}$ to $+6\ \text{K}$. For the fits to the high signal-to-noise positions with $T_d > 20\ \text{K}$, the ΔT varies from $-4\ \text{K}$ to $+9\ \text{K}$. Such a strong variation of ΔT , a range of 30 K for the fits to all the high signal-to-noise data, means that ΔT cannot be determined in this simple LTE case. This is not surprising given that the fits are not very good. Also, since only one parameter varies anyway, scaling the model curves varies that one parameter — ΔT in this case.

Another test of the model fit is to compare the gas column density as derived from the continuum observations, $N_d(\text{H})$, to that derived from the $^{13}\text{CO}\ J = 1 \rightarrow 0$ line, $N_{13}(\text{HI} + 2\text{H}_2)$. The $N_d(\text{H})$ values are determined from a trivial rearrangement of equation (B6) in Appendix B and the $N_{13}(\text{HI} + 2\text{H}_2)$ values come from

$$N_{13}(\text{HI} + 2\text{H}_2) = N(\text{HI}) + 2N_{13}(\text{H}_2) \quad , \quad (9)$$

in analogy to equation (B3). The $N_{13}(\text{H}_2)$ comes from equation (A27). The value of T_K used in (A27) for each position is given by the value of T_d for that position minus the ΔT of the

model fit. As stated above, $\Delta T = -4$ K, but $\Delta T = +9$ K was used for those positions with $T_d > 20$ K. A plot of $N_{13}(\text{HI} + 2\text{H}_2)$ versus $N_d(\text{H})$ is shown in Figure 10. The error bars represent the random uncertainties; the details of which are discussed in Appendices C and D. The systematic uncertainty in $N_d(\text{H})$ is 30%. This includes the calibration uncertainty of 12% for $I_\nu(240\ \mu\text{m})$, the calibration uncertainty of 6% for $I_\nu(140\ \mu\text{m})/I_\nu(240\ \mu\text{m})$, and the uncertainty due to the background subtraction of 10%. The systematic uncertainty in $N_{13}(\text{HI} + 2\text{H}_2)$ is 20% due to the calibration uncertainty in $I(^{13}\text{CO})$. The quadrature sum of these two uncertainties means that the systematic uncertainty in the slope in the $N_{13}(\text{HI} + 2\text{H}_2)$ versus $N_d(\text{H})$ plot is about 40%. The slope of the plotted straight line and the y-intercept, as stated above, were determined from a routine that considers the uncertainties in both x and y , similar to the orthogonal regression method discussed previously. The uncertainties in the slope and y-intercept were determined by finding the changes in each that would raise the total χ^2 by one, provided that $\chi_\nu^2 \simeq 1$. Since χ_ν^2 was greater than 1, the uncertainties in the slope and y-intercept were determined after scaling up the errors in x and y by the same amount until $\chi_\nu^2 \simeq 1$. The slope of the plot, 1.06 ± 0.03 , suggests that the column densities derived from the ^{13}CO line agree favorably with those determined from the continuum. However, the scatter is large: $\chi_\nu^2 = 16.6$. This is clearly a reflection of the bad fit of the single-component, LTE model to the data.

As a comparison, Figure 10 also includes a plot of the gas column density as derived from applying the usual conversion factor to the integrated intensity of ^{12}CO $J = 1 \rightarrow 0$, $I(^{12}\text{CO})$. As stated previously, the conversion factor employed was $N(\text{H}_2)/\int T_R dv = 2.6 \times 10^{20} \text{ cm}^{-2} \cdot (\text{K} \cdot \text{km} \cdot \text{s}^{-1})^{-1}$. The slope in the fitted line is 1.40 ± 0.04 . This suggests that a more appropriate value for the conversion factor is $1.9 \times 10^{20} \text{ cm}^{-2} \cdot (\text{K} \cdot \text{km} \cdot \text{s}^{-1})^{-1}$; this will be discussed further in Section 3.6. This value for the X-factor is only a crude average for the Orion clouds, because there is large scatter about the straight-line fit: $\chi_\nu^2 = 28.3$. Despite this large scatter, the ^{12}CO -derived column densities are within a factor of 2 of those derived from the continuum observations for about 80% of the points. So even on sub-cloud scales, the X-factor seems to give column densities that are correct to within a factor of 2 for most positions.

Comparison of the scatter in the upper and lower panels of Figure 10 may provide insights into the reliability of ^{12}CO -derived column densities. While the χ_ν^2 for the lower-panel straight-line fit with the ^{12}CO -derived column densities is nearly double that for the upper panel, the samples of points in the two panels are not the same. The sample with the ^{13}CO -derived column densities includes only those positions with greater than $5\text{-}\sigma$ in $I_\nu(140\ \mu\text{m})$, $I_\nu(240\ \mu\text{m})$, and $I(^{13}\text{CO})$. This is 674 points. The sample with the ^{12}CO -derived column densities includes those positions with greater than $5\text{-}\sigma$ in $I_\nu(140\ \mu\text{m})$, $I_\nu(240\ \mu\text{m})$, and $I(^{12}\text{CO})$. This is 1053 points. If the same 674-point sample is also used for the ^{12}CO -

derived column densities, then $\chi_\nu^2 = 17.5$ for the straight-line fit in the bottom panel. This is comparable to the $\chi_\nu^2 = 16.6$ found for the straight-line fit to the upper panel with the ^{13}CO -derived column densities. At face value, the comparable χ_ν^2 values would suggest that the ^{12}CO -derived column densities are almost as reliable as those derived from ^{13}CO . However, considering that the single-component LTE models used here do *not* properly characterize the data, this conclusion would be premature.

Another important point to consider is that of the area filling factors of the gas. The model fitting has the potential of determining the gas kinetic temperature. Since the ^{12}CO $J = 1 \rightarrow 0$ line is optically thick, this line could also give the gas kinetic temperature, if we assume LTE. The peak radiation temperature of this line, $T_{\text{R}}(^{12}\text{CO})$, would give T_{K} . However, $T_{\text{R}}(^{12}\text{CO})$ -derived T_{K} values differ from the model T_{K} values. This discrepancy is easily resolved by considering that the gas does not fill the beam within each narrow velocity interval. The radiation temperature would then be given by

$$T_{\text{R}}(\nu) = \eta_{\text{f}}(\nu) \mathcal{J}_{\nu}(T_{\text{K}}) [1 - \exp(-\tau_{\nu})] \quad , \quad (10)$$

where

$$\mathcal{J}_{\nu}(T_{\text{K}}) \equiv \frac{h\nu}{k} \left\{ \left[\exp\left(\frac{h\nu}{kT_{\text{K}}}\right) - 1 \right]^{-1} - \left[\exp\left(\frac{h\nu}{kT_{\text{BG}}}\right) - 1 \right]^{-1} \right\} \quad . \quad (11)$$

Expression (10) assumes that, at each velocity within the line profile, the telescope beam has an area devoid of gas emission and an area with gas emission. The τ_{ν} is the optical depth of the gas averaged in the appropriate way over the gas-emitting area at frequency ν within the line profile. The $\eta_{\text{f}}(\nu)$ is the area filling factor and is the fraction of the beam area that has gas emission at the frequency ν within the line profile. Given that the ^{12}CO $J = 1 \rightarrow 0$ line is optically thick, equation (10) can be written as

$$\eta_{\text{f}}(\nu) = \frac{T_{\text{R}}(\nu)}{\mathcal{J}_{\nu}(T_{\text{K}})} \quad . \quad (12)$$

Figure 11 shows the $\eta_{\text{f}}(\nu)$ for the peak of the ^{12}CO $J = 1 \rightarrow 0$ line profile determined from (12) plotted against the continuum-derived column densities. The gas kinetic temperatures were computed in the same way as for the column density calculations. There are two important things to notice in this plot. One is that, on average, positions with higher column densities have higher filling factors. This is expected: as the gas column density increases, there is an increasing number of cloud substructures or clumps along the line of sight. On average, more and more of the beam area is filled with clumps. Another thing to notice is that all the area filling factors are less than unity, as expected for a geometric filling factor.

In short, the single-component, LTE models are not very successful in explaining the r_{240} versus T_d plot. At best, these models only crudely reproduce the overall trend in the data and allow only a rough agreement between ^{13}CO -derived column densities and dust-derived column densities.

3.2. Non-LTE Models and Results

In this section, non-LTE effects on the $^{13}\text{CO } J = 1 \rightarrow 0$ line emission are considered. Also, the effects of non-negligible optical depths are also considered. To model the non-LTE line emission, the Large Velocity Gradient (LVG) method was used (Goldreich & Kwan 1974). The advantage of this method is its simplicity. Photodissociation region (PDR) models (e.g., see Mochizuki & Nakagawa 2000; Störzer et al. 2000; Tielens & Hollenbach 1985) are considerably more complicated and not necessary for the crude modeling done here. The LVG method assumes that every point in the gas is identical to every other point, with the exception of the velocities. In the spherical geometry case, every point in the gas is surrounded by points moving away from it in a spherically symmetric pattern with more distant points moving away even more rapidly — similar to a cosmological Hubble flow. Hence, every point in the gas is radiatively coupled to, and at the center of, a spherical region. Outside this region, the line emission of the gas is redshifted beyond that of the gas at the center of the sphere and, consequently, radiatively decoupled from it. This spherical geometry can then estimate the line emission from a spherical clump. This is only an estimate because the LVG method cannot accurately estimate the emission from the edges of a clump. Also, the velocity pattern within the clump would not be spherically symmetric. Nevertheless, the geometry of the region that is radiatively coupled to each point within the clump may be roughly spherical. Each clump is assumed to be radiatively decoupled from the other clumps; the other clumps that have radial velocities within the clump velocity width of a given clump are assumed to fill a small solid angle with respect to 4π steradians.

Once some basic parameters are chosen — the molecule, cosmic background temperature, geometry, and the maximum number of levels to be included in the computation — three parameters are specified: the kinetic temperature, gas density, and a third parameter. This third parameter can be the abundance per unit velocity gradient, $X(^{13}\text{CO})/(dv/dr)$ for ^{13}CO , or the column density per velocity interval, $N(^{13}\text{CO})/\Delta v$. It is common to choose $X(^{13}\text{CO})/(dv/dr)$ as the third parameter, but this has a couple of problems. One problem is that, by itself, $X(^{13}\text{CO})/(dv/dr)$ has little physical meaning. It says, in effect, that a region of the gas with a certain velocity width has a certain size (assuming fixed abundance); this says very little about the excitation by itself; the density must also be known. On the other hand,

$N(^{13}\text{CO})/\Delta v$ states that a region of gas with a particular velocity width has a certain column density; this provides strong clues to the level of radiative trapping. For example, in the range of parameter space described in the next paragraph, given the optical depth of the $J = 1 \rightarrow 0$ line of CO for given T_K and $N(^{13}\text{CO})/\Delta v$ values, one can estimate the optical depth to within a factor of ten for other values of T_K and $N(^{13}\text{CO})/\Delta v$ about 80% of the time *even without knowing the gas density* (provided that that unknown density is held constant). Another problem with using $X(^{13}\text{CO})/(dv/dr)$ is that the effects of collisions and radiative trapping are mixed together, making interpretation of observational data more difficult. Specifically, the gas density, $n(\text{H}_2)$, affects not only the collisions but also the column density. Because $N(^{13}\text{CO})/\Delta v = n(\text{H}_2) X(^{13}\text{CO})/(dv/dr)$, raising $n(\text{H}_2)$ for fixed $X(^{13}\text{CO})/(dv/dr)$ also raises $N(^{13}\text{CO})/\Delta v$, thereby raising the line optical depth while also raising the collision rate. This results in misleading impressions of the density sensitivity of line emission. For example, it has been mistakenly found that the $^{13}\text{CO } J = 1 \rightarrow 0 / ^{12}\text{CO } J = 1 \rightarrow 0$ intensity ratio is sensitive to $n(\text{H}_2)$ (e.g., Sakamoto et al. 1997; Tosaki et al. 2002). This intensity ratio when plotted as a function of $n(\text{H}_2)$ for fixed $X(^{13}\text{CO})/(dv/dr)$ does show a strong variation with $n(\text{H}_2)$, but this is because the rising $n(\text{H}_2)$ also results in rising $\tau(^{13}\text{CO } J = 1 \rightarrow 0)$ and, of course, the $^{13}\text{CO } J = 1 \rightarrow 0 / ^{12}\text{CO } J = 1 \rightarrow 0$ intensity ratio *is* sensitive to $\tau(^{13}\text{CO } J = 1 \rightarrow 0)$. (In fact, $\tau(^{13}\text{CO } J = 1 \rightarrow 0)$ is equivalent to this intensity ratio in the LTE, optically thin limit.) Being unaware of this coupling between optical depth and density has led to errors in interpretation of the data. In one case, the authors went so far as to conclude that the molecular gas in the galaxy M 51 must have temperatures of several hundred kelvins on scales of hundreds of parsecs, based on a comparison of the $J = 1 \rightarrow 0$ lines of HCN, ^{13}CO , and ^{12}CO (Tosaki et al. 2002); this despite the much simpler and much more likely interpretation of low-temperature gas with optically thin $^{13}\text{CO } J = 1 \rightarrow 0$ emission. Therefore we choose $N(^{13}\text{CO})/\Delta v$ to be the third parameter used in the LVG models.

The specific range of parameter space used in the modeling is as follows:

- $T_K = 2.8$ to 40.7 K in steps of 0.1 K.
- $\log_{10}[n(\text{H}_2)(\text{cm}^{-3})] = 1$ to 5 in steps of 0.25 .
- $\log_{10} \left[\frac{N(^{13}\text{CO})}{\Delta v} (\text{cm}^{-2} \cdot (\text{km} \cdot \text{s}^{-1})^{-1}) \right] = 15.5$ to 18.3 in steps of 0.2 .

The reason for the chosen lower limit on $N(^{13}\text{CO})/\Delta v$ has to do with the observed column densities of the Orion clouds. The majority of positions, 93%, have $N(\text{H I} + 2\text{H}_2) < 1 \times 10^{22} \text{ cm}^{-2}$. Negligible $N(\text{H I})$ and cloud line widths of $2 \text{ km} \cdot \text{s}^{-1}$ mean that this limit corresponds to $N(\text{H}_2)/\Delta v = 2.5 \times 10^{21} \text{ cm}^{-2} \cdot (\text{km} \cdot \text{s}^{-1})^{-1}$. Using the abundances given in Appendix A, this is equivalent to $N(^{13}\text{CO})/\Delta v = 3.2 \times 10^{15} \text{ cm}^{-2} \cdot (\text{km} \cdot \text{s}^{-1})^{-1}$. This column

density per velocity interval represents a large-scale cloud property, for some positions in the Orion clouds, and must *not* be confused with the column density per velocity interval within the individual substructures or clumps. The $N(^{13}\text{CO})/\Delta v$ values within the clumps can be higher than the large-scale values for a cloud. However, the values for $N(^{13}\text{CO})/\Delta v$ cannot be much smaller than the large-scale value without also having many clumps within a given velocity interval that are radiatively coupled. Radiatively coupled clumps means that the effective $N(^{13}\text{CO})/\Delta v$ is roughly the sum of the $N(^{13}\text{CO})/\Delta v$ values for the individual clumps. Consequently, values much less than the large-scale cloud $N(^{13}\text{CO})/\Delta v$ value are not meaningful. Therefore, a lower limit of $N(^{13}\text{CO})/\Delta v = 3.2 \times 10^{15} \text{ cm}^{-2} \cdot (\text{km} \cdot \text{s}^{-1})^{-1}$ is adopted, which is not too low for 93% of the high signal-to-noise positions (i.e. those positions represented in Fig 6) in the Orion clouds.

To develop the expression for r_{240} that uses LVG model results, we start with

$$I_\nu = 2 B_\nu(T_d) \kappa_\nu x_d \mu_H m_H N(\text{H}_2) \quad , \quad (13)$$

where I_ν is the continuum intensity. The above expression is a combination of equations (B1), (B2), and (B3) with $N(\text{HI}) = 0$. The integrated strength of the ^{13}CO $J = 1 \rightarrow 0$ line can be written as

$$I(^{13}\text{CO}) = T_R(^{13}\text{CO}) \Delta v \quad , \quad (14)$$

which is exact if Δv is defined appropriately. The quotient of (13) and (14) can be expressed as

$$\frac{I_\nu}{I(^{13}\text{CO})} = \frac{2 B_\nu(T_d) \kappa_\nu x_d \mu_H m_H}{X(^{13}\text{CO})} \left[\frac{N(^{13}\text{CO})}{\Delta v} \right]_{mod} [T_R(^{13}\text{CO})]_{mod}^{-1} \quad . \quad (15)$$

The subscript *mod* means that the quantity is either an LVG model input, $[N(^{13}\text{CO})/\Delta v]_{mod}$ or output, $[T_R(^{13}\text{CO})]_{mod}$. Using the values of the physical parameters from Appendices A and B, equation (15) becomes

$$\frac{I_\nu (\text{MJy} \cdot \text{sr}^{-1})}{I(^{13}\text{CO})} = 0.440 \lambda^{-5} (\mu\text{m}) \left[\exp\left(\frac{1.44 \times 10^4}{\lambda(\mu\text{m}) T_d}\right) - 1 \right]^{-1} \left[\frac{N(^{13}\text{CO})}{\Delta v} \right]_{mod} [T_R(^{13}\text{CO})]_{mod}^{-1} \quad . \quad (16)$$

Setting λ to $240 \mu\text{m}$ gives

$$r_{240} = 5.53 \times 10^{-13} \left[\exp\left(\frac{59.9}{T_d}\right) - 1 \right]^{-1} \left[\frac{N(^{13}\text{CO})}{\Delta v} \right]_{mod} [T_R(^{13}\text{CO})]_{mod}^{-1} \quad . \quad (17)$$

Even though ΔT and $n(\text{H}_2)$ do not *explicitly* appear in (17), the $[T_R(^{13}\text{CO})]_{mod}$ is an LVG model result, so it depends on $T_K (= T_d - \Delta T)$, $N(^{13}\text{CO})/\Delta v$, and $n(\text{H}_2)$. The effects of varying the parameters ΔT , $N(^{13}\text{CO})/\Delta v$, and $n(\text{H}_2)$ on the model curves are shown in Figures 12, 13, and 14.

The best fitting curve is shown in Figure 15. The solid curve is fit to all data at more than $5\text{-}\sigma$ in $I_\nu(140\text{ }\mu\text{m})$, $I_\nu(240\text{ }\mu\text{m})$, and $I(^{13}\text{CO})$. The best fit parameters are $\Delta T = -1 \pm 1\text{ K}$, $N(^{13}\text{CO})/\Delta v = (3.2 \pm \frac{1.8}{?}) \times 10^{15}\text{ cm}^{-2} \cdot (\text{km} \cdot \text{s}^{-1})^{-1}$, and $n(\text{H}_2) = (1.0 \pm \frac{?}{0.4}) \times 10^5\text{ cm}^{-3}$. Note that it is not possible to put a firm lower limit on $N(^{13}\text{CO})/\Delta v$ nor a firm upper limit on $n(\text{H}_2)$. In the former case, $N(^{13}\text{CO})/\Delta v$ is low enough that $^{13}\text{CO } J = 1 \rightarrow 0$ is close to the optically thin limit, and r_{240} is insensitive to $N(^{13}\text{CO})/\Delta v$ in this limit. In the latter case, $n(\text{H}_2)$ is high enough that $^{13}\text{CO } J = 1 \rightarrow 0$ is close to LTE and r_{240} is insensitive to $n(\text{H}_2)$ in that limit. The chi-square per degree of freedom, χ_ν^2 is 16.9, similar to that for the LTE model fit. The dashed curve is fit to the same $5\text{-}\sigma$ data, but only for $T_d \geq 20\text{ K}$. The parameters for this curve are $\Delta T = -3 \pm 4\text{ K}$, $N(^{13}\text{CO})/\Delta v = (3.2 \pm \frac{1.8}{?}) \times 10^{15}\text{ cm}^{-2} \cdot (\text{km} \cdot \text{s}^{-1})^{-1}$, and $n(\text{H}_2) = (5.6 \pm \frac{4.4}{2.5}) \times 10^3\text{ cm}^{-3}$. The goodness of fit is $\chi_\nu^2 = 9.98$. Again, as for the LTE case, the LVG one-component model clearly does not well characterize the data.

The poorness of the fit is also illustrated in Figure 16, which shows plots of the parameter variations with the scale factors. The total range in ΔT is 13 or 14 K. $N(^{13}\text{CO})/\Delta v$ varies by a factor of 7 for the solid curve and does not vary for the dashed curve. $n(\text{H}_2)$ varies by nearly two orders of magnitude. If we ignore the cases with limits instead of error bars, then we see again that the systematic variations are larger than the random errors (except for the dashed curve showing the $N(^{13}\text{CO})/\Delta v$ variation). The particularly large uncertainty in $n(\text{H}_2)$ is understandable because the $^{13}\text{CO } J = 1 \rightarrow 0$ line loses its density sensitivity for $n(\text{H}_2) \gtrsim \text{few} \times 10^3\text{ cm}^{-3}$. In short, as in the LTE case, it is difficult to determine the values of the parameters with certainty.

Again the continuum-derived gas column density, $N_d(\text{H})$, is compared with that derived from the $^{13}\text{CO } J = 1 \rightarrow 0$ line, $N_{13}(\text{HI} + 2\text{H}_2)$. The $N_d(\text{H})$ values are determined as in the LTE case (see Section 3.1). The $N_{13}(\text{HI} + 2\text{H}_2)$ values come from equation (9), where $N_{13}(\text{H}_2)$ is derived from

$$N_{13}(\text{H}_2) = \frac{[N(^{13}\text{CO})/\Delta v]_{mod}}{X(^{13}\text{CO}) [T_R(^{13}\text{CO } J = 1 \rightarrow 0)]_{mod}} I(^{13}\text{CO}) \quad , \quad (18)$$

where the subscript *mod* refers to LVG model quantities (i.e. model input or output parameters), $X(^{13}\text{CO})$ is the value adopted in Appendix A, and $I(^{13}\text{CO})$ is the observed intensity. Each point on the model curve has particular values of $[N(^{13}\text{CO})/\Delta v]_{mod}$ and $[T_R(^{13}\text{CO } J = 1 \rightarrow 0)]_{mod}$ associated with it. Each data point was then associated with a point on the model curve. This was done in the same way that the χ^2 values were computed: for each data point, the minimum of the distances to all the points on the model curve was the minimum of all values given by equation (7). (Also see discussion of this in Appendix E.) Note that the model curve used is the solid curve in Figure 15 for points with $T_d < 20\text{ K}$ and is the dashed curve in Figure 15 for points with $T_d \geq 20\text{ K}$. The random errors associated

with the $N_{13}(\text{H}_2)$ column densities were computed as described in Appendix E. The plot of $N_{13}(\text{HI} + 2\text{H}_2)$ versus $N_d(\text{H})$ is shown in Figure 17. The straight-line fit to the points was done in same way as for Figure 10 in the LTE case. The slope of the line, 1.08 ± 0.02 , suggests that there is good overall agreement between the continuum-derived and spectral line-derived column densities, except that the scatter is large: $\chi_\nu^2 = 15.5$. This is only marginally smaller than the $\chi_\nu^2 = 16.6$ obtained for the LTE case. Hence, the improvement from LTE, one-component models to LVG, one-component models is minor.

The filling factors as a function of spectral line derived column densities in the LVG, one-component case are plotted in Figure 18. The filling factors were derived using equation (12). The T_K used in that equation was determined from the observed T_d at each position minus the appropriate ΔT from the model fits. (Even though these are non-LTE models, the $^{12}\text{CO } J = 1 \rightarrow 0$ line is still essentially thermalized at these densities — i.e., $n(\text{H}_2) = 1 \times 10^5$ and $5.6 \times 10^3 \text{ cm}^{-3}$ — due to its high opacity. Consequently, the excitation temperature *of this transition* is close to T_K and simply using T_K in equation 12 is appropriate.) As in the LTE case, the filling factors, on average, increase with increasing column density. Again there is a saturation effect: the slope of the plot decreases with increasing column density.

In short, the single-component, LVG models do not successfully explain the r_{240} versus T_d plot and are, at best, only marginally better than the single-component, LTE models.

3.3. Two-Component, Non-LTE Models and Results

As discussed in the previous sections, single-component models only poorly characterize the data. In this section we assume that there are two emission components. “Component 0” is present on all lines of sight and has *constant* properties on all those lines of sight. Specifically, the dust temperature, gas kinetic temperature, column density per velocity interval, and gas density are all constant. “Component 1” is similar except that the dust and gas temperatures can vary from line of sight to line of sight while maintaining a constant dust–gas temperature difference, ΔT , as stated in the basic assumption. The physical motivation for these components is straightforward. Component 0 represents molecular gas at the surface of the Orion clouds and is heated only by the general interstellar radiation field (ISRF), giving it a constant temperature. Component 1 is the molecular gas deeper into the Orion clouds and is largely shielded from the general ISRF by component 0. Therefore, those positions in component 1 without stars will have colder dust temperatures than in component 0. In contrast, those positions in component 1 with stars will have warmer dust than in component 0. In this simple picture, component 0 has a constant temperature and component 1 has a varying temperature from position to position, varying above and below

the dust temperature of component 0.

We now need expressions relating the observed emission to the physical parameters of the gas and dust in order to construct the two-component models. The expressions derived here will be necessary for the simulations described in Paper II. Construction of the models requires certain simplifications. For example, it is assumed that component 0 has the same ΔT as component 1. Also, as discussed in Section 3.2, the clumps are assumed to be radiatively de-coupled from one another. Specifically, for these two-component models, it is assumed that the clumps of component 0 are de-coupled from those of component 1. Therefore the emission of the two components can simply be added together. Consequently, the specific intensity of the continuum emission averaged over the beam, I_ν , is given by

$$I_\nu = g_1 N_{c1} f_\nu(T_{d1}) + g_0 N_{c0} f_\nu(T_{d0}) \quad , \quad (19)$$

where $f_\nu(T_d)$ is defined as

$$f_\nu(T_d) \equiv \kappa_{\nu 0} x_d \mu_H m_H \left(\frac{\nu}{\nu_0} \right)^\beta B_\nu(T_d) \quad , \quad (20)$$

combining equations (B1), (B2), (B5) and removing the column density factor. N_{c1} is the column density of hydrogen nuclei (i.e. $2N(H_2)$ for purely molecular hydrogen) of each clump of component 1. g_1 is the number of clumps of component 1 on each line of sight averaged over the beam area. N_{c0} and g_0 are the corresponding quantities for component 0. The total number of clumps per line of sight averaged over the beam from both components, g , is given by

$$g = \frac{N}{a_1 N_{c1} + a_0 N_{c0}} \quad , \quad (21)$$

where N is the observed column density (i.e. the column density averaged over the beam) and a_1 , a_0 are the fractions of clumps belonging to components 1 and 0, respectively. Obviously, then

$$a_0 + a_1 = 1 \quad . \quad (22)$$

It follows then that

$$g_1 = a_1 g = \frac{N}{N_{c1} + c_0 N_{c0}} \quad (23)$$

and

$$g_0 = a_0 g = \frac{c_0 N}{N_{c1} + c_0 N_{c0}} \quad , \quad (24)$$

where

$$c_0 \equiv \frac{a_0}{a_1} \quad . \quad (25)$$

Notice that $g = g_1 + g_0$ follows naturally from (21), (22), (23), and (24). Equation (19) can now be written as

$$I_\nu = \frac{N}{N_{c1} + c_0 N_{c0}} N_{c1} f_\nu(T_{d1}) + \frac{N}{N_{c1} + c_0 N_{c0}} c_0 N_{c0} f_\nu(T_{d0}) \quad . \quad (26)$$

To compare the continuum emission strength with that of a spectral line, the cloud's velocity structure must be considered. Even though the dust grain velocities have no appreciable effect on the continuum emission, we can imagine examining the emission of only those dust grains associated with the ^{13}CO molecules emitting in a certain part of the ^{13}CO $J = 1 \rightarrow 0$ line. As such, the right side of (26) is multiplied by $\frac{\Delta v_c}{\Delta v} \frac{\Delta v}{\Delta v_c}$, where Δv is the observed line width and Δv_c is the clump line width. For simplicity it is assumed that *all* clumps have the same velocity width. Consequently, (26) can be written as

$$I_\nu = c_1 \left[\frac{N_{c1}}{\Delta v_c} f_\nu(T_{d1}) + c_0 \frac{N_{c0}}{\Delta v_c} f_\nu(T_{d0}) \right] \Delta v \quad , \quad (27)$$

where

$$c_1 \equiv \frac{(N/\Delta v)}{\frac{N_{c1}}{\Delta v_c} + c_0 \frac{N_{c0}}{\Delta v_c}} \quad . \quad (28)$$

Analogous to g_1 , c_1 is the number of clumps of component 1 per line of sight averaged over the beam *within a velocity interval equal to a clump velocity width*. The parameter c_0 (which is *not* analogous to g_0) is the ratio of the number of clumps of component 0 to those of component 1. (Note that clump velocity widths of the two components are assumed to be identical. Generalizing to the case of different clump velocity widths of the two components is trivial.) Analogous to the continuum emission equation (i.e. equation 27), the equation for the integrated radiation temperature of the ^{13}CO $J = 1 \rightarrow 0$ line is

$$I(^{13}\text{CO}) = c_1 \left[T_{R1}(T_{K1}, \frac{N_{c1}}{\Delta v_c}, n_{c1}) + c_0 T_{R0}(T_{K0}, \frac{N_{c0}}{\Delta v_c}, n_{c0}) \right] \Delta v \quad , \quad (29)$$

where T_{R1} and T_{R0} are the component-1 and component-0 radiation temperatures, respectively, T_{K1} and T_{K0} are the gas kinetic temperatures in components 1 and 0, respectively, and n_{c1} and n_{c0} are the molecular gas densities in the component-1 and component-0 clumps, respectively. Note that $\frac{N_{c1}}{\Delta v_c}$ is $\frac{N_{c1}(\text{H}_2)}{\Delta v_c}$ and $\frac{N_{c0}}{\Delta v_c}$ is $\frac{N_{c0}(\text{H}_2)}{\Delta v_c}$. The LVG results, T_{R1} and T_{R0} , depend directly on $\frac{N_{c1}(^{13}\text{CO})}{\Delta v_c}$ and $\frac{N_{c0}(^{13}\text{CO})}{\Delta v_c}$, respectively. Consequently, T_{R1} and T_{R0} as written in equation (29) also implicitly depend on the ^{13}CO to H_2 abundance ratio, $X(^{13}\text{CO})$. Dividing (27) by (29) gives the desired r_{240} :

$$r_{240} = \frac{\frac{N_{c1}}{\Delta v_c} f_\nu(T_{d1}) + c_0 \frac{N_{c0}}{\Delta v_c} f_\nu(T_{d0})}{T_{R1}(T_{d1} - \Delta T, \frac{N_{c1}}{\Delta v_c}, n_{c1}) + c_0 T_{R0}(T_{d0} - \Delta T, \frac{N_{c0}}{\Delta v_c}, n_{c0})} \quad , \quad (30)$$

where the following equations were used:

$$T_{K1} = T_{d1} - \Delta T \quad (31)$$

and

$$T_{K0} = T_{d0} - \Delta T \quad . \quad (32)$$

Again, the same ΔT is assumed for both components.

Equation (30) is used to determine the r_{240} ratio for the two-component, non-LTE case. The T_{R1} and T_{R0} values are determined from the LVG method. These models have seven input parameters: ΔT , c_0 , T_{d0} , $\frac{N_{c0}}{\Delta v_c}$, n_{c0} , $\frac{N_{c1}}{\Delta v_c}$, and n_{c1} . The component-1 dust temperature, T_{d1} , varies, resulting in model curves of r_{240} versus dust temperature. The dust temperature used in the plots of the model curves is the $140 \mu\text{m}/240 \mu\text{m}$ color temperature, T_{dc} . To solve for T_{dc} , the expression (27) is evaluated at ν_9 corresponding to $\lambda_9 = 140 \mu\text{m}$ and at ν_{10} corresponding to $\lambda_{10} = 240 \mu\text{m}$ and these are divided to yield:

$$\mathcal{R} = \frac{\frac{N_{c1}}{\Delta v_c} f_{\nu 9}(T_{d1}) K_{\nu 9}(T_{d1}, \beta) + c_0 \frac{N_{c0}}{\Delta v_c} f_{\nu 9}(T_{d0}) K_{\nu 9}(T_{d0}, \beta)}{\frac{N_{c1}}{\Delta v_c} f_{\nu 10}(T_{d1}) K_{\nu 10}(T_{d1}, \beta) + c_0 \frac{N_{c0}}{\Delta v_c} f_{\nu 10}(T_{d0}) K_{\nu 10}(T_{d0}, \beta)} \quad , \quad (33)$$

which uses the same notation as expression (4) in Section 2.1. The color corrections, $K_{\nu}(T_d, \beta)$, are used in order to correctly assess the relative contributions of the two components to *DIRBE*'s bands 9 and 10. Equation (4), with T_{dc} in place of T_d , is then solved for T_{dc} . This allows a valid comparison of the model T_{dc} values with the *DIRBE* observed T_{dc} values.

The master grid of T_K and $n(\text{H}_2)$ values is the same as that for the one-component, LVG models. The master grid values of $\log_{10} \left[\frac{N(^{13}\text{CO})}{\Delta v} (\text{cm}^{-2} \cdot (\text{km} \cdot \text{s}^{-1})^{-1}) \right]$ is extended down from 15.5 to 14.3. This does not necessarily violate the constraint that the minimum column density per velocity interval be about that of the cloud on the scale of a beam, because we are now dealing with two components. Having the combined column density per velocity interval of the two components above this minimum is still required. The panels of Figure ?? show how the theoretical curves are affected by the values of the model parameters. Many of the curves are characterized by the triangular loop that exists between $T_{dc} \simeq 15$ and $\simeq 19 \text{ K}$ and $r_{240} \simeq 7$ and $\simeq 40 \text{ MJy} \cdot \text{sr}^{-1} \cdot (\text{K} \cdot \text{km} \cdot \text{s}^{-1})^{-1}$. This loop is a consequence of the two components emitting in the Wien limit.

The best-fit curve is shown in Figure 19 and is fitted to all the data at more than 5σ in $I_{\nu}(140 \mu\text{m})$, $I_{\nu}(240 \mu\text{m})$, and $I(^{13}\text{CO})$, and the parameters are listed in Table 1. The curve is characterized by the triangular loop that exists between $T_{dc} \simeq 15$ and $\simeq 19 \text{ K}$ and $r_{240} \simeq 7$ and $\simeq 40 \text{ MJy} \cdot \text{sr}^{-1} \cdot (\text{K} \cdot \text{km} \cdot \text{s}^{-1})^{-1}$. This loop is a consequence of the two

components emitting in the Wien limit. The formal uncertainties are not listed because they are extremely small and not really meaningful when compared with the systematic uncertainties. The formal uncertainties for ΔT and T_{d0} are less than 3×10^{-4} K and for the other parameters the formal *relative* uncertainties are less than 3×10^{-4} . Unlike the one-component model curve, the two-component model curve is a reasonably good fit to the data, with $\chi^2_\nu = 5.7$. The F-test states that the two-component model is better than the one-component models at the 99.9% confidence level. (Note that the number of degrees of freedom adopted for estimating this confidence level was about 1/9 the number in Table 1, because the points in Figure 19, which represent individual map pixels, are *not* independent. Given that the number of pixels per effective beam is about 9, the effective number of degrees of freedom is reduced accordingly. This reduction results in a *lower* confidence level than would have occurred without this reduction.) Figure 19 explains the overall trend in the data and *even explains a large part of the triangular cluster of points* (see Section 3). Nevertheless, this fit still has certain problems: the curve does not follow the curvature in the data for $T_{dc} \gtrsim 20$ K and it does not account for the low- r_{240} points in the triangular cluster where $T_{dc} > 18$ K. While the best-fit curve does not explain these low- r_{240} points, inspection of Figure ?? suggests that some combination of parameter values could account for these points: if the component-0 parameters were allowed to vary from position to position (i.e., ignoring the basic assumption), for example. Also, allowing T_{d0} to vary between about 18 K and 20 K could fit these points. Nevertheless, given the simplicity of these two-component models, the current fit is reasonable. In addition, as mentioned in Section 3.1, these points could also be explained by uncertainties in the observations.

Even though the curve in Figure 19 is an adequate fit, the parameters in Table 1 still have appreciable uncertainty. Figure 20 shows the systematic effects on the resultant parameter values when the scale factor is changed. Parameters like ΔT and T_{d0} are known extremely well, ± 1 K or better, while parameters like $\frac{N_{c0}(^{13}\text{CO})}{\Delta v_c}$ and n_{c0} are uncertain by 2 or 3 orders of magnitude. Still others like c_0 , $\frac{N_{c1}(^{13}\text{CO})}{\Delta v_c}$, and n_{c1} are apparently known to within about an order of magnitude or better. In the case of the one-component models, ascertaining *any* of the parameter values was difficult. In the case of the two-component models, again *some* parameter values are very uncertain, but some are apparently very well known indeed.

The systematic uncertainties in the resultant parameter values were also tested by varying the starting search grid. There are enough parameters in the two-component models that a search grid with *both* sufficient range in all parameters *and* sufficient resolution (i.e. grid spacing) in all parameters was not possible. Therefore, the starting search grid had a large range in all parameters and poor resolution (i.e. large grid spacing). After the initial search, a new grid with better resolution and smaller range moved closer to the final solution. This was repeated a few times to home in on the final solution. In total there were 3 to 5 search

grids (including the starting grid) for each final solution. Of course, one wonders about the final solution’s stability: does the starting search grid affect the final answer? In the ideal case the answer is no. Nevertheless, this was tested by adjusting the starting search grid’s position to see the effect on the final answer. In total, four different starting search grids were tested and the results were examined. The results did indeed change depending on the starting grid. Nevertheless, the ranges in the results’ variations had nearly identical sizes (in a linear sense for ΔT and T_{d0} and in a logarithmic sense for the other parameters) to those found from varying the scale factors.

As in the previous sections, the gas column density as derived from the continuum observations, $N_d(H)$, is compared with that derived from the ^{13}CO $J = 1 \rightarrow 0$ line, $N_{13}(HI + 2H_2)$. The $N_{13}(H_2)$ values are derived from a modified version of equation (18) that was used for the one-component, LVG model:

$$N_{13}(H_2) = \frac{\left[\frac{N_{c1}(^{13}CO)}{\Delta v_c} \right]_{mod} + c_0 \left[\frac{N_{c0}(^{13}CO)}{\Delta v_c} \right]_{mod}}{X(^{13}CO) \left\{ [T_{R1}(^{13}CO \ J = 1 \rightarrow 0)]_{mod} + c_0 [T_{R0}(^{13}CO \ J = 1 \rightarrow 0)]_{mod} \right\}} I(^{13}CO) . \quad (34)$$

Using this equation is similar to using equation (18) for the one-component, LVG models. As for those one-component models, the random errors associated with the $N_{13}(H_2)$ column densities were computed as described in Appendix E. The $N_d(H)$ values must now be computed and require corrections from the one-component cases of the previous sections. This correction is

$$\frac{N_d(H)}{N_{d1}(H)} = \frac{N_{2M}}{N_{1M}} , \quad (35)$$

where $N_d(H)$ is the “true” dust-derived column density inferred from the observations in the two-component case, $N_{d1}(H)$ is the dust-derived column density that *would be* inferred from the observations assuming one component only, N_{2M} is the model column density for a two-component model, and N_{1M} is the model column density that would result if a single component were assumed. Specifically, this single component would have the color temperature, T_{dc} , and the specific intensity of the two-component model, as given by (27). So the right side of (35) is the correction factor that would be applied to the model column density to obtain the “true” model column density. Equation (35) then applies this correction factor to the actual observations. If all the column densities in (35) are beam-averaged column densities, then

$$N_{2M} = g_1(N_{c1} + c_0 N_{c0}) \quad (36)$$

and

$$N_{1M} = g_1 N_c . \quad (37)$$

Equation (36) is combination of equations (21), (23), (24), and (25). The N_c in equation (37) is the effective column density of a single clump for the one-component “version” of the two-component model. It is given by the expression,

$$I_{\nu_{10}} = c_1 \frac{N_c}{\Delta v_c} f_{\nu_{10}}(T_{dc}) \Delta v \quad , \quad (38)$$

which is the one-component analog of expression (27) that uses ν_{10} in place of ν . Equating (38) with (27) and rearranging yields

$$\frac{N_c}{\Delta v_c} = \frac{\frac{N_{c1}}{\Delta v_c} f_{\nu_{10}}(T_{d1}) + c_0 \frac{N_{c0}}{\Delta v_c} f_{\nu_{10}}(T_{d0})}{f_{\nu_{10}}(T_{dc})} \quad . \quad (39)$$

Expression (39) is substituted into (37), and (37) and (36) are substituted into (35). After this, a factor of $X(^{13}\text{CO})$ is removed from both numerator and denominator to yield

$$N_d(\text{H}) = \frac{\left\{ \left[\frac{N_{c1}(^{13}\text{CO})}{\Delta v_c} \right]_{mod} + c_0 \left[\frac{N_{c0}(^{13}\text{CO})}{\Delta v_c} \right]_{mod} \right\} f_{\nu_{10}}(T_{dc})}{\left[\frac{N_{c1}(^{13}\text{CO})}{\Delta v_c} \right]_{mod} f_{\nu_{10}}(T_{d1}) + c_0 \left[\frac{N_{c0}(^{13}\text{CO})}{\Delta v_c} \right]_{mod} f_{\nu_{10}}(T_{d0})} N_{d1}(\text{H}) \quad (40)$$

As done in the previous section for the one-component, LVG models, each data point was associated with the point on the model curve closest to it. The parameter values associated with that point on the model curve were then used in (34) and (40) to give the column densities $N_{13}(\text{H}_2)$, and therefore $N_{13}(\text{HI} + 2\text{H}_2)$, and $N_d(\text{H})$ corresponding to that data point. The uncertainties in $N_d(\text{H})$ are discussed in Appendix F.

Figure 21 is the plot of the ^{13}CO -derived column densities versus the dust-derived gas column densities. Clearly the agreement is much better than for the one-component models: $\chi^2_\nu = 7.4$. The slope of the straight-line fit, 1.08 ± 0.01 , is within the error of the corresponding slope for the one-component, LVG models. *It is clear that the two-component models are significantly better than the one-component models.*

The filling factors as a function of spectral line derived column densities in the LVG, two-component case are plotted in Figure 22. The filling factors were derived using a two-component analog of equation (12). Specifically, an effective excitation temperature, $\mathcal{J}_\nu(\text{eff})$, is determined from

$$\mathcal{J}_\nu(\text{eff}) = \frac{\mathcal{J}_\nu(T_{x1}) + c_0 \mathcal{J}_\nu(T_{x0})}{1 + c_0} \quad , \quad (41)$$

where T_{x1} and T_{x0} are the excitation temperatures of the ^{12}CO $J = 1 \rightarrow 0$ line in components one and zero, respectively. This effective excitation temperature is the brightness

temperature that would be observed at frequency ν if the gas filled the beam at the velocity in the line profile corresponding to frequency ν . (Note that this assumes that the line is optically thick. Note also that $\mathcal{J}_\nu(\text{eff})$ includes the Rayleigh-Jeans correction and the correction for the background.) The excitation temperatures, T_{x1} and T_{x0} , were computed with the following method. Each observed position has an associated point on the model curve. The point on the model curve has associated T_{d1} , T_{d0} , and ΔT values. These allow computation of the T_{K1} and T_{K0} values. The point on the model curve is also associated with the other model parameters, which permit determination of the T_{x1} and T_{x0} values from LVG models of the ^{12}CO line strengths. In particular, the $J = 1 \rightarrow 0$ line of ^{12}CO is optically thick and, as such, radiative trapping keeps the line closer to LTE. Therefore, the conversion from kinetic temperature to excitation temperature is close to unity. Specifically, the following approximations are accurate to within a few percent:

$$T_{x0} \simeq T_{K0} \quad (42a)$$

and

$$T_{x1} \simeq T_{K1} \left[1 - 0.08 \left(\frac{T_{K1}}{30} \right)^2 \right] \quad (42b)$$

Over the observed temperature range, the conversion of T_{K1} to T_{x1} deviates from unity by no more than about an 8%. The filling factor is then given by

$$\eta_f(\nu) = \frac{T_R(\nu)}{\mathcal{J}_\nu(\text{eff})} \quad (43)$$

The value of $\eta_f(\nu)$ at the line peak is plotted in Figure 22. As in the one-component cases, the filling factors, on average, increase with increasing column density. Again there is saturation with increasing column density. However, for these models, the area-filling factors can have non-physical values (i.e. > 1). In fact, some observed positions *seem* to have $\eta_f(\nu)$ up to about 6. Since these are area-filling factors, they cannot be greater than unity. Even if we were to reinterpret $\eta_f(\nu)$ as the number of clumps per line of sight within a clump velocity width, there would still be a problem: the effective column density per velocity interval would be higher than, and therefore inconsistent with, the values of $\frac{N_{c1}(^{13}\text{CO})}{\Delta v_c}$ and $\frac{N_{c0}(^{13}\text{CO})}{\Delta v_c}$ determined from the model fits. Only for $\eta_f(\nu) \leq 1$ is there no such problem, because some lines of sight within the beam, and within a clump velocity interval, can be free of clumps while others can have a single clump (with the properties given by the model fit). When $\eta_f(\nu) > 1$, lines of sight that have clumps will, on average, have more than one clump in a clump velocity interval, thereby forcing the effective $N(^{13}\text{CO})/\Delta v$ to be higher than the fitted $\frac{N_{c1}(^{13}\text{CO})}{\Delta v_c}$ and $\frac{N_{c0}(^{13}\text{CO})}{\Delta v_c}$ values. In addition, given that this is a filling factor within a clump velocity interval and that ^{12}CO $J = 1 \rightarrow 0$ is optically thick, detecting more than one

clump per line of sight within a narrow velocity interval is not possible, because the clump in front would block the emission of the ones behind.

Nevertheless, the problem of the unphysical $\eta_f(\nu)$ values has a solution. Both the numerator and denominator of (30) depend, explicitly or implicitly, on the product $c_0 \frac{N_{c0}}{\Delta v_c}$, and *not* on the individual c_0 and $\frac{N_{c0}}{\Delta v_c}$ values alone, over a large range parameter space. Accordingly, over that range of parameter space, r_{240} depends on that product and determining the parameters c_0 and $\frac{N_{c0}}{\Delta v_c}$ separately is very difficult. Indeed, Figure 20 shows that c_0 and $\frac{N_{c0}}{\Delta v_c}$ are roughly anticorrelated. The plot of their product shows that it is constant to within a factor of roughly 3 about some geometric mean. Consequently, restricting c_0 to some desired range can still yield physically reasonable fits. This will be examined in the next section.

In summary, the two-component, LVG models are reasonably good in explaining the r_{240} versus T_{dc} plot, which is in stark contrast to the one-component models. Examination of the systematic uncertainties suggests that ΔT and T_{d0} are known to within 1 K or better and n_{c1} is known to within a factor of 2 about some geometric mean. Other parameters like c_0 and $\frac{N_{c1}}{\Delta v_c}$ are known to within factors of 4 or 5 about a geometric mean, while the remaining component-0 parameters, $\frac{N_{c0}}{\Delta v_c}$ and n_{c0} can vary by factors of ~ 30 about the geometric mean. While a different class of two-component models could possibly explain the entire triangular cluster of points in the r_{240} versus T_{dc} plot, the two-component models described here only explain the triangular cluster for $T_{dc} \lesssim 18$ K. The points in the triangular cluster with $T_{dc} \gtrsim 19$ K are not accounted for with the current models. Another problem with the current models is that they predict area-filling factors that are unphysical for many of the observed positions. And this problem will be addressed in the following section.

3.4. Two-Component, Two-Subsample, Non-LTE Models and Results

As mentioned in the previous section, the two-component models suffer from a non-trivial physical drawback: the area-filling factors for some positions are greater than unity. Another problem is that the two-component models do not fit the $T_{dc} \geq 20$ K points well. As discussed in that section, keeping c_0 large enough will ensure that the filling factors have more reasonable values. Therefore, in this section we will consider models where c_0 is restricted to be ≥ 1 . To better fit $T_{dc} \geq 20$ K points, we divide the points into two subsamples: one subsample with $T_{dc} < 20$ K and the other with $T_{dc} \geq 20$ K. We fit the two-component, LVG models with $c_0 \geq 1$ *only* to the $T_{dc} < 20$ K subsample. The $T_{dc} \geq 20$ K subsample has a relatively simply trend and we need only fit the one-component models that were used in Section 3.2. Notice that we are relaxing the basic assumption somewhat: we are allowing parameters, in addition to T_d and T_K , to change from one subsample to

the other subsample. However, within each subsample we still impose the basic assumption. The parameter values resulting from the fits to the two subsamples are listed in Table 2. The resultant model curves are shown in Figure 23.

Casual inspection of the curves in Figure 23 suggests that these models better characterize the data than the simple two-component models of the previous section. However, the appropriate combination of the χ_ν^2 values in Table 2 into a reduced chi-square that characterizes *both* curves together yields $\chi_\nu^2 = 5.73$. Table 1 shows that the two-component models of the previous section yielded a best fit of $\chi_\nu^2 = 5.69$. Hence, the model curves for the two subsamples fit the data with essentially the same goodness of fit as for the simple two-component models. To be consistent with the two-component model fit to the $T_{\text{dc}} < 20$ K subsample, we could try to fit a two-component model to the $T_{\text{dc}} \geq 20$ K subsample. This two-component fit to the $T_{\text{dc}} < 20$ K subsample, when combined with that for the $T_{\text{dc}} \geq 20$ K subsample, gives an overall $\chi_\nu^2 = 5.34$. Again, this is *not* significantly better than the simple two-component models for the entire sample of points. Also, this model requires fixing T_{d0} at 18 K to get a reasonable fit. Therefore, only the one-component model fit to the $T_{\text{dc}} \geq 20$ K subsample is listed in Table 2 and is used in the column density and filling factor determinations.

If we consider only that the goodness of fit is no better and that extra model parameters are required, then the models discussed in this section should be ignored in favor of the two-component models for the entire sample of points. However, the two-component, two-subsample model described here has three important advantages. One is that the model fits the $T_{\text{dc}} \geq 20$ K points better. The second advantage is that the agreement between the dust-derived column densities, $N_{\text{d}}(\text{H})$, and the ^{13}CO -derived column densities, $N_{13}(\text{H I} + 2\text{H}_2)$, is noticeably improved. Figure 24 shows the plot of $N_{13}(\text{H I} + 2\text{H}_2)$ versus $N_{\text{d}}(\text{H})$. The χ_ν^2 of the straight line fit to the points in this plot is 5.3, compared with 7.4 in the corresponding plot for the simple two-component models. This an improvement with a 90% confidence level, according to the F-test.

Another advantage to the two-component, two-subsample models is seen in Figure 25, which shows the area-filling factors, $\eta_f(\nu)$, versus the ^{13}CO -derived molecular gas column densities, $N_{13}(\text{H}_2)$. The filling factors are now all (or almost all) less than or equal to unity, as desired. As was seen for the one-component models, the filling factors here again show saturation with increasing column density.

The uncertainties are estimated from the work of the previous sections. For the $T_{\text{dc}} < 20$ K subsample, the uncertainties of the two-component model parameters are largely systematic. As such, the uncertainties should be similar to those for the two-component models fitted to the entire sample of points (see previous section). However, our estimates of those

uncertainties for the component-1 density, n_{c1} must be modified. The previous section suggests that n_{c1} is known to within a factor of 2 about a geometric mean of possible densities. However, the n_{c1} for the current section is 2 orders of magnitude larger than for the previous section. Hence, we can only place a lower limit of $\sim \text{few} \times 10^2 \text{ cm}^{-3}$ on n_{c1} . We obtain a higher density value in the current section, possibly because the densities in the $T_{\text{dc}} < 20 \text{ K}$ subsample are 2 orders of magnitude higher than some kind of average density for the whole sample. Indeed, we find that the $T_{\text{dc}} \geq 20 \text{ K}$ subsample has a density that is lower by more than an order of magnitude. However, the $T_{\text{dc}} < 20 \text{ K}$ subsample has always dominated the results of the fits; the results obtained for this subsample are nearly identical to those for the whole sample. Therefore, this method likely places only a rough lower limit on the density. This is expected because the $^{13}\text{CO } J = 1 \rightarrow 0$ transition is insensitive to densities higher than about 10^3 cm^{-3} . Thus the uncertainties in the parameter values for the $T_{\text{dc}} < 20 \text{ K}$ subsample are the same as those for the entire sample points (see the previous section) with the exception that the component-1 density only has a lower limit of $\sim \text{few} \times 10^2 \text{ cm}^{-3}$.

The parameter uncertainties for the $T_{\text{dc}} \geq 20 \text{ K}$ subsample are again dominated by the systematics. The ΔT versus scale factor for the one-component models, i.e. Figure 16, shows that the fit to the $T_{\text{dc}} \geq 20 \text{ K}$ points varies from -10 to $+4 \text{ K}$. Hence we can say that $\Delta T = -3 \pm 7 \text{ K}$. This uncertainty is only slightly larger (i.e. less than a factor of 2) than the formal uncertainty given in Table 2. The plot of $N(^{13}\text{CO})/\Delta v$ versus scale factor suggests that only the formal uncertainties in $N(^{13}\text{CO})/\Delta v$ are important. However, the two-component model fitted to the $T_{\text{dc}} \geq 20 \text{ K}$ sample suggests larger systematic uncertainties. The $\frac{N_{c1}(^{13}\text{CO})}{\Delta v_c}$ value found (which corresponds to the $N(^{13}\text{CO})/\Delta v$ value in the one-component model) is less than a factor of 2 greater than the $N(^{13}\text{CO})/\Delta v$ value found for the one-component model. The systematic uncertainties (see the plot of $\frac{N_{c1}(^{13}\text{CO})}{\Delta v_c}$ versus scale factor in Figure 20) suggest that $N(^{13}\text{CO})/\Delta v$ varies between about 10^{15} and $10^{16} \text{ cm}^{-2} \cdot (\text{km} \cdot \text{s}^{-1})^{-1}$. (Recall that it cannot be lower than about $10^{15} \text{ cm}^{-2} \cdot (\text{km} \cdot \text{s}^{-1})^{-1}$ because the large-scale observed $N(^{13}\text{CO})/\Delta v$ represents a lower limit.) As for the systematic uncertainty of the density, Figure 16 suggests that, again, only a lower limit is applicable. This lower limit is $\sim 10^3 \text{ cm}^{-3}$. It is interesting that the two-component model results for the $T_{\text{dc}} \geq 20 \text{ K}$ subsample suggest a component-1 density identical to that of the one-component model fit.

One noticeable problem with the current models is the abrupt transition in the solid curve when crossing the $T_{\text{dc}} = 20 \text{ K}$ boundary. A more natural-looking curve would have a smooth transition across this boundary. Examination of the different parameter values for both subsamples suggests that gradually decreasing the $\frac{N_{c1}}{\Delta v_c}$ value by factors of 4 to 6 when going from the $T_{\text{dc}} < 20 \text{ K}$ subsample to the $T_{\text{dc}} \geq 20 \text{ K}$ subsample (thereby becoming the $N(^{13}\text{CO})/\Delta v$ value for the one-component model for the latter subsample) could possibly produce the desired smooth curve. Note that other solutions, such as varying n_{c1} would *not*

produce a satisfactory solution, because it would not merge well with the low- T_{dc} curve. Also, the component-0 parameters c_0 , $\frac{N_{\text{c}0}}{\Delta v_{\text{c}}}$, and $n_{\text{c}0}$ have little affect on the overall curve shape and are irrelevant for the $T_{\text{dc}} \geq 20$ K subsample. Therefore, the $T_{\text{dc}} \geq 20$ K subsample clumps are likely to have $N(^{13}\text{CO})/\Delta v$ values that are factors of a few lower than those in the $T_{\text{dc}} < 20$ K subsample.

The dashed curve on the $T_{\text{dc}} > 20$ K side of Figure 23 suggests another possibility. The current models do not account for the vertical spread of the points (neither in the $T_{\text{dc}} > 20$ K side nor in the triangular cluster mostly on the $T_{\text{dc}} < 20$ K side) in the r_{240} versus T_{dc} plot. Also, they do not account for the horizontal spread of the triangular cluster, although this spread is probably due to the large uncertainties in T_{dc} for some of these points. The dashed curve on the $T_{\text{dc}} > 20$ K side passes through the high- r_{240} . Accordingly, two or more subsamples could indeed account for these spreads *if* the curves for *all* the subsamples were applied to the whole range of observed color temperatures. However, what is the optimum way of separating these two (or more) subsamples? Separating them according to dust temperature is simplistic: the $T_{\text{dc}} \geq 20$ K solution, for example, does not pass through points on the $T_{\text{dc}} < 20$ K side (i.e. the dashed line on that side) that are far from the $T_{\text{dc}} < 20$ K solution (the solid curve on that side). The optimum separation of these subsamples would involve two (or more) curves for the whole color temperature range of that would correctly characterize all the points in the plot. In other words, the basic assumption in its simplest form is not correct. Nonetheless, the basic assumption imposed within each subsample would simplify the modeling. For now, we keep the current two-component, two-subsample model parameters because they represent an adequate characterization of the data.

In summary, the two-component, two-subsample models produce a similarly good fit to the r_{240} versus T_{dc} plot as the simple two-component models, but fix the problems of the unphysical filling factors and the poor fit to the high- T_{d} points. Also, the dust-derived and ^{13}CO -derived column densities agree better for these two-subsample models than for the models fitted to the whole sample. Also, the current two-component, two-subsample models hint that the optimum choice of subsamples has yet to be found. This will be left to future work.

3.5. The Fiducial Points

As a rough illustration of the limitations of the basic assumption and of the modeling, a few reference or fiducial points were chosen in the r_{240} versus T_{dc} plots. These points roughly follow the overall shape of the sample in these plots. Specifically, four of the fiducial points approximately represent the corners and centroid of the triangular cluster of points and the

other three fiducial points represent the overall trend in the high- T_{dc} branch. The fiducial points are represented as diamonds in the r_{240} versus T_{dc} plots (i.e., Figures 6, 7, 8, 12, 13, 14, 15, ??, 19, and 23). Table 3 lists the fiducial points (in order of increasing T_{dc}) and the physical properties that pertain to each. Because of the basic assumption, the derived physical properties would be the same for all the points (except T_{K} and T_{d}). However, when a high- T_{dc} solution was found, as for all but the LVG two-component case, the physical conditions derived for the four fiducial points with $T_{\text{dc}} \geq 20$ K were those of the high- T_{dc} solution. The table lists these physical conditions for the four cases of the previous sections:

- Case 1: LTE, one-component models.
- Case 2: LVG, one-component models.
- Case 3: LVG, two-component models.
- Case 4: LVG, two-component, two-subsample models.

Despite representing overall trends, the fiducial points do not necessarily represent the sample as a whole: e.g., the second, third, and fifth points as listed in Table 3, which have distances of 3 or more sigmas from the best-fitting model curves. The deviations of these three points from each model curve are not just statistical uncertainties; the models used here simply cannot account for the total vertical spread of the points in the sample. The basic assumption does not allow models that would “fill” the space occupied by the sample of points in the r_{240} versus T_{dc} plot. One alternative is to have two or three of these two-component model curves fit to all the sample simultaneously. In practice, this is time-consuming and is left to a later date.

3.6. Masses

The derived column densities now allow us to estimate the masses of the Orion clouds. Maps of the column densities are presented in Figures 26 to 28. Figure 26 shows the column density maps derived from the observations using the LVG, one-component model results, Figure 27 the analogous maps for the two-component, two-subsample case, and Figure 28 the maps of column density for just component 1 on those lines of sight where this component has a temperature of 10 K or less (i.e., $T_{\text{d1}} = T_{\text{K1}} \leq 10$ K). The maps of column densities for the LTE case are not shown, because they closely resemble the maps of the LVG, one-component case. The upper panel in each of these figures shows the continuum-derived (dust-derived) gas column densities and each lower panel shows the ^{13}CO -derived gas column densities. Summing these column densities appropriately and using the adopted distance of 450 pc gives the masses (*not* including Helium) listed in Tables 4, 5, 6, and 7. The random uncertainties in these masses are small: relative uncertainties of the order of 0.5% for the continuum-derived masses, 0.25% for the ^{12}CO -derived masses, and 6.5% for the ^{13}CO -derived masses

(although the smaller Orion Nebula and NGC 2024 Fields have relative uncertainties of 20% for the ^{13}CO -derived masses). The systematic uncertainties (i.e., the uncertainties due to calibration and background-subtraction uncertainties) are more appreciable: 30% for the continuum-derived masses and 20% for the ^{13}CO -derived masses. The model results in each of the four cases were combined with the ^{13}CO $J = 1 \rightarrow 0$ and HI observations to yield the column densities, as described previously, and these were summed to yield the masses in the tables.

All the ^{13}CO -derived column density maps show a plateau with steep edges. This plateau is roughly 20° wide in longitude and about 6° in latitude. For example, one of the edges of this plateau can be seen running from galactic longitude 216° to 208° at latitude -10.25° . These are approximately the mapped area in ^{13}CO . Specifically, these edges occur just inside the mapped area’s edges, where the observed ^{13}CO $J = 1 \rightarrow 0$ line strength falls to zero. These plateau edges are also partly visible in the upper panel of Figure 27, even though this panel does not have the ^{13}CO -derived column densities. This is because these “observed” column densities depend on the two-component, two-subsample model results, which, in turn, require knowledge of the ^{13}CO line strengths. This model dependence is especially true of the cold gas column density maps in Figure 27, resulting in the clear visibility of the plateau edges in the northward and eastward (i.e. towards the top and left) directions. The southward and westward edges are the arbitrary boundaries imposed by selecting only those lines of sight with $T_{\text{d1}} \leq 10$ K; column densities of component 1 on lines of sight with $T_{\text{d1}} > 10$ K are set to zero.

There are apparent discrepancies between the derived masses (i.e. Tables 4 and 5) and the column density versus column density plots (i.e., Figures 10, 17, 21, and 24). For example, the ratio of the ^{12}CO -derived masses in Table 4 compared to the continuum-derived masses of Cases 1 & 2 in Table 5 is 1.08, whereas the linear fit in the lower panel of Figure 10 suggests a ratio of 1.40. There are two reasons for the discrepancy that are related to the signal-to-noise ratio of the observations. One reason is that the plot of column densities in Figure 10 only considers positions with high signal-to-noise data (i.e. more than $5\text{-}\sigma$ in ^{12}CO $J = 1 \rightarrow 0$ and in the continuum bands). If all the positions in the Orion fields were included in the plot, the slope would change to about 1.3. The rest of the discrepancy is because of the difference between the slope of a line from linear regression and the ratio of the averages of the ordinate values and abscissa values. The former represents a sum of values that are weighted by $1/\sigma^2$ and divided by another sum of similarly weighted values. Determining the total masses by simply summing the column densities in the fields and dividing by another similarly determined sum represents the latter. In other words, the masses in the tables are not determined from weighted sums, whereas the slopes in the column density plots are indeed determined from such sums. Therefore, the slopes in the

column density plots are biased toward the points with higher signal-to-noise ratios *even* when these plots include the low signal-to-noise ratio points. This discrepancy in the ratio between the tables and the plots is simply a consequence of the scatter of the points in these plots. If there were less scatter, then the tables and the plots would give similar ratios for the ^{12}CO -derived over continuum-derived masses (assuming similar coverage in both types of maps). This affects the accuracy of our X-factor estimates. The slope from the lower panel of Figure 10 suggests an X-factor of $1.9 \times 10^{20} \text{ cm}^{-2} \cdot (\text{K} \cdot \text{km} \cdot \text{s}^{-1})^{-1}$, whereas comparing the total masses in the tables for the one-component cases suggests an X-factor of $2.4 \times 10^{20} \text{ cm}^{-2} \cdot (\text{K} \cdot \text{km} \cdot \text{s}^{-1})^{-1}$. Combining these two numbers gives an estimate of the X-factor of $(2.1 \pm 0.3) \times 10^{20} \text{ cm}^{-2} \cdot (\text{K} \cdot \text{km} \cdot \text{s}^{-1})^{-1}$. This is an uncertainty of about $\pm 15\%$. Thus specifying the X-factor to greater accuracy (i.e., a smaller uncertainty) is meaningless.

An interesting, but crude, comparison can be made with the Orion X-factor estimated from Figure 8 of Dame et al. (2001). In that figure, the predicted $\text{I}(\text{CO})$ profile that cuts along the Orion region is *on average* about 20-30% higher than that of the observed profile. Accordingly, the predicted X-factor of $1.8 \times 10^{20} \text{ cm}^{-2} \cdot (\text{K} \cdot \text{km} \cdot \text{s}^{-1})^{-1}$ for the entire Galaxy must be increased by factors of about 1.2 to 1.3 to give the *average* X-factor for Orion. This gives an average X-factor for Orion of about $2.2\text{-}2.3 \times 10^{20} \text{ cm}^{-2} \cdot (\text{K} \cdot \text{km} \cdot \text{s}^{-1})^{-1}$. This is consistent with the value derived above.

There is another apparent discrepancy between the plots and the tables; the total masses derived from ^{13}CO (i.e., in Table 4) disagree with those derived from the continuum (i.e., in Table 5). In this case, the ratios derived from the tables are more extreme (i.e., further from 1) than from the column density plots. The problem here is that the ^{13}CO map does not cover the full area covered by the continuum maps. This results in two problems: a problem with the continuum-derived gas masses and a problem with the ^{13}CO -derived gas masses. The former problem is that the two-component-model results cannot give the continuum-derived gas column densities outside the area mapped in ^{13}CO . Specifically, an observed data point in the r_{240} versus T_{dc} plot *cannot* be associated with a point on the theoretical curve, because the observed data point *cannot* even be placed in this plot without knowing the ^{13}CO $J = 1 \rightarrow 0$ line strength. Consequently, the correction factor in equation (40) is assumed to be unity (i.e., $N_{\text{d}}(\text{H}) = N_{\text{d1}}(\text{H})$ is assumed) for those positions outside the area mapped in ^{13}CO $J = 1 \rightarrow 0$. The latter problem is that the ^{13}CO observations alone do *not* yield accurate *total* masses for these clouds; the mass estimates from ^{13}CO $J = 1 \rightarrow 0$ must be corrected for the missing coverage towards the edges of the clouds. These corrections were estimated by determining the total of the gas masses of the three big fields from the continuum observations for *only those positions inside the* $\text{I}(^{13}\text{CO}) = 0$ *contour* for each of the four cases (where Cases 1 and 2 are identical for the continuum-derived masses). These were then compared with the continuum-derived masses for all the gas in those fields (i.e.,

the numbers listed as “Total” in Table 5).

Before discussing this comparison, assessing the accuracy of this method is possible by comparing the continuum-derived masses inside the $I(^{13}\text{CO}) = 0$ contour with the ^{13}CO -derived masses in Table 4. These latter masses represent, in practice, the molecular gas mass inside the $I(^{13}\text{CO}) = 0$ contour plus the HI mass throughout the entire Orion fields. That is, the masses listed in the “Case 1”, “Case 2”, “Case 3”, and “Case 4” columns of Table 4 are the ^{13}CO -derived molecular gas masses within the $I(^{13}\text{CO}) = 0$ contour plus the HI mass both inside and outside this contour. Therefore, to assess the accuracy of this correction for the lack of ^{13}CO coverage, the continuum-derived masses inside this contour must be corrected upwards for the HI mass that lies outside this contour. This HI mass is $34000 M_{\odot}$. After adding this mass to the continuum-derived masses inside the $I(^{13}\text{CO}) = 0$ contour, the continuum-derived masses agree with the ^{13}CO -derived masses of Table 4 to within 5 to 10%, depending on the case.

Now to correct the total masses in Table 4 for the gas mass that is missing outside the $I(^{13}\text{CO}) = 0$ contour, we compare the continuum-derived masses within this contour with the masses in Table 5. This gives mass differences of $88000 M_{\odot}$ in the one-component cases and $87000 M_{\odot}$ in the two-component cases. Allowing again for the $34000 M_{\odot}$ of HI outside the $I(^{13}\text{CO}) = 0$ contour that is already implicit in Table 4 requires the masses in Table 4 to be corrected upwards by $54000 M_{\odot}$ in the one-component cases and by $53000 M_{\odot}$ in the two-component cases. The resultant best estimates for the Orion gas masses in the one-component case (for Case 2) and in the two-component case (for Case 4) are in Table 6, where the continuum-derived and ^{13}CO -derived masses agree to within about 5%.

Table 7 shows that roughly 40 to 50% of the two-component gas mass is in the form of cold ($T_{\text{K}} < 10 \text{ K}$) gas (compare with Table 5). Consequently, the mass of gas or dust being detected at wavelengths much more sensitive to warm, rather than cold, gas or dust (e.g., in the Wien limit) must be corrected upward by a factor of at least 1.6. Figure 28 shows that the cold component is on one edge of each of the small 2° HII-region fields (i.e. Orion Nebula and NGC 2024 Fields) and is spread out along the northern edge of the Orion B Field. There is also some cold dust towards the north-eastern edge of the λ Orionis Field. A natural question at this point is about a realistic lower limit to the temperature: are gas and dust temperatures as low as 3 K really necessary for explaining the data? To test this, two-component models were applied, where T_{K1} was restricted to be $\geq 10 \text{ K}$. This gave $\Delta T = -7 \text{ K}$ and $\chi^2_{\nu} = 10.5$. In other words, the minimum T_{d1} was *still* found to be 3 K. Also, the χ^2 is a factor of 1.9 higher than the best fit models that had no such restriction on T_{K1} . This is a worse fit at the 99% confidence level. Restricting *both* T_{d1} and T_{K1} would have given an even worse fit. A less extreme restriction on T_{K1} of $T_{\text{K1}} \geq 5 \text{ K}$ gives $\Delta T = -2 \text{ K}$

and $\chi^2_\nu = 7.7$. This fit is worse at almost the 90% confidence level and *again* the minimum T_{d1} is 3 K. In short, avoiding having at least some dust or gas with temperatures near 3 K is very difficult, provided that the basic assumption is valid. Further discussion of this is deferred to Paper III (Wall 2006a).

Since the failings of the basic assumption could be relevant here, longer-wavelength observations confirming the existence of such cold gas or dust would be helpful. The longer wavelength *FIRAS* data were used to test this, but the results were inconclusive. The *FIRAS* data extend to a wavelength of about 4 mm, making them much less sensitive to the warm dust and, as such, much less *insensitive* to the cold dust. However, the *FIRAS* data also have a spatial resolution of 7° ; the *FIRAS* beam solid angle is a *factor of 100 larger* than that of the *DIRBE* beam. Consequently, a direct comparison with the *DIRBE* data and the Orion fields as defined here is difficult. Nevertheless, such a comparison was attempted as follows:

1. The spectra for 183 positions towards and around the Orion fields were obtained. Each position had two spectra: a low-frequency spectrum and a high-frequency spectrum. These were joined to form a single spectrum. Data in the channels that overlapped between the two spectra were averaged with $1/\sigma^2$ weights. This yields spectra that cover frequencies of from 68 to 2911 GHz (i.e. wavelengths from 4410 to $103\ \mu\text{m}$) with channels 13.6 GHz wide.
2. The 60 highest frequency channels were then binned into 5 channels to improve the signal-to-noise ratio. The 12 channels that went into each of the 5 new channels were averaged with $1/\sigma^2$ weights.
3. A background with the form $I_{BG} = a_0 + a_1 \csc(b_{eff})$ was fitted to each channel from those positions outside the Orion fields and farther than half a *FIRAS* beam from the Galactic plane. The a_0 represents an isotropic background component and is the cosmic background radiation. The a_1 represents a scaling factor for the Galactic plane emission. The b_{eff} is the effective Galactic latitude for emission that follows a cosecant(b) law averaged within the *FIRAS* beam. Specifically, $b_{eff} \equiv \arccsc(\langle \csc(b) \rangle)$ where $\langle \csc(b) \rangle$ is the average of $\csc(b)$ within the 7° tophat beam of *FIRAS*. A good empirical approximation to b_{eff} is $b_{eff} = |b| - 5|b|^{-1.15}$ for $|b|$ in the range of 4° to 27° . After determining the best fit a_0 and a_1 values for all the channels, the resultant background spectrum was subtracted from the *FIRAS* spectra centered on the Orion field centers.
4. Two-component models of modified blackbodies were fitted to the background-subtracted spectra. These were of the form $I_\nu = \tau_a(\nu/\nu_0)^\beta B_\nu(T_{da}) +$

$\tau_b(\nu/\nu_0)^\beta B_\nu(T_{db})$, where τ_a and τ_b are the optical depths of components a and b , respectively, at reference frequency ν_0 .

The best fitting curves had a warm component with temperatures between 17 and 20 K. The cold component was very hard to define. Assuming that this component even exists, the temperature is around 5 K, but could not be pinned down. Because of this temperature uncertainty, placing limits on the cold component mass was difficult. The cold-component mass was anywhere between 0 and 10 times the warm-component mass. In any event, confirming the existence of this cold dust must await long-wavelength spectra with greater spatial resolution and sufficient spatial and wavelength coverage.

4. Summary and Discussion

We used the $240\ \mu\text{m}$ continuum to the $^{13}\text{CO}\ J = 1 \rightarrow 0$ intensity ratio plotted against the $140\ \mu\text{m}/240\ \mu\text{m}$ dust color as a diagnostic of the dust and gas physical conditions in the Orion A and B molecular clouds. Model curves were fitted to the data with orthogonal regression. Two sets of one-component models were applied to the data: Local Thermodynamic Equilibrium (LTE) and Large Velocity Gradient (LVG). Two sets of two-component models were also applied to the data: two-component, LVG models and two-component, two-subsample, LVG models. In each case, the model fit gave the conversion of the observed intensities into gas/dust column densities and beam-area filling factors. The results of the fitting are summarized below:

- *One-Component, LTE Models:* These models fit the data only poorly with a reduced chi-square of $\chi_\nu^2 = 16.5$. When considering systematic uncertainties, the only parameter to be fitted, ΔT , was very poorly determined: ΔT lies anywhere between $-24\ \text{K}$ and $+6\ \text{K}$. Comparison of the continuum-derived gas column densities with those derived from the $^{13}\text{CO}\ J = 1 \rightarrow 0$ spectral line showed considerable scatter with $\chi_\nu^2 = 16.6$. The filling factors exhibit an understandable increase with increasing column density and are all less than unity. At best, the one-component, LTE models only crudely reproduce the overall trend in the data.
- *One-Component, LVG Models:* These models also fit the data only poorly with a reduced chi-square of $\chi_\nu^2 = 16.9$. When considering systematic uncertainties, the ΔT was again very poorly determined: ΔT lies anywhere between $-14\ \text{K}$ and $-1\ \text{K}$. Comparison of the continuum-derived versus spectral line-derived gas column densities showed comparable scatter to the LTE model case, with $\chi_\nu^2 = 15.5$. The filling factors behaved

similar to those in the case of the LTE modeling. The LVG model results overall are, at best, only marginally better than the single-component, LTE models.

- *Two-Component, LVG Models:* In contrast to the one-component models, these models explain the overall trend in the data with $\chi^2_\nu = 5.7$; this is better than the one-component models at a confidence level of better than 99.9% according to the F-test. Also in contrast to the one-component model results, ΔT is known to be within 1 K of 0 K even when the systematic uncertainties are considered. The component-0 dust temperature *seems* to be accurately known and is consistent with the large-scale interstellar radiation field, i.e. 18 K. Other parameters, such as gas densities and column densities per velocity interval, are known from factors of a few to more than an order of magnitude about some geometric mean. The continuum-derived versus spectral line-derived gas column densities showed much better agreement for these models than for the one-component component models, the former having $\chi^2_\nu = 7.4$. Despite their advantages, these models suffer from two problems. The first is that many of the filling factors have unphysical values — i.e., greater than unity. The second problem is that the model curves do not fit well to the data with 140 μm /240 μm color temperatures greater than 20 K.
- *Two-Component, Two-Subsample, LVG Models:* Here the sample of data points was split into two subsamples: one with dust color temperatures < 20 K and the other with such temperatures \geq 20 K. These models have all the advantages of the simpler two-component models described previously, and also fix the problems of the unphysical filling factors and the poor fit to the data points with 140 μm /240 μm color temperatures \geq 20 K. The only disadvantage is that this approach is ad hoc. Nevertheless, the derived parameter values agree with those of the simpler two-component models to within the systematic uncertainties.
- *Cloud Masses:* After correcting for systematic effects, such as the lack of coverage of the ^{13}CO $J = 1 \rightarrow 0$ map, the total *hydrogen* gas mass derived in the Orion fields is $4.2 \times 10^5 M_\odot$, as found in the more realistic two-component case (and is $2.5 \times 10^5 M_\odot$ for the less realistic one-component case). Due to the systematics, the uncertainty in this mass is $\pm 40\%$. The extra mass in the two-component case is due to the apparent presence of cold dust/gas with temperatures of 3-10 K. Attempting to confirm the existence of this cold dust/gas with the long-wavelength FIRAS data was inconclusive due to the insufficient spatial resolution.

The above results have a number of astronomical implications, which are mentioned here only briefly:

1. *Dust Temperatures Equal to Gas Temperatures:* If this surprising result applies to the gas and dust on large scales in our Galaxy, then models of gas-to-dust thermal coupling must be revised. Having dust and gas temperatures equal on galactic scales implies that large-scale molecular gas temperatures are nearly double the temperatures previously believed (i.e. closer to 20 K than to 10 K). Also, one dust grain alignment mechanism would be ruled out.
2. *Cold Gas/Dust:* If similar two-component models are correct and are applicable to other large clouds in the Galaxy, then the total mass of molecular gas in the Galaxy must be revised upwards by about 60%.
3. *Millimeter Continuum to ^{13}CO $J = 1 \rightarrow 0$ Line Ratio as a Temperature Diagnostic:* For the millimeter continuum to ^{13}CO $J = 1 \rightarrow 0$ intensity ratio above some threshold, this ratio can serve as a diagnostic of the gas/dust temperature, even in the high-temperature limit.
4. *X-Factor:* An improved explanation for the X-factor is applicable. This will be discussed in detail in Wall (2006b).

Discussing the above results in depth would be premature at this point. We must first examine the modeling and various systematic effects more carefully. Even though we have tested the effects of some systematics on the model curves (i.e., by applying scale factors or changing the starting grid when fitting the models), we need to find and understand any inherent biases or flaws that the model fitting may have. For example, the two-component models consistently find a ΔT equal to or near 0 K, in spite of the scale factor applied to the data. Is this because the dust-gas temperature difference really is zero? Or is it simply because these models are biased towards $\Delta T = 0$ K despite its true value? And what of the reliability of the other parameter values? The component-1 density, for example, is supposed to be known to within a factor of a few of $600 \text{ H}_2 \text{ cm}^{-3}$, according to the simple two-component models (see Figure 20). And yet, the two-subsample, two-component models suggest densities that are one to three orders of magnitude higher than this. Clearly, the methods used thus far to examine the systematics are incomplete. Consequently, Paper II examines the results of running the models on simulated data and will answer the concerns raised here.

In addition to those concerns, there are other questions not yet addressed by the methods used here. Specifically, what is the effect of the background subtractions used? How will dust associated with HI affect the results? Does changing the spectral emissivity index β appreciably affect the results? Are there alternative kinds of models that would also explain the data? The cloud positions modeled here only represent 26% of the area of the Orion

clouds; how representative are the results of the clouds as a whole? Paper III examines these questions.

All these questions and concerns are addressed in Papers II and III. Paper III also discusses the scientific implications of the results in more detail.

This work was supported by CONACyT grants #211290-5-0008PE and #202-PY.44676 to W. F. W. at *INAOE*. I am very grateful to W. T. Reach for his comments and support. I owe a great debt of thanks to Y. Fukui and T. Nagahama of Nagoya University for supplying us with the ^{13}CO data that made this work possible. The author is grateful to R. Maddalena and T. Dame, who supplied the map of the peak ^{12}CO $J = 1 \rightarrow 0$ line strengths and provided important calibration information. I thank D. H. Hughes, W. T. Reach, Y. Fukui, M. Greenberg, T. A. .D. Paglione, G. MacLeod, E. Vazquez Semadeni, and others for stimulating and useful discussions.

A. Column Densities from Optically Thin Rotational Lines of CO

In this appendix, the relationship between the molecular gas column density and integrated line strength of an optically thin rotational line of CO, or one of its isotopologues, is derived. The derivation detailed below is more appropriately applied to the isotopologues of CO, such as ^{13}CO and C^{18}O , than to CO itself (i.e. $^{12}\text{C}^{16}\text{O}$), because the low- J lines of CO (i.e. $J = 1 \rightarrow 0$, $2 \rightarrow 1$, $3 \rightarrow 2$) are usually optically thick, whereas the corresponding lines of its isotopologues are usually optically thin for molecular gas on the scales of many parsecs. Such a derivation is helpful for a number of reasons. One reason is that this relationship is central to this paper and knowing which approximations were *not* used, as well as which ones were used, is important. Another reason is that the full derivation is difficult to find in the literature. Furthermore, aside from the usual assumptions made in determining column densities (i.e., optically thin line, non-varying gas physical conditions along the line of sight, and sometimes LTE), the equations in the literature are sometimes based on additional invalid or unnecessary assumptions. For example, the Rayleigh-Jeans approximation is sometimes used and is *both* invalid *and* unnecessary. (Ironically enough, using the Rayleigh-Jeans approximation actually results in a more complicated expression than *not* using this approximation.)

The optical depth of the $J \rightarrow J - 1$ rotational transition, $\tau_\nu(J \rightarrow J - 1)$, is related to the volume absorption coefficient, $\kappa_\nu(J \rightarrow J - 1)$, by

$$\tau_\nu(J \rightarrow J - 1) = \int \kappa_\nu(J \rightarrow J - 1) \, ds \quad (\text{A1})$$

or

$$\tau_\nu(J \rightarrow J-1) = \frac{1}{4\pi} \int \left(B_{J-1,J} n_{J-1} - B_{J,J-1} n_J \right) h\nu_{J,J-1} \phi_\nu(J \rightarrow J-1) ds \quad . \quad (\text{A2})$$

The integral is over the line of sight through the cloud. The n_{J-1} and n_J are the volume densities of those CO molecules in the $J-1$ and J rotational levels, respectively. The $B_{J-1,J}$ and $B_{J,J-1}$ are the Einstein B-coefficients defined in terms of the mean intensity of the radiation field, rather than in terms of the energy density. The $B_{J-1,J}$ is the absorption rate coefficient for absorptions from level $J-1$ to level J . The $B_{J,J-1}$ is the rate coefficient for stimulated emission from level J to level $J-1$ and is the stimulated emission correction to the optical depth in equation (A2). The $h\nu_{J,J-1}$ is the energy difference between levels $J-1$ and J , where h is Planck's constant and $\nu_{J,J-1}$ is the frequency of the $J \rightarrow J-1$ transition. The quantity $\phi_\nu(J \rightarrow J-1)$ is the line profile function in terms of frequency, ν . It is normalized such that

$$\int_{\text{spectral line}} \phi_\nu(J \rightarrow J-1) d\nu = 1 \quad . \quad (\text{A3})$$

The integration in (A2) converts the volume densities, n_{J-1} and n_J , into the corresponding column densities, N_{J-1} and N_J , yielding

$$\tau_\nu(J \rightarrow J-1) = \frac{1}{4\pi} \left(B_{J-1,J} N_{J-1} - B_{J,J-1} N_J \right) h\nu_{J,J-1} \phi_\nu(J \rightarrow J-1) \quad . \quad (\text{A4})$$

Note that the assumption of LTE has not been used. Similarly, assuming constant gas physical properties along the line of sight has not been applied. (Strictly speaking, the line profile function can change along the line of sight. Nevertheless, the $\phi_\nu(J \rightarrow J-1)$ that appears in A4 is the appropriately weighted average along the line of sight of the $\phi_\nu(J \rightarrow J-1)$ that appears in A2.) The following relations eliminate the Einstein B-coefficients in favor of the spontaneous emission rate coefficient, $A_{J,J-1}$:

$$B_{J-1,J} = \frac{g_J}{g_{J-1}} B_{J,J-1} \quad (\text{A5a})$$

and

$$B_{J,J-1} = \frac{c^2}{2h\nu_{J,J-1}^3} A_{J,J-1} \quad , \quad (\text{A5b})$$

where c is the speed of light and g_J and g_{J-1} are the degeneracies of levels J and $J-1$, respectively. Using (A5a) and (A5b), equation (A4) becomes,

$$\tau_\nu(J \rightarrow J-1) = \frac{c^2}{8\pi\nu_{J,J-1}^2} g_J A_{J,J-1} \left(\frac{N_{J-1}}{g_{J-1}} - \frac{N_J}{g_J} \right) \phi_\nu(J \rightarrow J-1) \quad . \quad (\text{A6})$$

The frequency profile function, $\phi_\nu(J \rightarrow J-1)$, is replaced with the velocity profile function, $\phi_v(J \rightarrow J-1)$. Since $\phi_\nu(J \rightarrow J-1) d\nu = \phi_v(J \rightarrow J-1) dv$, $\phi_\nu(J \rightarrow J-1) = \lambda_{J,J-1} \phi_v(J \rightarrow J-1)$, where $\lambda_{J,J-1}$ is the wavelength of the $J \rightarrow J-1$ transition. Substituting this into (A6) yields

$$\tau_v(J \rightarrow J-1) = \frac{g_J A_{J,J-1} \lambda_{J,J-1}^3}{8\pi} \frac{N_{J-1}}{g_{J-1}} \left(1 - \frac{N_J}{N_{J-1}} \frac{g_{J-1}}{g_J} \right) \phi_v(J \rightarrow J-1) \quad . \quad (\text{A7})$$

The excitation temperature between levels J and $J-1$, $T_x(J \rightarrow J-1)$, is defined by

$$\frac{n_J}{n_{J-1}} = \frac{g_J}{g_{J-1}} \exp\left(-\frac{h\nu_{J,J-1}}{kT_x(J \rightarrow J-1)}\right) \quad , \quad (\text{A8})$$

where k is Boltzmann’s constant. Up to now, the assumption of constant gas physical properties along the line of sight and the assumption of LTE have not been used.

The term “excitation temperature” is often used incorrectly in the literature. Under the assumptions of some optical depth limit and LTE, a ratio of two molecular lines gives a temperature. In the LTE limit, this line-ratio temperature is the kinetic temperature of the gas. However, it is often called the “excitation temperature of the gas”, as though excitation temperature is a physical property of the gas itself, like kinetic temperature, rather than a parameter determined *by* the physical properties. The excitation temperature properly represents the population ratio of two *particular* levels of a *particular* molecule and *not* a physical property that characterizes all the levels of all the molecules in a region of a molecular cloud. A line-ratio temperature represents three or four levels and is *not* an excitation temperature, but depends on the *two* excitation temperatures of the lines forming the ratio (as well as their optical depths). In general, temperatures from line ratios and the excitation temperatures of the various transitions are numerically distinct from one another, except in the limits of either low or high density. In the former case, all excitation temperatures equalize to the temperature of the ambient radiation field (i.e., the cosmic background temperature in the absence of other sources) and the temperatures derived from line ratios are equal to this temperature. In the latter case, all the excitation and line ratio temperatures are the same as the kinetic temperature of the gas. As such, many articles actually mean “line-ratio temperature” or “kinetic temperature” when they say “excitation temperature”. In particular, the term “kinetic temperature” is appropriate when such articles compute column densities from a *single* optically thin rotational line of CO. Unless a non-LTE radiative transfer code (e.g., the Large Velocity Gradient or LVG code) is used, along with some constraints on the gas physical conditions, to explicitly consider the excitation temperature variation with position in the rotational ladder, the excitation temperatures are implicitly assumed to be *numerically* constant throughout the rotational ladder in computing the partition function. Therefore, this adopted and unvarying (with J)

excitation temperature is actually the adopted kinetic temperature (or the temperature of the ambient radiation field in the case of very low density).

Now the gas physical conditions are assumed constant along the line of sight, so that $N_J/N_{J-1} = n_J/n_{J-1}$. Substituting (A8) into (A7), integrating over the line velocity profile, and rearranging gives

$$N_{J-1} = \frac{8\pi g_{J-1}}{g_J A_{J,J-1} \lambda_{J,J-1}^3} \left[1 - \exp\left(-\frac{h\nu_{J,J-1}}{kT_x(J \rightarrow J-1)}\right) \right]^{-1} \int_{\text{spectral line}} \tau_v(J \rightarrow J-1) dv \quad , \quad (\text{A9})$$

where we used the normalization condition (A3), but applied to ϕ_v instead of ϕ_ν . Following Kutner and Ulich (1981), the radiation temperature, T_R , which is the brightness temperature defined in the Rayleigh-Jeans sense (as opposed to the Planck sense), is given by

$$\begin{aligned} T_R(J \rightarrow J-1) &= \frac{h\nu_{J,J-1}}{k} \left\{ \left[\exp\left(\frac{h\nu_{J,J-1}}{kT_x(J \rightarrow J-1)}\right) - 1 \right]^{-1} \right. \\ &\quad \left. - \left[\exp\left(\frac{h\nu_{J,J-1}}{kT_{BG}}\right) - 1 \right]^{-1} \right\} \left[1 - \exp(-\tau_v(J \rightarrow J-1)) \right] \quad , \quad (\text{A10}) \end{aligned}$$

where T_{BG} is the cosmic background temperature. Note that, even though this is a Rayleigh-Jean brightness temperature, the Rayleigh-Jeans approximation is not used. For optically thin lines, (A10) can be rewritten as

$$\frac{kT_R(J \rightarrow J-1)}{h\nu_{J,J-1}} = \left[\exp\left(\frac{h\nu_{J,J-1}}{kT_x(J \rightarrow J-1)}\right) - 1 \right]^{-1} \tau_v(J \rightarrow J-1) C_{BG} \quad , \quad (\text{A11})$$

where C_{BG} is a correction for the cosmic background radiation and is given by

$$C_{BG} = 1 - \frac{\exp\left(\frac{h\nu_{J,J-1}}{kT_x(J \rightarrow J-1)}\right) - 1}{\exp\left(\frac{h\nu_{J,J-1}}{kT_{BG}}\right) - 1} \quad . \quad (\text{A12})$$

Notice that this correction factor is zero when $T_x(J \rightarrow J-1) = T_{BG}$, because a line with an excitation temperature equal to that of the cosmic background is not seen against this background.

Many expressions in the literature for CO column density implicitly assume that C_{BG} is unity. This is a reasonable assumption when $T_x(J \rightarrow J-1)$ is appreciably greater than T_{BG} . For example, for the $^{13}\text{CO } J = 1 \rightarrow 0$ line ($\nu_{10} = 110.201$ GHz) the $T_x(1 \rightarrow 0)$ is probably

close to the kinetic temperature, T_K , which is often no lower than 10 K in most cases. For $T_K = 10$ K, $C_{BG} = 0.88$, thereby affecting the column density derivation by about 12%. For most purposes, this accuracy is sufficient and is even better at higher temperatures: for $T_K = 15$ K, $C_{BG} = 0.93$ and for $T_K = 20$ K, $C_{BG} = 0.95$. The accuracy is also better at higher frequencies: for the ^{13}CO $J = 2 \rightarrow 1$ line ($\nu_{10} = 220.399$ GHz), again adopting $T_x(2 \rightarrow 1) = T_K$ for simplicity, the $C_{BG} = 0.96, 0.98, 0.99$ for $T_K = 10, 15,$ and 20 K, respectively. Nevertheless, for the work described in this paper, the C_{BG} correction was included in the computations.

Rearranging (A11) gives

$$\left[1 - \exp\left(-\frac{h\nu_{J,J-1}}{kT_x(J \rightarrow J-1)}\right) \right]^{-1} \tau_v(J \rightarrow J-1) = \frac{kT_R(J \rightarrow J-1)}{h\nu_{J,J-1} C_{BG}} \exp\left(\frac{h\nu_{J,J-1}}{kT_x(J \rightarrow J-1)}\right) . \quad (\text{A13})$$

Substituting (A13) into (A9) results in

$$N_{J-1} = \frac{8\pi g_{J-1}}{g_J A_{J,J-1} \lambda_{J,J-1}^3} \frac{k}{h\nu_{J,J-1} C_{BG}} \exp\left(\frac{h\nu_{J,J-1}}{kT_x(J \rightarrow J-1)}\right) \int T_R(J \rightarrow J-1) dv . \quad (\text{A14})$$

The excitation temperature, $T_x(J \rightarrow J-1)$, is not known in general, but is now eliminated by using (A8) and the expression $N_J/N_{J-1} = n_J/n_{J-1}$:

$$N_J = \frac{8\pi}{A_{J,J-1} \lambda_{J,J-1}^3} \frac{k}{h\nu_{J,J-1} C_{BG}} \int T_R(J \rightarrow J-1) dv . \quad (\text{A15})$$

Even though $T_x(J \rightarrow J-1)$ is still implicitly present in C_{BG} , the dependence of C_{BG} on $T_x(J \rightarrow J-1)$ is very weak for $T_x(J \rightarrow J-1) \gg T_{BG}$.

Equation (A15) can be simplified further using

$$A_{J,J-1} = \frac{64\pi^4 \nu_{J,J-1}^3}{3hc^3} \left(\frac{J}{2J+1}\right) \mu^2 , \quad (\text{A16})$$

where μ is the permanent dipole moment of the molecule. This is 0.11 Debye for CO, where 1 Debye = 10^{-18} esu·cm in CGS units or 3.33564×10^{-30} m·C in SI units (see CRC Handbook of Chemistry and Physics 1998-99). The energy above the ground state of level J , $h\nu_{J,0}$, is well represented by

$$h\nu_{J,0} = hB J(J+1) , \quad (\text{A17})$$

where B is the rotational constant of the molecule (not to be confused with the Einstein B -coefficients). From (A17) it follows that

$$\nu_{J,J-1} = 2BJ \quad . \quad (\text{A18})$$

Equations (A17) and (A18) assume that the molecule is a rigid rotor and neglect the effects of centrifugal stretching. Nevertheless, (A18) gives the correct observed frequencies of the rotational lines of CO up to the $J = 10 \rightarrow 9$ line to within 0.06% or better. (Note that this is still *very inaccurate* for obtaining radial velocities during actual observations, but is more than sufficient accuracy for column density determinations.) Using (A18), the rotational constant can be easily determined from $B = \nu_{10}/2$, where ν_{10} is the observed frequency of the $J = 1 \rightarrow 0$ line. For CO and its isotopologues, these values are $B(\text{CO}) = 57.64 \text{ GHz}$, $B(^{13}\text{CO}) = 55.10 \text{ GHz}$, and $B(\text{C}^{18}\text{O}) = 54.89 \text{ GHz}$. Equation(A16) is now written as

$$A_{J,J-1} = \frac{512\pi^4 B^3}{3hc^3} \left(\frac{J^4}{2J+1} \right) \mu^2 \quad . \quad (\text{A19})$$

The $\leq 0.06\%$ accuracy of expression (A18) *would* limit the accuracy of (A19) to no more than about 0.2%, except that the accuracy of (A19) *is currently* limited by the uncertainty in the dipole moment, μ . The uncertainty in $\mu(\text{CO})$ is about 10%, giving a 20% uncertainty in $A_{J,J-1}$ for CO (see CRC Handbook of Chemistry and Physics and references therein).

Substituting equations (A19) and (A18) into (A15) yields the useful expression

$$N_J = \frac{3k(2J+1)}{16\pi^3 B J^2 \mu^2 C_{\text{BG}}} I_{J,J-1} \quad , \quad (\text{A20})$$

where $I_{J,J-1} = \int T_{\text{R}}(J \rightarrow J-1) dv$ is often called the integrated intensity of the line (although it is really the velocity-integrated radiation temperature of the line). Normally, CGS units are used, but $I_{J,J-1}$ is in units of $\text{K} \cdot \text{km} \cdot \text{s}^{-1}$; consequently (A20) becomes

$$N_J = \frac{3k(2J+1)}{16\pi^3 B J^2 \mu^2 C_{\text{BG}}} \cdot 10^5 \cdot I_{J,J-1} (\text{K} \cdot \text{km} \cdot \text{s}^{-1}) \quad , \quad (\text{A20a})$$

where all quantities with units, except $I_{J,J-1}$, are in CGS units. So far, the gas physical conditions have been assumed constant along the line of sight. LTE has not yet been assumed. Therefore, for general non-LTE conditions, the total column density $N(\text{CO})$ can be estimated by observing a number of optically thin rotational lines of CO, using (A20a) to determine the column density in the upper levels of the observed transitions, and sum the N_J values. This sum must then be corrected for the column densities in the upper levels of unobserved transitions and for the column density in the ground state, N_0 . (Notice that A20a is not

defined for N_0 .) As such, the fraction of the total column density in the ground state and in the upper levels of unobserved lines must be estimated by modeling the physical conditions from the observed line ratios. This fraction then corrects the sum of the observed N_J values to an estimate of the true $N(\text{CO})$.

When only one or two optically thin lines of CO are observed, LTE is often assumed. Notice from (A19) that the spontaneous emission rates are lowest for the lowest-J transitions, implying that these lines are closest to LTE. So if the lines observed are low-J lines like $J = 1 \rightarrow 0$ or $J = 2 \rightarrow 1$, then the LTE assumption might reasonably estimate the total CO column density from the integrated intensity of a single observed line. The total column density of CO is given by

$$N(\text{CO}) = \sum_{J'=0}^{\infty} N_{J'} = N_J \left(\frac{N_0}{N_J} \right) \sum_{J'=0}^{\infty} \frac{N_{J'}}{N_0} \quad . \quad (\text{A21})$$

The J in this expression is the upper-J of the observed transition. Replacing all occurrences of $J-1$ in (A8) by 0 and, because LTE is now assumed, replacing $T_x(J \rightarrow J-1)$ by the kinetic temperature, T_K , for all J , converts (A21) to

$$N(\text{CO}) = \frac{N_J}{2J+1} Q(T_K) \exp\left(\frac{h\nu_{J,0}}{kT_K}\right) \quad . \quad (\text{A22})$$

(A22) uses $g_J = 2J+1$ and $g_0 = 1$. The $Q(T_K)$ is the rotational partition function given by

$$Q(T_K) = \sum_{J'=0}^{\infty} (2J'+1) \exp\left(-\frac{hBJ'(J'+1)}{kT_K}\right) \quad , \quad (\text{A23})$$

where (A17) was used. When the kinetic temperature is high enough, the summation variable, J' , can be treated as a continuous variable (i.e. real instead of integral) and the summation in (A23) is treated as an integral over J' . This gives the simplified, but approximate,

$$Q(T_K) \simeq \frac{kT_K}{hB} \quad . \quad (\text{A24})$$

For CO, ^{13}CO , and C^{18}O , (A24) is $T_K/2.766$, $T_K/2.644$, and $T_K/2.634$, respectively.

As is the case for the cosmic background correction factor, C_{BG} , the approximate form of the partition function, (A24), is often used in the literature. Again, this approximate form is appropriate most of the time, because usually $T_K \gg hB/k$. For $T_K = 10, 15$, and 20 K , the ratios of the approximate $Q(T_K)$, given by (A24), to the exact $Q(T_K)$, given by (A23), are 0.91, 0.94, and 0.96, respectively. Again, for the work described in this paper, the

approximate form was *not* used. It is easy to see why: the effects of neglecting the cosmic background correction and using the approximate rotational partition function reinforce each other and result in a theoretical $I(^{13}\text{CO})$ (for the $J = 1 \rightarrow 0$ line) that is too high by 14% at $T_K = 15$ K. This is non-negligible for the work here.

Substituting (A17) and (A20) into (A22) results in

$$N(\text{CO}) = \frac{3k}{16\pi^3 B J^2 \mu^2 C_{\text{BG}}} Q(T_K) \exp\left(\frac{hB J(J+1)}{kT_K}\right) I_{J,J-1} \quad . \quad (\text{A25})$$

Using the same units as in (A20a) gives

$$N(\text{CO}) = \frac{3 \times 10^5 k}{16\pi^3 B J^2 \mu^2 C_{\text{BG}}} Q(T_K) \exp\left(\frac{hB J(J+1)}{kT_K}\right) I_{J,J-1} (\text{K} \cdot \text{km} \cdot \text{s}^{-1}) \quad , \quad (\text{A25a})$$

where $N(\text{CO})$ is in units of CO molecules per cm^2 . Note that the C_{BG} that appears in (A25) and (A25a) is now a function of T_K instead of $T_x(J \rightarrow J-1)$. Substituting in the fundamental physical constants gives

$$N(\text{CO}) = 6.90 \times 10^{24} \frac{Q(T_K)}{B J^2 C_{\text{BG}}} \exp\left(4.80 \times 10^{-11} \frac{B J(J+1)}{T_K}\right) I_{J,J-1} (\text{K} \cdot \text{km} \cdot \text{s}^{-1}) \quad . \quad (\text{A26})$$

Choosing a particular isotopologue of CO, ^{13}CO , then applying the value for the rotational constant for ^{13}CO results in

$$N(^{13}\text{CO}) = 1.25 \times 10^{14} \frac{Q(T_K)}{J^2 C_{\text{BG}}} \exp\left(2.64 \frac{J(J+1)}{T_K}\right) I_{J,J-1}(^{13}\text{CO}) \quad , \quad (\text{A27})$$

where $I_{J,J-1}(^{13}\text{CO})$ is still in units of $\text{K} \cdot \text{km} \cdot \text{s}^{-1}$. Equation (A27) is used in the current paper for determining the molecular gas column densities in the LTE case. When $T_K \gg 2.644$ K, (A27) can be simplified using the asymptotic form for $Q(T_K)$, (A24), and $C_{\text{BG}} \simeq 1$ so that

$$N(^{13}\text{CO}) = 4.73 \times 10^{13} \frac{T_K}{J^2} \exp\left(2.64 \frac{J(J+1)}{T_K}\right) I_{J,J-1}(^{13}\text{CO}) \quad . \quad (\text{A28})$$

Note that (A28) was not used in the current paper, but is still a useful approximation: the upward corrections for this equation are 14%, 6.5%, and 1.8% for $T_K = 15, 30$, and 100 K, respectively.

Using the appropriate abundances with (A26) and (A27) allows determination of $N(\text{H}_2)$. Reasonable values for these abundances are $X(^{12}\text{CO}) = 8 \times 10^{-5}$, $X(^{12}\text{CO})/X(^{13}\text{CO}) = 25$ to 65, and $X(^{13}\text{CO})/X(\text{C}^{18}\text{O}) = 5$ to 6 (e.g., Encrenaz et al. 1975; Dickman 1975; Knapp & Jura

1976; Frerking et al. 1982; Langer & Penzias 1990; Taylor & Dickman 1989). Note that the abundances of the isotopologues near cloud surfaces can be different from the numbers given here, which are the abundances for cloud interiors (see, e.g., Taylor & Dickman 1989; Frerking et al. 1982). Simply dividing the CO column density by the abundance can give a reasonable estimate of $N(\text{H}_2)$, but Frerking et al. (1982) find that a zero-point $N(\text{H}_2)$ must also be added to explain their observations of the Taurus and ρ Ophiuci molecular clouds. Such a zero-point column density was not used in the current work because it varies by a factor of a few from cloud to cloud (see Frerking et al. 1982) and because it would make little difference to the results and conclusions. For the ^{13}CO abundance, we adopt $X(^{12}\text{CO})/X(^{13}\text{CO}) = 63$. This is an average of the value observed at the position (0.5, 2.5) observed by Langer & Penzias (1990) and the interpolated value expected for the galactocentric radius of the Orion clouds (see their Figure 6). This average is probably more representative of the Orion clouds as a whole and only differs by 6% from the observed value at position (0.5, 2.5). Note that the observed value at the (0,0) is probably peculiar because it lies within a region with strong UV fields (see Langer & Penzias 1990).

Briefly discussing other approaches for determining column densities with optically thin CO lines is worthwhile. For example, sometimes the Rayleigh-Jeans approximation is used. In that case, the excitation temperature of the transition is assumed to be sufficiently large that the approximation $h\nu_{J,J-1}/kT_x(J \rightarrow J-1) \ll 1$ is valid. Equation (A11) would have the much simpler form,

$$T_R(J \rightarrow J-1) \simeq T_x(J \rightarrow J-1)\tau_\nu(J \rightarrow J-1) \quad (\text{A29})$$

However, adopting this simpler expression actually complicates the final formula (i.e., A25) for the column density because the $[1 - \exp(-h\nu_{J,J-1}/kT_x(J \rightarrow J-1))]^{-1}$ factor is not replaced with a simpler form. Consequently, the LTE expression (A25) has an additional factor, $(h\nu_{J,J-1}/kT_K) [\exp(h\nu_{J,J-1}/kT_K) - 1]^{-1}$. For some reason, this additional factor is retained, even though the Rayleigh-Jeans approximation used to validate the use of (A29) requires its replacement with *unity*. Because the high- T_K limit applies, C_{BG} is set to 1 and the approximation for the partition function, (A24), is used. The latter allows cancellation of the extra T_K^{-1} . The resultant expression reasonably estimates the column density only in the high- T_K , low- J limit. The ratios of the column density derived from the expression using the Rayleigh-Jeans approximation to that of (A25) for the ^{13}CO $J = 1 \rightarrow 0$ line are 0.61, 0.79, 0.86, and 0.91 for $T_K = 10, 20, 30$, and 50 K, respectively. For the ^{13}CO $J = 2 \rightarrow 1$ line the corresponding ratios are 0.49, 0.72, 0.80, and 0.88. For the ^{13}CO $J = 3 \rightarrow 2$ line these ratios are 0.37, 0.63, 0.74, and 0.83. If column density estimates within a factor of 2 of those from (A25) are considered acceptable, then, even for the rather common kinetic temperature of 10 K, the estimates based on the Rayleigh-Jeans approximation are unacceptable for all transitions higher than $J = 1 \rightarrow 0$. Even for $J = 1 \rightarrow 0$, the column density estimate

must be corrected upwards by 64%. A similarly large upward correction, 59%, is necessary even for a kinetic temperature of 20 K for the $J = 3 \rightarrow 2$ line. Avoiding the Rayleigh-Jeans approximation keeps the final expression more accurate *and* less complicated. (Of course, if the Rayleigh-Jeans approximation is applied correctly, then the additional factor is unity anyway. The resultant expression *would* be correct in the high- T_K limit, where C_{BG} is set to unity, which is appropriate for this limit.)

Another approach is to use the corresponding line of ^{12}CO , which is optically thick, assume LTE and that the gas fills the beam in the velocity interval about the ^{12}CO line peak, and solve for the optical depth $\tau(^{13}\text{CO})$ or $\tau(\text{C}^{18}\text{O})$ from the $^{13}\text{CO}/^{12}\text{CO}$ or $\text{C}^{18}\text{O}/^{12}\text{CO}$ intensity ratios. In addition, the ^{12}CO line peak intensity estimates the gas kinetic temperature. (Note that this is often inappropriately referred to as the “excitation temperature”. It is inappropriate because LTE was assumed in computing τ and in the expression for the column density.) The optical depth, kinetic temperature, and line velocity-width are then used in an LTE expression for the column density that assumes the high- T_K limit for the rotational partition function. This method has the advantages that assuming the optically thin limit is not necessary and that the additional information provided by the ^{12}CO line is used. However, it also has the disadvantages that the high- T_K limit for the partition function is used and that the gas fills beam in the interval about the ^{12}CO line peak is assumed. The former assumption does not produce very large errors: even down to $T_K = 2.8$ K, the upward correction to the column density found from using the full partition function is only 40%. The latter assumption is likely wrong for external galaxy observations, because the molecular gas is unlikely to fill the beam in any single velocity interval. (As discussed in this paper, it is also likely wrong for observations of Galactic molecular clouds, but may still be roughly correct to within a factor of about 2.) In fact, this assumption can lead, in certain cases, to column density estimates that are wrong by factors of a few or more. If we consider a few cases with $I(\text{C}^{18}\text{O } J = 1 \rightarrow 0)$ a factor of 20 down from $I(^{12}\text{CO } J = 1 \rightarrow 0)$ and if $T_R(^{12}\text{CO } J = 1 \rightarrow 0)$ is weak, then the column density estimates are too high by factors of 2 to 5. For example, if the filling factor in each velocity interval is 0.1 and if $T_R(^{12}\text{CO } J = 1 \rightarrow 0) = 0.1$ K, the column density estimate is too high by a factor of 5. Even in the less extreme case of $T_R(^{12}\text{CO } J = 1 \rightarrow 0) = 0.5$ K and a filling factor of 0.2, the estimate is too high by a factor of 2. Even if $T_R(^{12}\text{CO } J = 1 \rightarrow 0)$ is much stronger, 10 K, the estimate is still a factor of 2 too high for a filling factor of 0.1. Despite this shortcoming, the correction factor to the column density estimate is often much less extreme than the filling factor itself. In any event, this method is easily improved by appropriate application of the filling factor to the equations used to derive the optical depth, kinetic temperature, and the column density itself.

One final point is that elaborate non-LTE radiative transfer models suggest that LTE-

derived CO column densities can be underestimates of the true column densities by factors of 1.3 to 7 (Padoan et al. 2000). As shown in the current paper, the assumption of LTE can indeed underestimate the true column density; similar factors are derived using much simpler two-component models that employ the LVG code.

B. Ratio of the Submillimeter or Millimeter Continuum to an Optically Thin ^{13}CO Rotational Line in the LTE Case

The optically thin continuum emission of the dust has a specific intensity, I_ν , given by

$$I_\nu = \tau_\nu B_\nu(T_d) \quad . \quad (\text{B1})$$

The dust optical depth τ_ν is given by

$$\tau_\nu = \kappa_\nu x_d \mu_H m_H N(\text{H}) \quad , \quad (\text{B2})$$

where κ_ν is the dust mass absorption coefficient at frequency ν , μ_H is the correction for the presence of helium, x_d is the dust-to-gas mass ratio (where “gas” means hydrogen and helium), m_H is the hydrogen atom mass, and $N(\text{H})$ is the column density of hydrogen nuclei. Specifically,

$$N(\text{H}) = N(\text{H I}) + 2N(\text{H}_2) \quad , \quad (\text{B3})$$

where $N(\text{H I})$ is the column density of atomic hydrogen and $N(\text{H}_2)$ is the column density of molecular hydrogen. Substituting (B2) into (B1), using the explicit form for the Planck function, and converting from cgs units to $\text{MJy} \cdot \text{sr}^{-1}$ yields

$$I_\nu (\text{MJy} \cdot \text{sr}^{-1}) = 2 \times 10^{17} \frac{h\nu^3 \kappa_\nu x_d \mu_H m_H}{c^2 [\exp(\frac{h\nu}{kT_d}) - 1]} N(\text{H}) \quad . \quad (\text{B4})$$

The mass absorption coefficient at frequency ν expressed in terms of that coefficient at a reference frequency ν_0 is

$$\kappa_\nu = \left(\frac{\nu}{\nu_0} \right)^\beta \kappa_{\nu_0} \quad , \quad (\text{B5})$$

where β is the spectral emissivity index of the dust. Substituting (B5) into (B4) gives

$$I_\nu (\text{MJy} \cdot \text{sr}^{-1}) = 2 \times 10^{17} \frac{h\nu^{3+\beta} \kappa_{\nu_0} x_d \mu_H m_H}{\nu_0^\beta c^2 [\exp(\frac{h\nu}{kT_d}) - 1]} N(\text{H}) \quad . \quad (\text{B6})$$

Now that the continuum intensity is expressed in terms of temperature and column density, the same must be done for the ^{13}CO rotational line. In the LTE, optically thin case,

such an equation is simply the rearrangement of (A25a). At this point the assumption $N(\text{HI}) = 0$ is adopted because the molecular gas column densities dominate for the majority of the positions studied here. (Nonetheless, there are positions for which the atomic gas column density is appreciable, introducing possible complications in the interpretation of the results. These complications are examined in detail in Paper III.) Applying the abundance of ^{13}CO to change $N(^{13}\text{CO})$ to $N(\text{H}_2)$, using (B3) with $N(\text{HI}) = 0$ to change $N(\text{H}_2)$ to $N(\text{H})$, and rearranging (A25a) results in

$$I_{J,J-1}(^{13}\text{CO}) = \frac{8\pi^3 B J^2 \mu^2 C_{\text{BG}} X(^{13}\text{CO})}{3 \times 10^5 \text{ kQ}(T_{\text{K}})} \exp\left(-\frac{h B J(J+1)}{k T_{\text{K}}}\right) N(\text{H}) \quad , \quad (\text{B7})$$

where $I_{J,J-1}(^{13}\text{CO})$ is in units of $\text{K} \cdot \text{km} \cdot \text{s}^{-1}$. Dividing (B6) by (B7) gives

$$r_{\nu_j} \equiv \frac{I_{\nu}(\text{MJy} \cdot \text{sr}^{-1})}{I_{J,J-1}(^{13}\text{CO})} = 7.5 \times 10^{21} \frac{h k \nu^{3+\beta} \kappa_{\nu 0} x_d \mu_H m_H Q(T_{\text{K}})}{\pi^3 B J^2 \mu^2 \nu_0^\beta C_{\text{BG}} X(^{13}\text{CO}) c^2} \frac{\exp\left(\frac{h B J(J+1)}{k T_{\text{K}}}\right)}{\exp\left(\frac{h \nu}{k T_d}\right) - 1} \quad , \quad (\text{B8})$$

where r_{ν_j} is in units of $\text{MJy} \cdot \text{sr}^{-1} \cdot (\text{K} \cdot \text{km} \cdot \text{s}^{-1})^{-1}$. Substituting in the fundamental physical constants and for the rotational constant of ^{13}CO ,

$$r_{\lambda_j} = 1.67 \times 10^4 \frac{\lambda_0^\beta(\mu\text{m}) \kappa_{\nu 0} x_d \mu_H Q(T_{\text{K}})}{\lambda^{3+\beta}(\mu\text{m}) J^2 X(^{13}\text{CO}) C_{\text{BG}}} \frac{\exp\left(\frac{2.64 J(J+1)}{T_{\text{K}}}\right)}{\exp\left(\frac{1.44 \times 10^4}{\lambda(\mu\text{m}) T_d}\right) - 1} \quad , \quad (\text{B9})$$

where $\lambda_0(\mu\text{m})$ and $\lambda(\mu\text{m})$ are the wavelengths in μm corresponding to frequencies ν_0 and ν , respectively. Note that r_{λ_j} is still in units of $\text{MJy} \cdot \text{sr}^{-1} \cdot (\text{K} \cdot \text{km} \cdot \text{s}^{-1})^{-1}$. Although not explicitly stated in every case in W96, that paper adopted the following values: $\kappa_{\nu 0} = 40 \text{ cm}^2/\text{g}$ for ν_0 corresponding to $\lambda_0 = 100 \mu\text{m}$, $x_d = 0.0075$, $\mu_H = 1.4$, and $\beta = 2$. $X(^{12}\text{CO})/X(^{13}\text{CO}) = 63$ was adopted for the ^{13}CO abundance (see Appendix A), so that equation (B9) becomes

$$r_{\lambda_j} = 5.51 \times 10^{13} \frac{Q(T_{\text{K}})}{\lambda^5(\mu\text{m}) J^2 C_{\text{BG}}} \frac{\exp\left(\frac{2.64 J(J+1)}{T_{\text{K}}}\right)}{\exp\left(\frac{1.44 \times 10^4}{\lambda(\mu\text{m}) T_d}\right) - 1} \quad . \quad (\text{B10})$$

If λ is set to $240 \mu\text{m}$ and J to 1, then

$$r_{240} = 69.2 \frac{Q(T_{\text{K}})}{C_{\text{BG}}} \frac{\exp\left(\frac{5.28}{T_{\text{K}}}\right)}{\exp\left(\frac{59.9}{T_d}\right) - 1} \quad , \quad (\text{B11})$$

where the second subscript on the r (i.e. the J) was dropped for clarity. Equation (B11) is used in the current paper for the LTE modeling of the continuum to line ratio as a function of T_d .

It is interesting to examine the behavior of r_{240} in the low- and high-temperature limits. For simplicity we assume that T_d and T_K are the same and equal to some T . We also assume that $T \gg 2.644$ in both the low- and high- T limits, so that the simpler form of the partition function, (A24), can be used and so that $C_{BG} \simeq 1$. The low- T limit means that $T \ll 59.9$ K and so

$$r_{240} = 26.2 \, T \exp\left(-\frac{54.6}{T}\right) \quad . \quad (B12)$$

The upward correction to this formula is 16% and 23% at $T=15$ K and 30 K, respectively. The high- T limit is where $T \gg 59.9$ K and we have

$$r_{240} = 0.437 \, T^2 \quad . \quad (B13)$$

The downward correction to this formula is 20% at $T=100$ K. In short, the continuum to line ratio has a strong Wien-like rise at low temperatures and a *relatively* weaker T^2 rise at high temperatures. This high-temperature rise is still very strong compared to that of ratios of CO rotational lines from the same isotopologue and to that of ratios of continuum intensities at two different wavelengths.

C. Uncertainty Analysis of the LTE Derivation of the ^{13}CO Column Density

To derive the uncertainty in the ^{13}CO column density in the LTE case, we start with equation (A27) with $J=1$:

$$N(^{13}\text{CO}) = N_0 \, Q(T_K) \, C_{BG}^{-1}(T_K) \exp\left(\frac{T_{10}}{T_K}\right) I(^{13}\text{CO}) \quad , \quad (C1)$$

where $N_0 = 1.25 \times 10^{14}$ and $T_{10} = h\nu_{10}/k = 5.28$ K. The uncertainty in the derived column density, $\sigma(N)$, is given by

$$\sigma^2(N) = \left(\frac{\partial N}{\partial T_K}\right)^2 \sigma^2(T_K) + \left(\frac{\partial N}{\partial I}\right)^2 \sigma^2(I) \quad , \quad (C2)$$

Substituting equation (C1) into (C2) and then dividing by (C2) yields

$$\frac{\sigma^2(N)}{N^2} = \left(\frac{T_K \, Q'(T_K)}{Q(T_K)} - \frac{T_K \, C'_{BG}(T_K)}{C_{BG}} - \frac{T_{10}}{T_K}\right)^2 \frac{\sigma^2(T_K)}{T_K^2} + \frac{\sigma^2(I)}{I^2} \quad . \quad (C3)$$

Differentiating (A12) gives $C'_{BG}(T_K)$:

$$C'_{BG}(T_K) = \frac{\frac{T_{10}}{T_K^2} \exp\left(\frac{T_{10}}{T_K}\right)}{\exp\left(\frac{T_{10}}{T_{BG}}\right) - 1} \quad . \quad (C4)$$

Similarly, differentiating (A23) gives $Q'(T_K)$:

$$Q'(T_K) = \frac{B_T}{T_K^2} \sum_{J=1}^{\infty} J(J+1)(2J+1) \exp\left(-\frac{B_T J(J+1)}{T_K}\right) , \quad (C5)$$

where $B_T = hB/k = 2.64 \text{ K}$ and is the molecular rotational constant in units of Kelvins. To simplify the above expression, only the first two terms in the summation are necessary at low temperatures, i.e. $T_K < 2B_T$, to achieve 5% accuracy or better. At high temperatures, i.e. $T_K \geq 2B_T$, the approximate expression (A24) can be used. This results in the following approximations for $Q'(T_K)$:

$$Q'(T_K) = \frac{B_T}{T_K^2} \sum_{J=1}^2 J(J+1)(2J+1) \exp\left(-\frac{B_T J(J+1)}{T_K}\right) , \quad T_K < 2B_T \quad (C6a)$$

$$Q'(T_K) = \frac{1}{B_T} , \quad T_K \geq 2B_T . \quad (C6b)$$

The error in this approximation is no worse than 5% for T_K just below $2B_T$ or 5.28 K and better than this at higher and lower temperatures. The uncertainty in T_K itself, $\sigma(T_K)$, is

$$\sigma^2(T_K) = \sigma^2(T_d) + \sigma^2(\Delta T) . \quad (C7)$$

Therefore, the uncertainty in the derived ^{13}CO column density is given by equation (C3), with equations (C4), (C5), (C6b), (C6b), and (C7) substituted in.

D. Uncertainty Analysis of the Column Density Derived from the Dust Continuum Emission

The Wien limit is used for estimating the uncertainties in the dust-derived column densities. Combining equations (B1) and (B2) and using the Wien approximation gives

$$N = I_\nu D \exp\left(\frac{F}{T_d}\right) , \quad (D1)$$

where $D = [(2h\nu^3/c^2)\kappa_\nu\mu_H m_H x_d]^{-1}$ and $F = h\nu/k$. The uncertainty in the dust-derived column density, $\sigma(N)$, is

$$\sigma^2(N) = \left(\frac{\partial N}{\partial I_\nu}\right)^2 \sigma^2(I_\nu) + \left(\frac{\partial N}{\partial T_d}\right)^2 \sigma^2(T_d) . \quad (D2)$$

Evaluating (D2) using (D1) and then dividing by (D1) results in

$$\frac{\sigma^2(N)}{N^2} = \frac{\sigma^2(I_\nu)}{I_\nu^2} + \frac{\sigma^2(T_d)}{T_d^2} \frac{F^2}{T_d^2} . \quad (D3)$$

For ν corresponding to $\lambda = 240 \mu\text{m}$, $F = 60.0 \text{ K}$. Equation (5) gives $\sigma(T_d)$.

E. Uncertainty Analysis of the LVG Derivation of the ^{13}CO Column Density

As stated in Section 3.2, the column density of molecular gas derived from the ^{13}CO $J = 1 \rightarrow 0$ line, $N_{13}(\text{H}_2)$, using LVG model results can be written as

$$y = R(a_1, a_2, a_3; x_1, x_2, x_3) x_3 , \quad (E1)$$

where

$$y \equiv N(^{13}\text{CO}) \quad (E2)$$

and

$$R(a_1, a_2, a_3; x_1, x_2, x_3) \equiv \frac{[N(^{13}\text{CO})/\Delta v]_{mod}}{[T_R(^{13}\text{CO } J = 1 \rightarrow 0)]_{mod}} \quad (E3)$$

The $[N(^{13}\text{CO})/\Delta v]_{mod}$ and $[T_R(^{13}\text{CO } J = 1 \rightarrow 0)]_{mod}$ are the column density per velocity interval and radiation temperature of the ^{13}CO $J = 1 \rightarrow 0$ line, respectively, from the model fit. Just as there is a family of model curves of r_{240} versus T_d , the $R(a_1, a_2, a_3; x_1, x_2, x_3)$ can be thought of as a family of curves where each R is given by a particular model r_{240} . The $\{a_i\}$ are the curve parameters that specify a particular R curve from the family of R curves and the $\{x_i\}$ specify, *indirectly*, a particular point on that curve. Specifically, the $\{a_i\}$ are

$$a_1 \equiv \Delta T = T_d - T_K , \quad (E4a)$$

$$a_2 \equiv \left[\frac{N(^{13}\text{CO})}{\Delta v} \right]_{mod} , \quad (E4b)$$

and

$$a_3 \equiv [n(\text{H}_2)]_{mod} . \quad (E4c)$$

The $\{x_i\}$ represent a particular observed data point and that point is associated with the point on the R versus T_d curve that is closest to it, where

$$x_1 \equiv T_d , \quad (E5a)$$

$$x_2 \equiv I_\nu(240 \mu\text{m}) , \quad (E5b)$$

and

$$x_3 \equiv I(^{13}\text{CO}) \quad . \quad (\text{E5c})$$

The uncertainty in the derived column density, $\sigma(y)$, is given by

$$\sigma^2(y) = \sum_{i=1}^3 \left(\frac{\partial y}{\partial a_i} \right)^2 \sigma^2(a_i) + \sum_{i=1}^3 \left(\frac{\partial y}{\partial x_i} \right)^2 \sigma^2(x_i) \quad (\text{E6})$$

The first summation in (E6) represents the contribution of the model-fit uncertainties to the computed column density uncertainty. The second summation in (E6) represents the contribution of the observational uncertainties to the computed column density uncertainty. Specifically, the observational uncertainties result in uncertainties in choosing the nearest point on the model curve. To evaluate equation (E6), we will use $r = x_2/x_3$, where the subscript “240” on the r was dropped for brevity. This gives us

$$\frac{\partial y}{\partial a_i} = \frac{\partial R}{\partial a_i} x_3 \quad (\text{E7a})$$

$$\frac{\partial y}{\partial x_1} = \frac{\partial R}{\partial x_1} x_3 \quad (\text{E7b})$$

$$\begin{aligned} \frac{\partial y}{\partial x_2} &= \frac{\partial R}{\partial x_2} x_3 \\ &= \left(\frac{\partial R}{\partial r} \frac{\partial r}{\partial x_2} \right) x_3 \\ &= \frac{\partial R}{\partial r} \end{aligned} \quad (\text{E7c})$$

$$\begin{aligned} \frac{\partial y}{\partial x_3} &= \frac{\partial R}{\partial x_3} x_3 + R \\ &= \left(\frac{\partial R}{\partial r} \frac{\partial r}{\partial x_3} \right) x_3 + R \\ &= -\frac{\partial R}{\partial r} r + R \quad . \end{aligned} \quad (\text{E7d})$$

Substituting equations (E7a) through (E7d) into (E6) yields

$$\begin{aligned} \sigma^2(y) &= \left[\sum_{i=1}^3 \left(\frac{\partial R}{\partial a_i} \right)^2 x_3^2 \sigma^2(a_i) \right] + \left(\frac{\partial R}{\partial x_1} \right)^2 x_3^2 \sigma^2(x_1) + \left(\frac{\partial R}{\partial r} \right)^2 \sigma^2(x_2) \\ &\quad + \left[\left(\frac{\partial R}{\partial r} \right)^2 r^2 - 2rR \left(\frac{\partial R}{\partial r} \right) + R^2 \right] \sigma^2(x_3) \end{aligned} \quad (\text{E8})$$

Employing

$$\sigma^2(r) = r^2 \left(\frac{\sigma^2(x_2)}{x_2^2} + \frac{\sigma^2(x_3)}{x_3^2} \right) \quad (\text{E9})$$

changes (E8) to

$$\begin{aligned} \sigma^2(y) = & \left[\sum_{i=1}^3 \left(\frac{\partial R}{\partial a_i} \right)^2 \sigma^2(a_i) \right] x_3^2 + \left[\left(\frac{\partial R}{\partial x_1} \right)^2 \sigma^2(x_1) + \left(\frac{\partial R}{\partial r} \right)^2 \sigma^2(r) \right] x_3^2 \\ & + \left[R^2 - 2rR \left(\frac{\partial R}{\partial r} \right) \right] \sigma^2(x_3) \end{aligned} \quad (\text{E10})$$

Equation (E10) has the advantage that there is no explicit dependence on $\sigma(x_2)$, $\partial R/\partial x_2$, nor $\partial R/\partial x_3$. Instead, there is an explicit dependence on r and on $\sigma(r)$, both of which have already been computed for the LTE modeling. Equation (E10) was used in determining the uncertainties in the derived column densities.

We must now compute the derivatives of R . The derivatives with respect to the a_i , $\partial R/\partial a_i$, are determined from the difference in R , ΔR , that results for a given difference in a specific a_i , Δa_i , from the family of model curves. In other words, the following approximation is used:

$$\frac{\partial R}{\partial a_i} \simeq \frac{\Delta R}{\Delta a_i} \quad (\text{E11})$$

The uncertainties in the $\sigma(a_i)$ were determined by finding the values of a_i that resulted in the total χ^2 rising by a value of χ_ν^2 , since this value was greater than 1 (see discussion of this in Section 3.1). Since the model curves were on a grid, changes in a_i occur in discrete jumps that increase χ^2 by amounts less than or greater than χ_ν^2 . For Figure 16, the error bars represent the *minimum* change in a_i that increased χ^2 by *more* than χ_ν^2 . The $\sigma(a_i)$ used for deriving $\sigma(y)$ was the change in a_i interpolated linearly between the grid points that gave the appropriate increase in χ^2 . Where there was a limit instead of an upper (lower) error bar, an error bar the same size as the lower (upper) error bar was assumed.

The derivatives $\partial R/\partial x_1$ and $\partial R/\partial r$ are with respect to the *observed* x_1 (i.e., T_d) and the *observed* r (i.e., $I_\nu(240\mu\text{m})/I(^{13}\text{CO})$). The former derivative is the amount that R changes when the observed x_1 changes (for fixed r). In other words, when a point in the r versus x_1 plot changes in x_1 , the closest point on the model curve to this point will also change, thereby changing R . The latter derivative is similar, but with r in place of x_1 . Determining the closest point on the model curve to the observed data point requires defining distances in the r versus x_1 plane. The distance from any observed point can be defined by normalizing changes in x_1 to its observational uncertainty, $\sigma(x_1)$, and changes in r to $\sigma(r)$. Thus we define a coordinate system for a given data point as

$$X \equiv \frac{x_1}{\sigma(x_1)} \quad (\text{E12a})$$

$$Y \equiv \frac{r}{\sigma(r)} \quad . \quad (\text{E12b})$$

The distance between the data point and a point on the model curve is simply $(X_d - X_c)^2 + (Y_d - Y_c)^2$, where (X_d, Y_d) are the data point coordinates and (X_c, Y_c) are the coordinates of a point on the model curve. Because the curve is a smooth curve, it can be approximated by a straight line in an interval that is sufficiently small. The interval of interest is one centered on the point on the curve closest to the data point. Varying the X_d of the data point, while holding Y_d constant, or vice versa, then varies the coordinates of nearest point on the curve. The variations of these coordinates, $(\Delta X_c, \Delta Y_c)$, are related to the data point coordinate variations by

$$\Delta X_d = \frac{\Delta X_c^2 + \Delta Y_c^2}{\Delta X_c} \quad (\text{E13a})$$

for constant ΔY_d and

$$\Delta Y_d = \frac{\Delta X_c^2 + \Delta Y_c^2}{\Delta Y_c} \quad (\text{E13b})$$

for constant ΔX_d . The $\Delta X_d, \Delta Y_d$ are the data point coordinate variations corresponding to variations $\Delta X_c, \Delta Y_c$. Equations (E13a) and (E13b) were derived with simple trigonometry. Using equations (E12a) and (E12b), equations (E13a) and (E13b) become

$$(\Delta x_1)_d = \frac{(\Delta x_1)_c^2 \sigma^2(r) + (\Delta r)_c^2 \sigma^2(x_1)}{(\Delta x_1)_c \sigma^2(r)} \quad (\text{E14a})$$

and

$$(\Delta r)_d = \frac{(\Delta x_1)_c^2 \sigma^2(r) + (\Delta r)_c^2 \sigma^2(x_1)}{(\Delta r)_c \sigma^2(x_1)} \quad (\text{E14b})$$

The derivatives $\partial R / \partial x_1$ and $\partial R / \partial r$ use the approximations

$$\frac{\partial R}{\partial x_1} \simeq \frac{\Delta R}{(\Delta x_1)_d} \quad (\text{E15a})$$

and

$$\frac{\partial R}{\partial r} \simeq \frac{\Delta R}{(\Delta r)_d} \quad (\text{E15b})$$

These derivatives are then computed using equations (E15a) and (E15b) combined with (E14a) and (E14b): a particular value of $(\Delta x_1)_c$ is added to the $(x_1)_c$ of the point on the model curve that is closest to the data point. This implies a particular $(\Delta r)_c$, which, in turn, implies a particular ΔR . These are placed in equations (E14a) and (E14b) to compute the variations induced at the data point, $(\Delta x_1)_d$ and $(\Delta r)_d$. These, in turn, are used in equations (E15a) and (E15b) to compute the desired derivatives. In the special cases where $(\Delta x_1)_c = 0$ and $(\Delta r)_c = 0$, $\partial R / \partial x_1 = 0$ and $\partial R / \partial r = 0$, respectively, which can be verified geometrically and do *not* come from equations (E14a) and (E14b).

Generalizing the above to the two-component LVG model is trivial. The definitions of the $\{a_i\}$ are now the seven parameters of the two-component models, instead of the three parameters shown in equations (E4a), (E4b), and (E4c).

F. Uncertainty Analysis of the Dust-Derived Column Density for the Two-Component Models

As stated in Section 3.3, the column density of molecular gas derived from the continuum observations is derived from expression (40), which is written here as

$$Y = C(\{a_i\}; x_1, x_2, x_3) X(x_1, x_2) \quad , \quad (\text{F1})$$

where Y is the observed column density, $N_d(\text{H})$, C is the factor multiplying $N_d(\text{H})$, and X is $N_{d1}(\text{H})$. The $\{x_i\}$ are defined as Appendix E, except that x_2 is now T_{dc} . The $\{a_i\}$ are the seven parameters that specify each model curve for the two-component models (see Section 3.3). The function C is analogous to the R in Appendix E. Consequently, the uncertainty derivation is very similar to that in Appendix E. The only other expression needed is that for X . This can be in the Wien limit for simplicity, as was done in Section 2.1 and Appendix D. Specifically, equation (D1) is now written as

$$X(x_1, x_2) = x_2 \text{Exp}\left(\frac{F}{x_1}\right) \quad . \quad (\text{F2})$$

As in Appendix E, taking partial derivatives of Y with respect to the $\{a_i\}$ and $\{x_i\}$ is necessary. Consequently, we use the following:

$$\frac{\partial X}{\partial x_1} = X \left(\frac{-F}{x_1} \right) \quad (\text{F3a})$$

and

$$\frac{\partial X}{\partial x_2} = \frac{X}{x_2} \quad . \quad (\text{F3b})$$

Taking the partial derivatives of Y with respect to the $\{a_i\}$ and $\{x_i\}$ and adding them as in equation (E6) gives

$$\begin{aligned} \sigma^2(Y) = & \left[\sum_{i=1}^7 \left(\frac{\partial C}{\partial a_i} \right)^2 \sigma^2(a_i) \right] X^2 + \left[\left(\frac{\partial C}{\partial x_1} \right)^2 \sigma^2(x_1) + \left(\frac{\partial C}{\partial r} \right)^2 \sigma^2(r) \right] X^2 \\ & + 2 \left[-F \frac{\partial C}{\partial x_1} \frac{\sigma^2(x_1)}{x_1^2} + r \frac{\partial C}{\partial r} \frac{\sigma^2(x_2)}{x_2^2} \right] X^2 + C^2 \sigma^2(X) \quad , \end{aligned} \quad (\text{F4})$$

where r is defined as in Appendix E. The partial derivatives of C were determined using the same approach as for the partial derivatives of R in Appendix E. Expression (F4) was used to give the uncertainties in the derived $N_d(H)$ values for the two-component models.

REFERENCES

- Aalto, S., Booth, R. S., Black, J. H., and Johansson, L. E. B. 1995, *A&A*, 300, 369
- Aalto, S., Hüttemeister, Scoville, N. Z., Thaddeus, P. 1999, *ApJ*, 522, 165
- Andriesse, C. D. 1974, *A&A*, 37, 257
- Bally, J., Langer, W. D., Stark, A. A., and Wilson, R. W. 1987, *ApJ*, 312, L45
- Bally, J., Langer, W. D., and Liu, W. 1991, *ApJ*, 383, 645
- Berkhuijsen, E. M. 1972, *A&AS*, 5, 263
- Blaauw, A. 1964, *ARA&A*, 2, 213
- Black, J. H. and van Dishoeck, E. F. 1987, *ApJ*, 322, 412
- Boggess N. et al. 1992, *ApJ*, 397, 420
- Boreiko, R. T. and Betz, A. L. 1989, *ApJ*, 346, L97
- Boulanger, F., Bronfman, L., Dame, T. M., and Thaddeus, P. 1998, *A&A*, 332, 273
- Boulanger, F., Falgarone, E., Puget, J.-L., and Helou, G. 1990, *ApJ*, 369, 136
- Bronfman, L., Cohen, R. S., Alvarez, H., May, J., and Thaddeus, P. 1988, *ApJ*, 324, 248
- Brown, A. G. A., de Geus, E. J., de Zeeuw, P. T. 1994, *A&A*, 289, 101
- Brown, A. G. A., Hartmann, D., and Burton, W. B. 1995, *A&A*, 300, 903
- Bryant, P. M. and Scoville, N. Z. 1999, *AJ*, 117, 2632
- Burke, J. R. and Hollenbach, D. J. 1983, *ApJ*, 265, 223
- Chromey, F. R., Elmegreen, B. G., and Elmegreen, D. M. 1989, *AJ*, 98, 2203

- COBE* Diffuse Infrared Background Experiment (*DIRBE*) Explanatory Supplement 1998, version 2.3, ed. M. G. Hauser, T. Kelsall, D. Leisawitz, and J. Weiland, *COBE* Ref. Pub. 98-A (Greenbelt, MD: NASA/GSFC), available in electronic form from the NSSDC.
- Cohen, R. S., Dame, T. M., and Thaddeus, P. 1986, *ApJS*, 60, 695
- CRC Handbook of Chemistry and Physics 1998-99, ed. D. R. Lide, (Boca Raton: CRC Press)
- Dame, T. M., Hartmann, D., and Thaddeus, P. 2000, *ApJ*, 547, 792
- Dame, T. M. and Thaddeus, P. 1994, *ApJ*, 436, L173
- Dame, T. M., Ungerechts, H., Cohen, R. S., de Geus, E. J., Grenier, I. A., May, J., Murphy, D. C., Nyman, L.-Å., and Thaddeus, P. 1987, *ApJ*, 322, 706
- Désert, F.-X., Boulanger, F., & Puget, J. L. 1990, *A&A*, 237, 215
- Dickman, R. L. 1975, *ApJ*, 202, 50
- Dupac, X., Giard, M., Bernard, J.-P., Lamarre, J.-M., Mény, C., Pajot, F., Ristorcelli, I., Serra, G., and Torre, J.-P. 2000, *ApJ*, 553, 604
- Encrenaz, P. J., Falgarone, E., and Lucas, R. 1975, *A&A*, 44, 73
- Fixsen, D. J., Bennett, C. L., and Mather, J. C. 1999, *ApJ*, 526, 207
- Frerking, M. A., Langer, W. D., and Wilson, R. W. 1982, *ApJ*, 262, 590
- Fuente, A., Martín-Pintado, J., Rodríguez-Fernández, N. J., Rodríguez-Franco, A., de Vicente, P., and Kunze, D. 1999, *ApJ*, 518, L45
- García-Burillo, S., Martín, J., Fuente, A., and Neri, A. 2000, *A&A*, 355, 499
- Goldreich, P. & Kwan, P. 1974, *ApJ*, 189, 441
- Goldsmith, P. F., Bergin, E. A., and Lis, D. C. 1997, *ApJ*, 491, 615
- Grabelsky, D. A., Cohen, R. S., Bronfman, L., and Thaddeus, P. 1988, *ApJ*, 331, 181
- Graf, U. U., Eckart, A., Genzel, R., Harris, A. I., Poglitsch, A., Russell, A. P. G., and Stutzki, J. 1993, *ApJ*, 405, 249
- Graf, U. U., Genzel, R., Harris, A. I., Hills, R. E., Russell, A. P. G., and Stutzki, J. 1990, *ApJ*, 358, L49

- Green, D. A. 1991, MNRAS, 253, 350
- Güsten, R., Serabyn, E., Kasemann, C., Schinkel, A., Schneider, G., Schulz, A., and Young, K. 1993, ApJ, 402, 537
- Harris, A. I., Hills, R. E., Stutzki, J., Graf, U. U., Russell, A. P. G., and Genzel, R. 1991, ApJ, 382, L75
- Harris, A. I., Jaffe, D. T., Silber, M., and Genzel, R. 1985, ApJ, 294, L93
- Harrison, A., Henkel, C., and Russell, A. 1999, ApJ, 303, 157
- Haslam, C. G. T., Quigley, M. J. S., and Salter, C. J. 1970, MNRAS, 147, 405
- Hauser, M. G. et al. 1998, ApJ, 508, 25
- Heiles, C. and Habing, H. J. 1974, A&AS, 14, 1
- Heiles, C., Haffner, L. M., Reynolds, R. J., and Tufte, S. L. 2000, ApJ, 536, 335
- Heyer, M. H., Brunt, C., Snell, R. L., Howe, J., Schoerb, F. P., and Carpenter, J. M. 1998, ApJS, 115, 241
- Hollenbach, D. J. 1989, IAU Symp. 135, Interstellar Dust, eds. A. G. G. M. Tielens & L. Allamandola, (Dordrecht:Kluwer), p227
- Howe, J. E., Jaffe, D. T., Grossman, E. N., Wall, W. F., Mangum, J. G., and Stacey, G. J. 1993, ApJ, 410, 179
- Ikeda, M., Maezawa, H., Ito, T., Saito, G., Yutaro, S., Yamamoto, S., Tatematsu, K., Arikawa, Y., Aso, Y., Noguchi, T., Shi, S.-C., Miyazawa, K., Saito, S., Ozeki, H., Fujiwara, H., Ohishi, M., and Inatani, J. 1999, ApJ, 527, L59
- IRAS Catalogs and Atlases: Explanatory Supplement. 1988, ed. C. A. Beichman, G. Neugebauer, H. J. Habing, P. E. Clegg and T. J. Chester (Washington, DC:GPO)
- Johnstone, D. and Bally, J. 1999, ApJ, 510, L49
- Johnstone, D., Fich, M., Mitchell, G. F., Moriarty-Schieven, G. 2001, ApJ, 559, 307
- Kawamura, A., Onishi, T., Yonekura, Y., Dobashi, K., Mizuno, A., Ogawa, H., and Fukui, Y. 1998, ApJS, 117, 387
- Kennicutt, R. C. 1989, ApJ, 344, 685

- Kikumoto, T., Taniguchi, Y., Nakai, N., Ishizuki, S., Matsushita, S., and Kawabe, R. 1998, PASJ, 50, 309
- Knapp, G. R. and Jura, M. 1976, ApJ, 209, 782
- Kuno, N., Nakai, N., Handa, T., and Sofue, Y. 1995, PASJ, 47, 745
- Lada, E. A. 1992, ApJ, 393, L25
- Lagache, G., Abergel, A., Boulanger, F., and Puget, J.-L. 1998, A&A, 333, 709
- Lang, W. J., Mashedier, M. R. W., Dame, T. M., and Thaddeus, P. 2000, A&A, 357, 1001
- Langer, W. D. and Penzias, A. A. 1990, ApJ357, 477
- Lee, Y., Stark, A. A., Kim, H.-G., and Moon, D. 2001, ApJS, 136, 137
- Leisawitz, D. and Hauser, M. J. 1988, ApJ, 332, 954
- Lo, K. Y., Cheung, K. Y., Masson, C. R., Phillips, T. G., Scott, S. L., and Woody, D. P. 1987, ApJ, 312, 574
- Maddalena, R. J., Morris, M., Moscowitz, J., and Thaddeus, P. 1986, ApJ, 303, 375
- Martin, C. L. and Kennicutt R. C. 2001, ApJ, 555, 301
- Mitchell, G. F., Johnstone, D., Moriarty-Schieven, G., Fich, M., and N. F. H. Tothill 2001, ApJ, 556, 215
- Mizuno A., Hayakawa, T., Yamaguchi, N., Kato, S., Hara, A., Mizuno, N., Yonekura, Y., Onishi, T., Kawamura, A., Tachihara, K., Obayashi, A., Xiao, K., Ogawa, H., and Fukui, Y. 1998, ApJ, 507, L83
- Mochizuki, K. and Nakagawa, T. 2000, ApJ535, 118
- Moorwood, A. F. M. and Oliva, E. 1988, A&A, 203, 278
- Moorwood, A. F. M. and Oliva, E. 1990, A&A, 239, 78
- Mulchaey, J. S. and Regan, M. W. 1997, ApJ, 482, L135
- Murdin, P. and Penston, M. V. 1977, MNRAS, 181, 657
- Nagahama, T., Mizuno, A., Ogawa, H., and Fukui, Y. 1998, AJ, 116, 336
- Nishiyama, K. and Nakai, N. 2001, PASJ, 53, 713

- Nishiyama, K., Nakai, N., and Kuno, N. 2001, PASJ, 53, 757
- Oka, T., Hasegawa, T., Hayashi, M., Handa, T., and Sakamoto, S. 1998, ApJ, 493, 730
- Onishi, T., Mizuno, A., Kawamura, A., Ogawa, H., and Fukui, Y. 1996, ApJ, 465, 815
- Padoan, P., Juvela, M., Bally, J., and Nordlund, Å. 2000, ApJ, 529, 259
- Paglione, T. A. D., Jackson, J. M., and Ishizuki, S. 1997, ApJ, 484, 656
- Parmar, P. S., Lacy, J. H., and Achtermann, J. M. 1991, ApJ, 372, L25
- Plume, R., Bensch, F., Howe, J. E., Ashby, M. L. N., Bergin, E. A., Chin, G., Erickson, N. R., Goldsmith, P. F., Harwit, M., Kleiner, S., Koch, D. G., Neufeld, D. A., Patten, B. M., Scheider, R., Snell, R. L., Stauffer, J. R., Tolls, V., Wang, Z., Winnewisser, G., Zhang, Y. F., Reynolds, K., Joyce, R., Tavoletti, C., Jack, G., Rodkey, C. J., and Melnick, G. J. 2000, ApJ, L133
- Press, W. H., Teukolsky, S. A., Vetterling, W. T., and Flannery, B. P. 1992, Numerical Recipes, Second Edition, (Cambridge: Cambridge University Press)
- Puxley, P. J., Hawarden, T. G., and Mountain, C. M. 1990, ApJ, 364, 77
- Rand, R. J., Kulkarni, S. R., and Rice, W. 1992, ApJ, 390, 66
- Reach, W. T., Wall, W. F., and Odegard, N. 1998, ApJ, 507, 507
- Reich, W. 1978, A&A, 64, 407
- Rieu, N.-Q., Jackson, J. M., Henkel, C., Trurong-Bach, and Mauersberger, R. 1992, ApJ, 399, 521
- Robinson, B. J., Manchester, R. N., Whiteoak, J. B., Otrupcek, R. E., and McCutcheon, W. H. 1988, A&A, 193, 60
- Rodríguez-Fernández, N. J., Martín-Pintado, J., Fuente, A., de Vicente, P., Wilson, T. L., and Hüttemeister, S. 2001, A&A, 365, 174
- Rosenthal, D., Bertoldi, F., and Drapatz, S. 2000, A&A, 356, 705
- Rownd, B. K. and Young, J. S. 1999, AJ, 118, 670
- Sage, L. J., Mauersberger, R., Henkel, C. 1991, A&A, 249, 31
- Sakamoto, S., Handa, T., Sofue, Y., Honma, M., and Sorai, K. 1997, ApJ, 475, 134

- Sakamoto, S., Hasegawa, T., Hayashi, M., Handa, T., and Oka, T. 1995, *ApJS*, 100, 125
- Sakamoto, S., Hasegawa, T., Hayashi, M., Morino, J.-I., and Sato, K. 1997a, *ApJ*, 481, 302
- Sakamoto, S., Hayashi, M., Hasegawa, T., Handa, T., and Oka, T. 1994, *ApJ*, 425, 641
- Sanders, D. B., Scoville, N. Z., and Solomon, P. M. 1985, *ApJ*, 289, 373
- Sanders, D. B., Solomon, P. M., and Scoville, N. Z. 1984, *ApJ*, 276, 182
- Schloerb, F. P., Snell, R. L., and Schwartz, P. R. 1987, *ApJ*, 319, 426
- Scoville, N. Z. and Good, J. C. 1989, *ApJ*339, 149
- Scoville, N. Z., Soiffer, B. T., Neugebauer, G., Young, J. S., Matthews, K., Yerka, J. 1985, *ApJ*, 289, 129
- Seaquist, E. R., Frayer, D. T., and Bell, M. B. 1998, *ApJ*, 507, 745
- Seki, J. & Yamamoto, T. 1980, *Ap&SS*, 72, 79
- Sellgren, K., Luan, L., and Werner, M. W. 1990, *ApJ*, 359, 384
- Sheth, K., Regan, M. W., Vogel, S. N., and Teuben, P. J. 2000, *ApJ*, 532, 221
- Silverberg, R. F. et al. 1993, in *Proc SPIE Conf. 2019, Infrared Spaceborne Remote*, ed. M. S. Scholl (Bellingham:SPIE), 180
- Sodroski, T. J., Bennett, C., Boggess, N., Dwek, E., Franz, B. A., Hauser, M. G., Kelsall, T., Moseley, S. H., Odegard, N., Silverberg, R. F., and Weiland, J. L. 1994, *ApJ*, 428, 638
- Sodroski, T. J., Dwek, E., Hauser, M. G., and Kerr, F. J. 1989, *ApJ*, 336, 762
- Sorai, K., Nakai, N., Kuno, N., Nishiyama, K., Hasegawa, T. 2000, *PASJ*, 52, 785
- Störzer, H., Zielinsky, M., Stutzki, J. and Sternberg, A. 2000, *A&A*, 358, 682
- Swartz, P. R., Snell, R. L., and Schloerb, F. P. 1989, *ApJ*, 336, 519
- Takami, M., Usuda, T., Sugai, H., Kawabata, H. Suto, H., and Tanaka, M. 2000, *ApJ*, 529, 268
- Tachihara, K., Mizuno, A., and Fukui, Y. 2000, *ApJ*, 528, 817
- Taylor, D. R. and Dickman, R. L. 1989, *ApJ*, 341, 293

- Thronson, H. A., Walker, C. K., Walker, C. E., and Maloney, P. 1989, *A&A*, 214, 29
- Tielens, A. G. G. M. and Hollenbach, D. 1985, *ApJ*, 291, 722
- Tilanus, R. P. J., Tacconi, L. J., Zhou, S., Sanders, D. B., Sutton, E. C., Lo, K. Y., Stephens, S. A., and Wynn-Williams, C. G. 1991, *ApJ*, 376, 500
- Tosaki, T., Hasegawa, T., Shioya, Y., Kuno, N., and Matsushita, S. 2002, *PASJ*, 54, 209
- Turner, J. L., Martin, R. N., Ho, P. T. P. 1991, *ApJ*, 367, 677
- Verter, F. 1987, *ApJS*, 65, 555
- Verter, F. 1988, *ApJS*, 68, 129
- Verter, F. and Rickard, L. J. 1989, *A&A*, 225, 27
- Vogel, S. N., Kulkarni, S. R., and Scoville, N. Z. 1988, *Nature*, 334, 402
- Wall, W. F. 1999, *Millimeter-Wave Astronomy: Molecular Chemistry and Physics in Space*, W. F. Wall, A. Carramiñana, L. Carrasco, and P. F. Goldsmith, Dordrecht: Kluwer, 1999, 1
- Wall, W. F., Jaffe, D. T., Bash, F. N., Israel, F. P., Maloney, P. R., and Baas, F. 1993, *ApJ*, 414, 98
- Wall, W. F., Jaffe, D. T., Israel, F. P., and Bash, F. N. 1991, *ApJ*, 380, 384
- Wall, W. F., Reach, W. T., Hauser, M. G., Arendt, R. G., Weiland, J. L., Berriman, G. B., Bennett, C. L., Dwek, E., Leisawitz, D., Mitra, P. M., Odenwald, S. F., Sodroski, T. J., and Toller, G. N. 1996, *ApJ*, 456, 566 (W96)
- Wall, W. F. 2006, *astro-ph* (Paper II)
- Wall, W. F. 2006a, *astro-ph* (Paper III)
- Wall, W. F. 2006b, *astro-ph*, in preparation
- Warren, W. H. and Hesser, J. E. 1977, *ApJS*, 34, 115
- Warren, W. H. and Hesser, J. E. 1978, *ApJS*, 36, 497
- Weingartner, J. C. and Draine, B. T. 2001, *ApJS*, 134, 263
- Werner, M. W., Gatley, I., Harper, D. A., Becklin, E. E., Loewenstein, R. F., Telesco, C. M., and Thronson, H. A. 1976, *ApJ*, 204, 420

- Wild, W., Harris, A. I., Eckart, A., Genzel, R., Graf, U. U., Jackson, J. M., Russell, A. P. G., and Stutzki, J. 1992, *A&A*, 265, 447
- Wilson, B. A., Dame, T. M., Mashedier, M. R. W., and Thaddeus, P. 2005, *A&A*, 430, 523
- Wilson, T. L., Muders, D., Kramer, C., and Henkel, C. 2001, *ApJ*, 557, 240
- Wong, T. and Blitz, L. 2000, *ApJ*, 540, 771
- Wright, C. M., van Dishoeck, E. F., Cox, P., Sidher, S. D., and Kessler, M. F. 1999, *ApJ*, 515, L29
- Zhang, C. Y., Laureijs, R. J., Chlewicki, G., Clark, F. O., and Wesselius, P. R. 1989, *A&A*, 218, 231
- Zhang, C. Y. and Green, D. A. 1991, *AJ*, 101, 1006

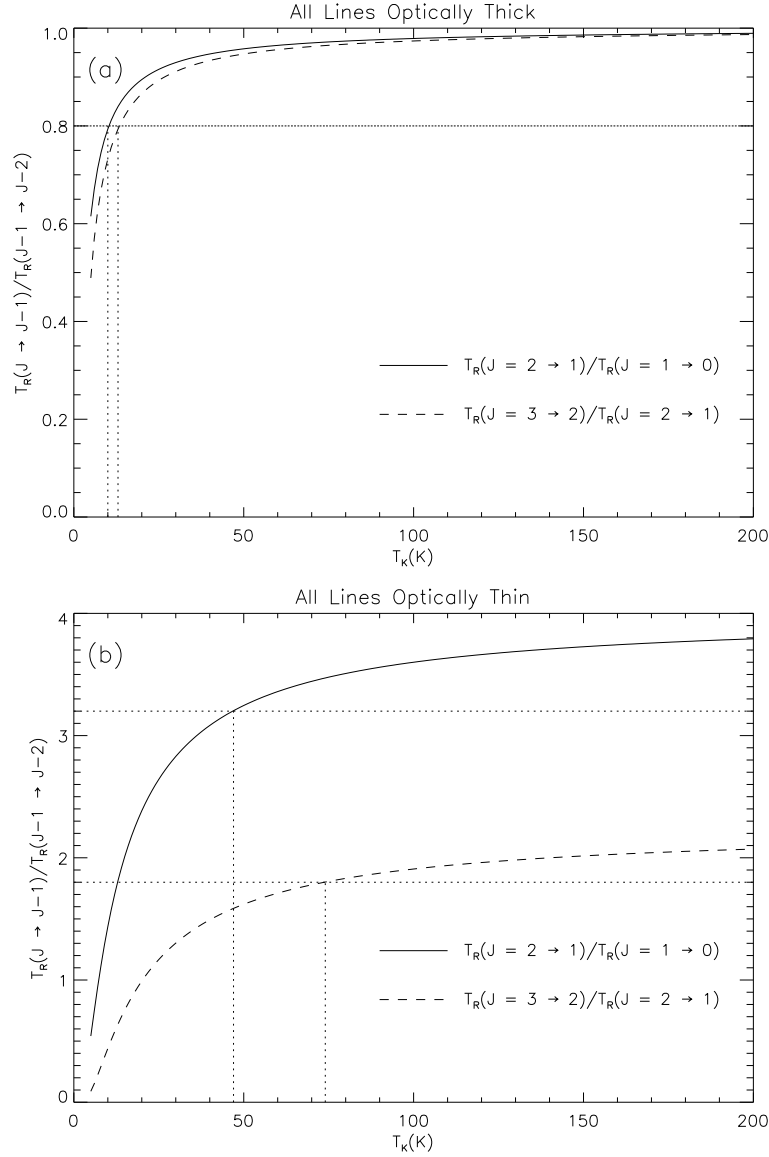


Fig. 1.— The panels above show CO rotational line ratios as a function of kinetic temperature, T_K , in the LTE limit. The solid curves show the ratio of the radiation temperature, T_R , of the $J = 2 \rightarrow 1$ line to that of the $J = 1 \rightarrow 0$ line. The dashed curves show the $T_R(J = 3 \rightarrow 2)/T_R(J = 2 \rightarrow 1)$ ratio. The horizontal dotted lines mark the levels of the ratios at 80% of their asymptotic values in the high- T_K limit. The vertical dotted lines mark the T_K values for which the ratios achieve this 80% level. Panel (a) shows the behavior of these ratios in the case where all the lines are optically thick. Panel (b) shows this behavior in the optically thin case.

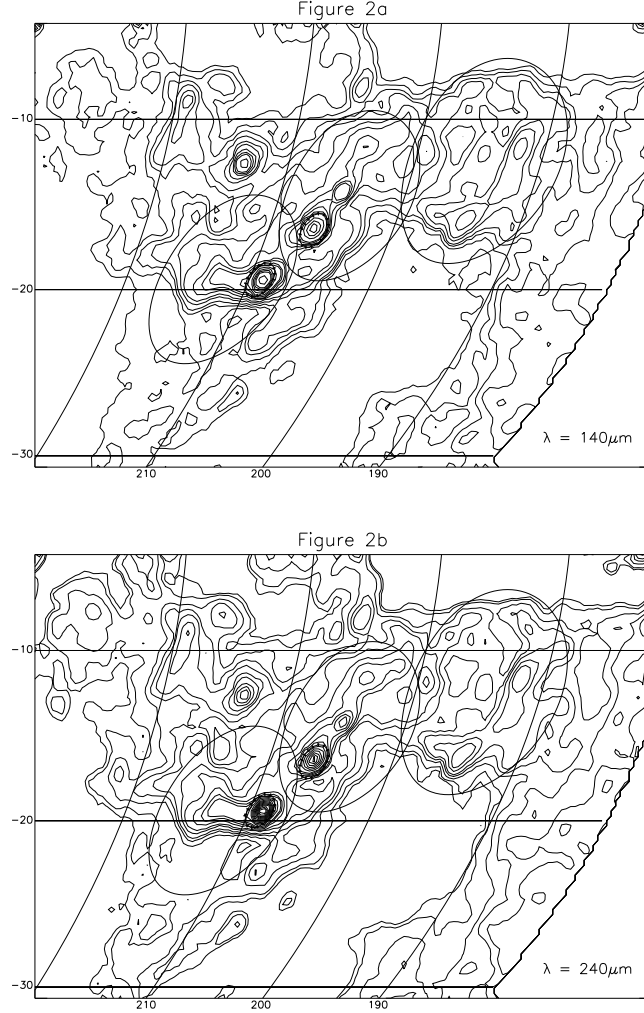


Fig. 2.— The *DIRBE* Surface Brightness Maps for $\lambda = 140$ and $240 \mu\text{m}$ from the 1998-release are displayed in the equal-area Mollweide projection with a Galactic longitude-latitude coordinate grid. The analysis concentrates on the three 10° - 12° circular fields that appear in the map as roughly elliptical loops; circles on the sky appear distorted in this projection. The fields, from east to west, are the Orion A, Orion B, and λ Orionis Fields. Also shown with dotted ellipses are the smaller (2° diameter) Orion Nebula and NGC 2024 Fields (which are circular on the real sky). The absolute photometric uncertainties of the maps are 10.6% for the $140 \mu\text{m}$ map and 11.6% for the $240 \mu\text{m}$ map. All maps have been “cleaned” of zodiacal light and had $\text{cosecant}(|b|)$ backgrounds subtracted. The contour levels for the $140 \mu\text{m}$ map are 5, 10, 15, 20, 30, 40, 60, 80, 100, 150, 200, 400, 600, 800, 1000, 1500, 1900 $\text{MJy} \cdot \text{sr}^{-1}$ and for the $240 \mu\text{m}$ map are 3, 5, 10, 15, 20, 30, 40, 60, 80, 100, 150, 200, 250, 300, 350, 400, 450, 500, 550, 600, 650, 700, 750 $\text{MJy} \cdot \text{sr}^{-1}$.

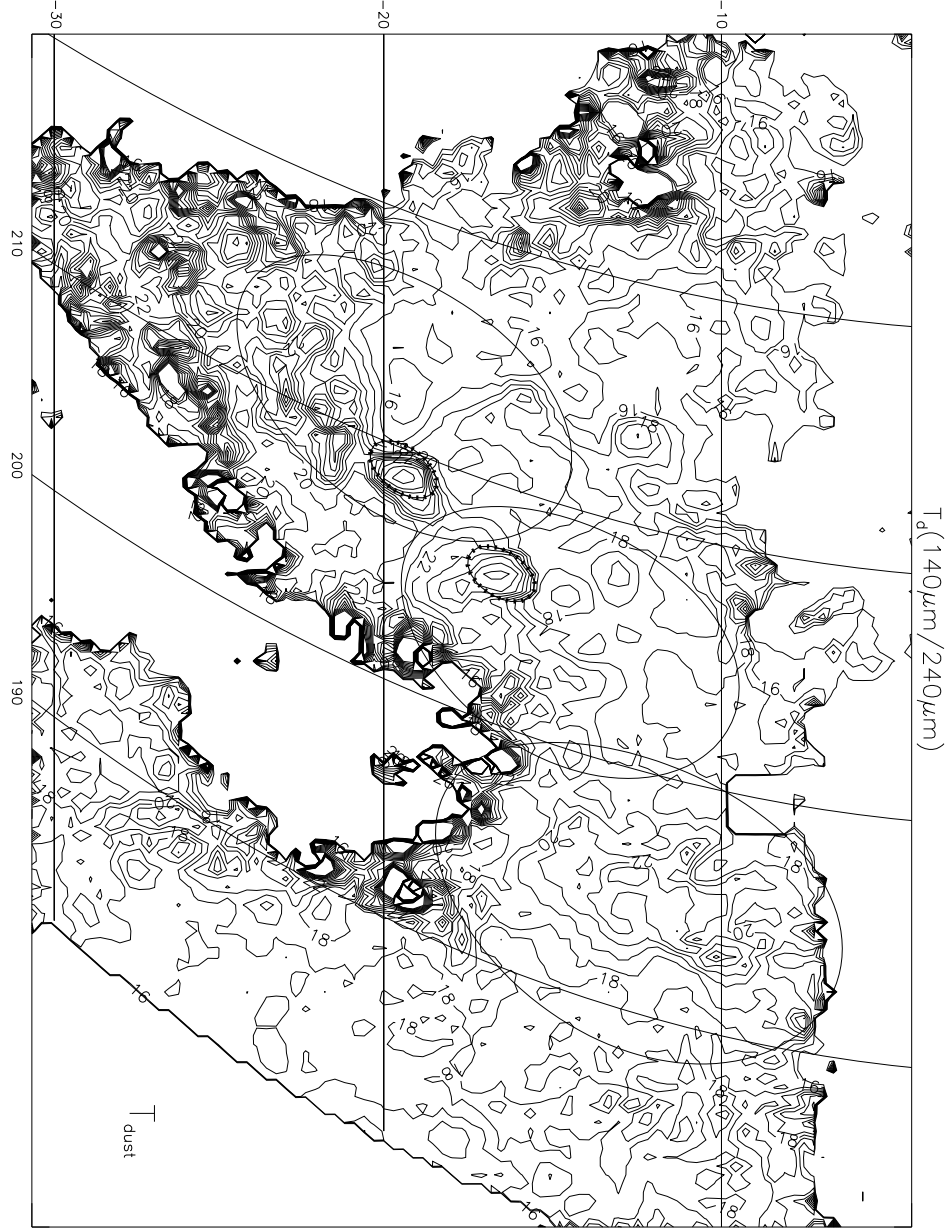


Fig. 3.— Spatial distribution of the $140\,\mu\text{m}/240\,\mu\text{m}$ color temperature, T_d , is illustrated ($\beta = 2$ emissivity index unless otherwise stated). Contour levels are 15, 16, 17, ..., 30 K. All positions in the T_d map where $I_\nu(140\,\mu\text{m}) < 1\,\text{MJy} \cdot \text{sr}^{-1}$ or $I_\nu(240\,\mu\text{m}) < 1\,\text{MJy} \cdot \text{sr}^{-1}$ were set to zero, resulting in the close spacing of contours at the edges of the emitting regions.

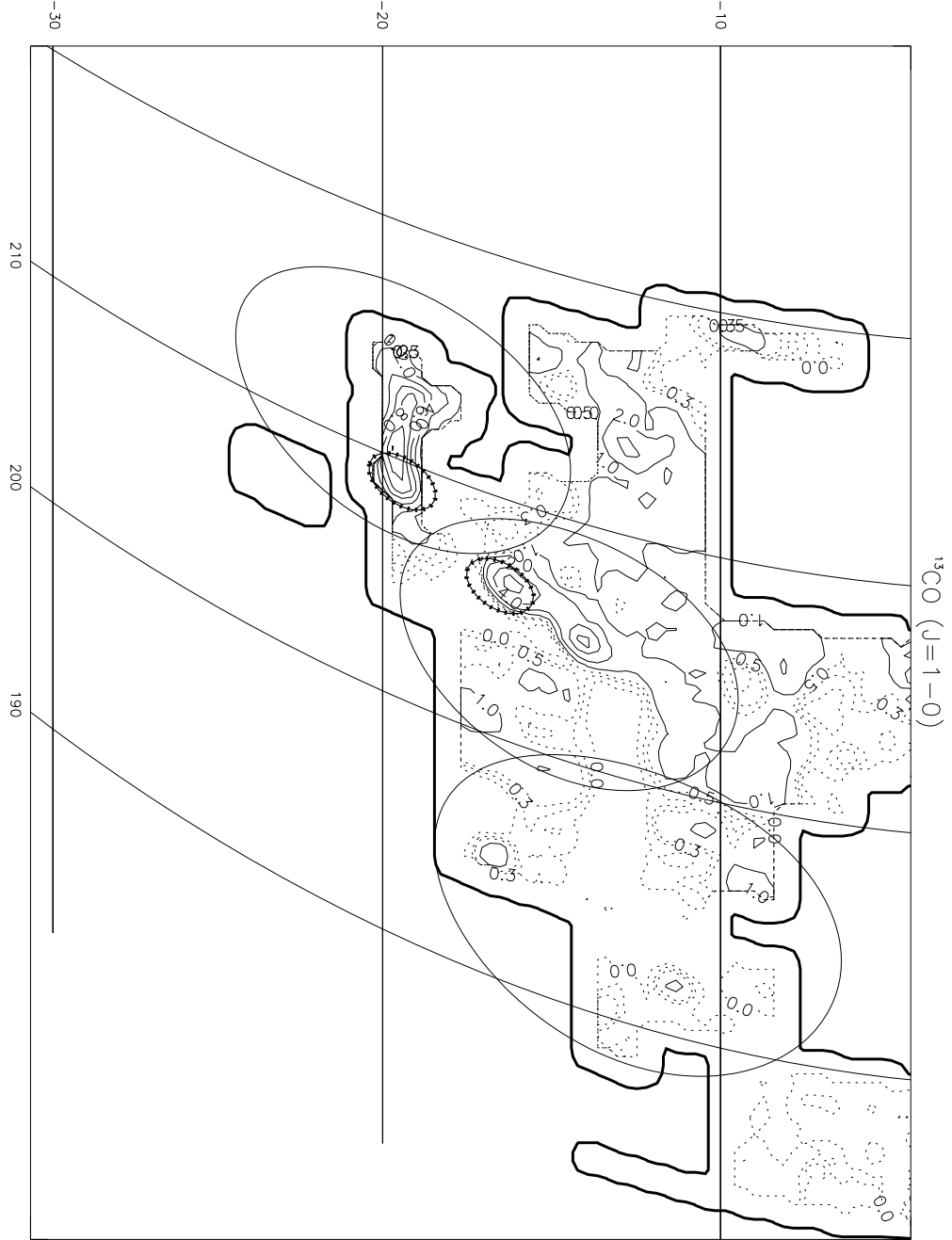


Fig. 4.— Map of the velocity-integrated radiation temperature of the $^{13}\text{CO } J = 1 \rightarrow 0$ line is shown for the Orion region. Contour levels are 0, 0.3, 0.5, 1, 2, 4, 6,...,12 $\text{K} \cdot \text{km} \cdot \text{s}^{-1}$. The thick contour indicates the edge of the mapped area.

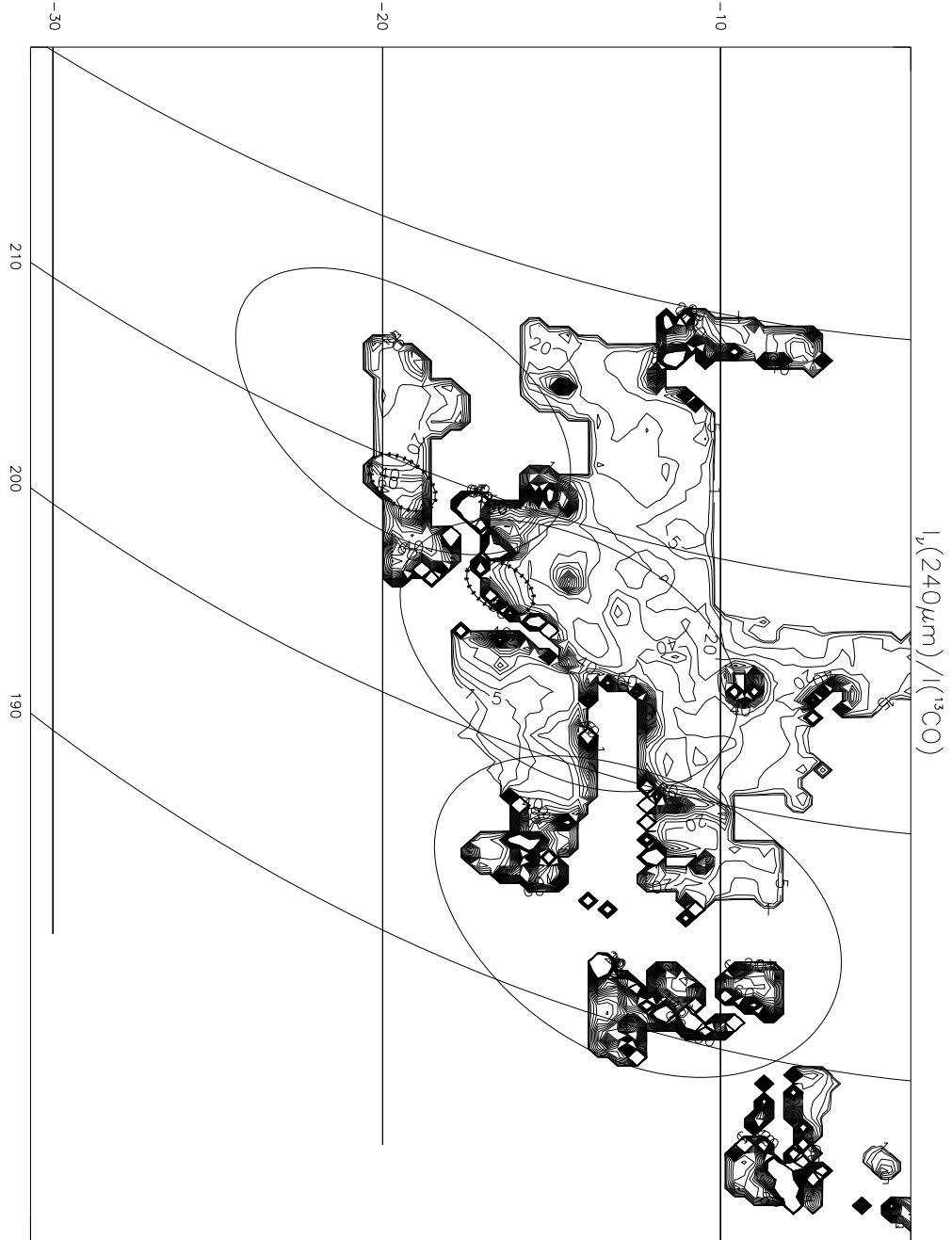


Fig. 5.— The map of r_{240} or $I_{\nu}(240 \mu\text{m})/I(^{13}\text{CO})$ is shown for the Orion region. Contour levels are 1, 2, 5, 10, 20, 30,..., 250 $\text{MJy} \cdot \text{sr}^{-1} \cdot (\text{K} \cdot \text{km} \cdot \text{s}^{-1})^{-1}$.

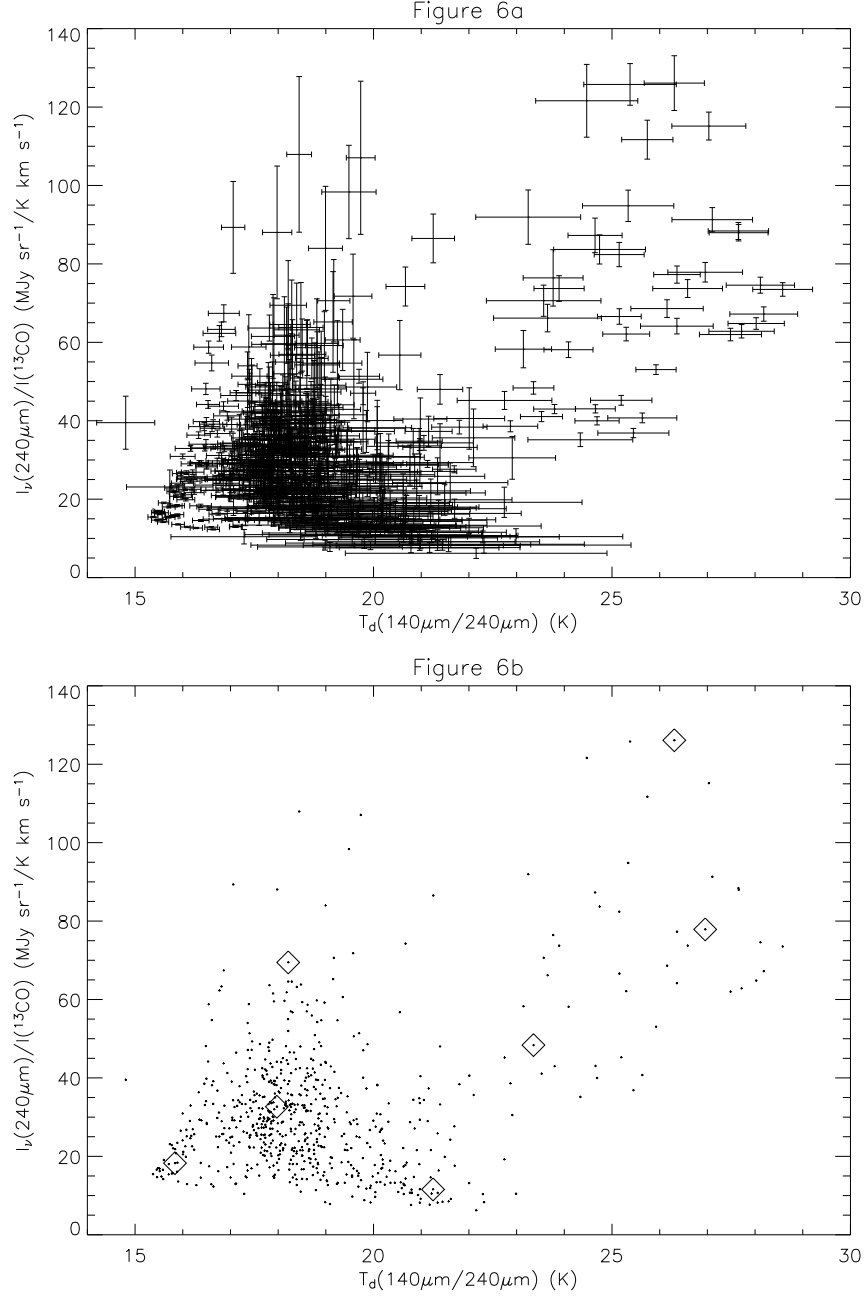


Fig. 6.— Plots of r_{240} or $I_\nu(240\mu\text{m})/I(^{13}\text{CO})$ versus T_d are shown for the Orion region. The plots include points at more than $5\text{-}\sigma$ in $I_\nu(140\mu\text{m})$, $I_\nu(240\mu\text{m})$, and $I(^{13}\text{CO})$. Panel a) includes the error bars of the random errors (i.e. systematic errors are not included), whereas in Panel b) the error bars are excluded to more clearly reveal the overall pattern in the plotted points. The diamonds in this panel are the fiducial points discussed in Section 3.5 and listed in Table 3.

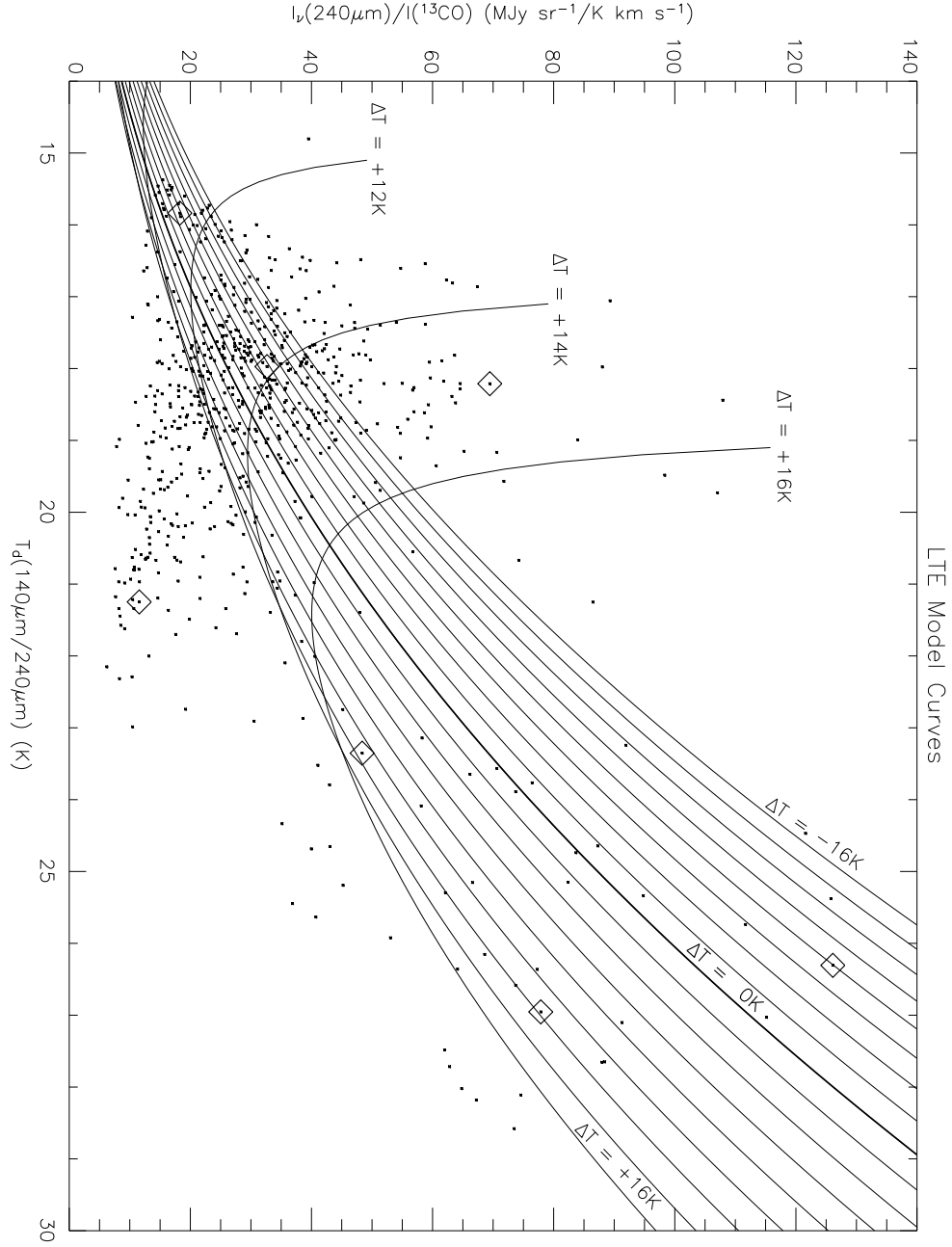


Fig. 7.— The model curves of r_{240} versus T_d are shown for the LTE case. The plot includes the same data points as in Figure 6 with error bars excluded for clarity. Each model curve is for a specific value of ΔT or $T_K - T_d$. The curves shown range from $\Delta T = -16\text{ K}$ to $+16\text{ K}$ in steps of 2 K . The diamonds in this figure are the fiducial points discussed in Section 3.5 and listed in Table 3.

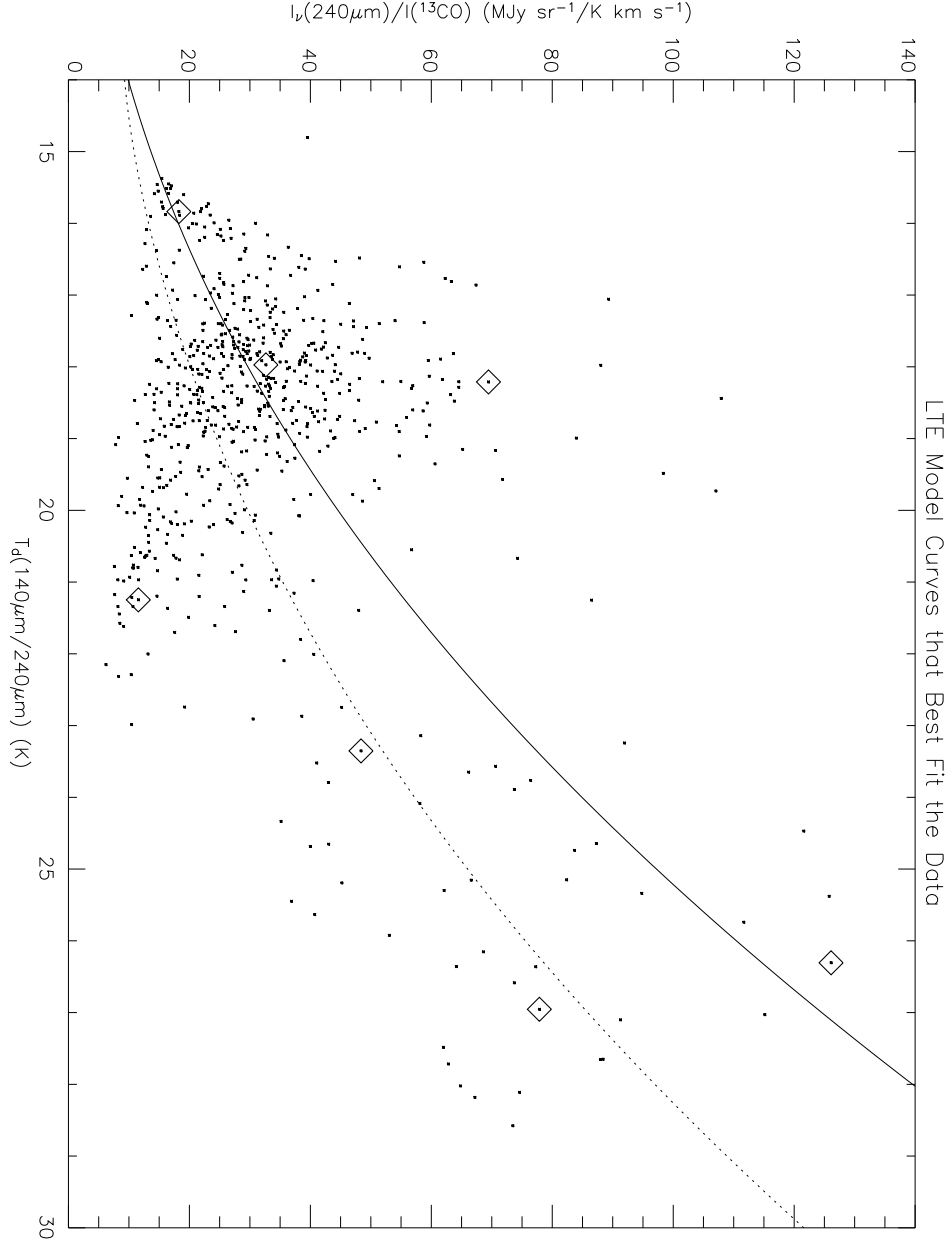


Fig. 8.— The model curves of r_{240} versus T_d that best fit the data are shown for the LTE case. The plot includes the same data points as in Figure 6 with error bars excluded for clarity. The solid curve represents $\Delta T = -4 \text{ K}$ and is the best fit to all the data points. The dotted curve represents $\Delta T = +9 \text{ K}$ and is the best fit to only the data points with $T_d > 20 \text{ K}$. The diamonds in this figure are the fiducial points discussed in Section 3.5 and listed in Table 3.

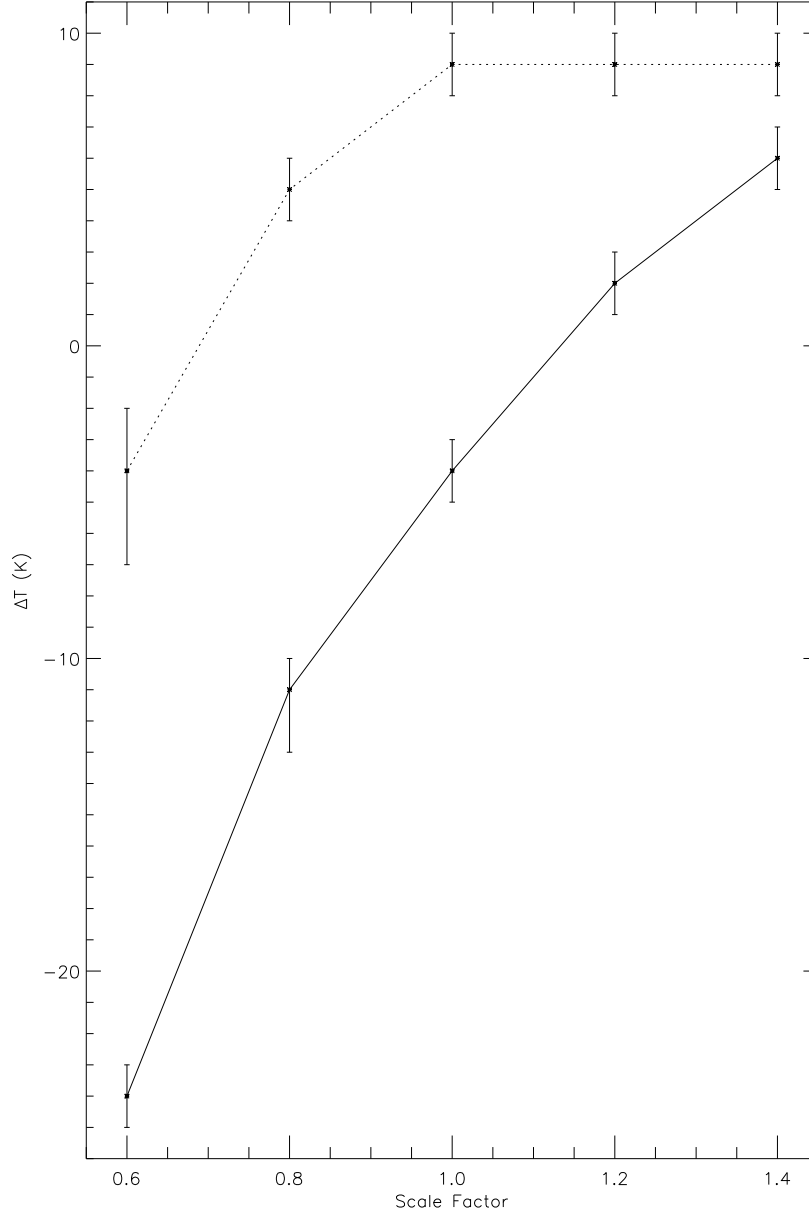


Fig. 9.— The effect of the systematic uncertainties on the resultant ΔT from the fits of the LTE model curves is shown. The effect of these uncertainties was tested by applying the scale factors 0.6, 0.8, 1.0, 1.2, and 1.4 to the model curves and fitting the ΔT for each one. The solid line represents the resultant ΔT values for the fits to all the data (i.e., all the data points shown in Figure 6). The dotted line represents the resultant ΔT values for the fits to the data with $T_d > 20$ K. The error bars represent the formal error bars for each model fit.

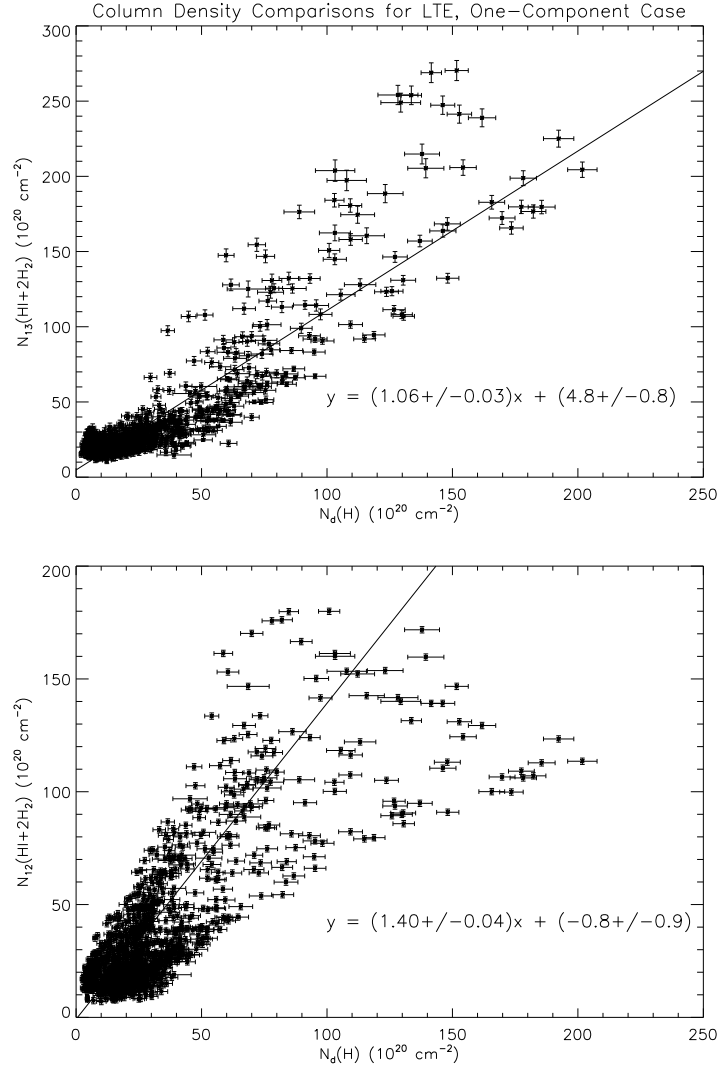


Fig. 10.— The plots above compare the gas column densities as derived from gas tracers and those derived from dust continuum emission for the case of LTE gas emission and a single component. The upper panel shows the gas column density as derived from the $^{13}\text{CO } J = 1 \rightarrow 0$ in the LTE, optically thin case versus the gas column density as derived from the $140 \mu\text{m}$ and $240 \mu\text{m}$ continuum emission. The points in the upper panel plot represent the positions where $I_\nu(140 \mu\text{m})$, $I_\nu(240 \mu\text{m})$, and $I(^{13}\text{CO})$ are at more than $5\text{-}\sigma$, as in Figure 6. The lower panel shows the gas column density as derived from the $^{12}\text{CO } J = 1 \rightarrow 0$ line assuming the conversion factor discussed in the text. The points in the lower panel plot represent the positions where $I_\nu(140 \mu\text{m})$, $I_\nu(240 \mu\text{m})$, and $I(^{12}\text{CO})$ are at more than $5\text{-}\sigma$. Consequently, this sample has more points than in the upper panel: specifically the upper panel has 674 points and the lower panel has 1053 points.

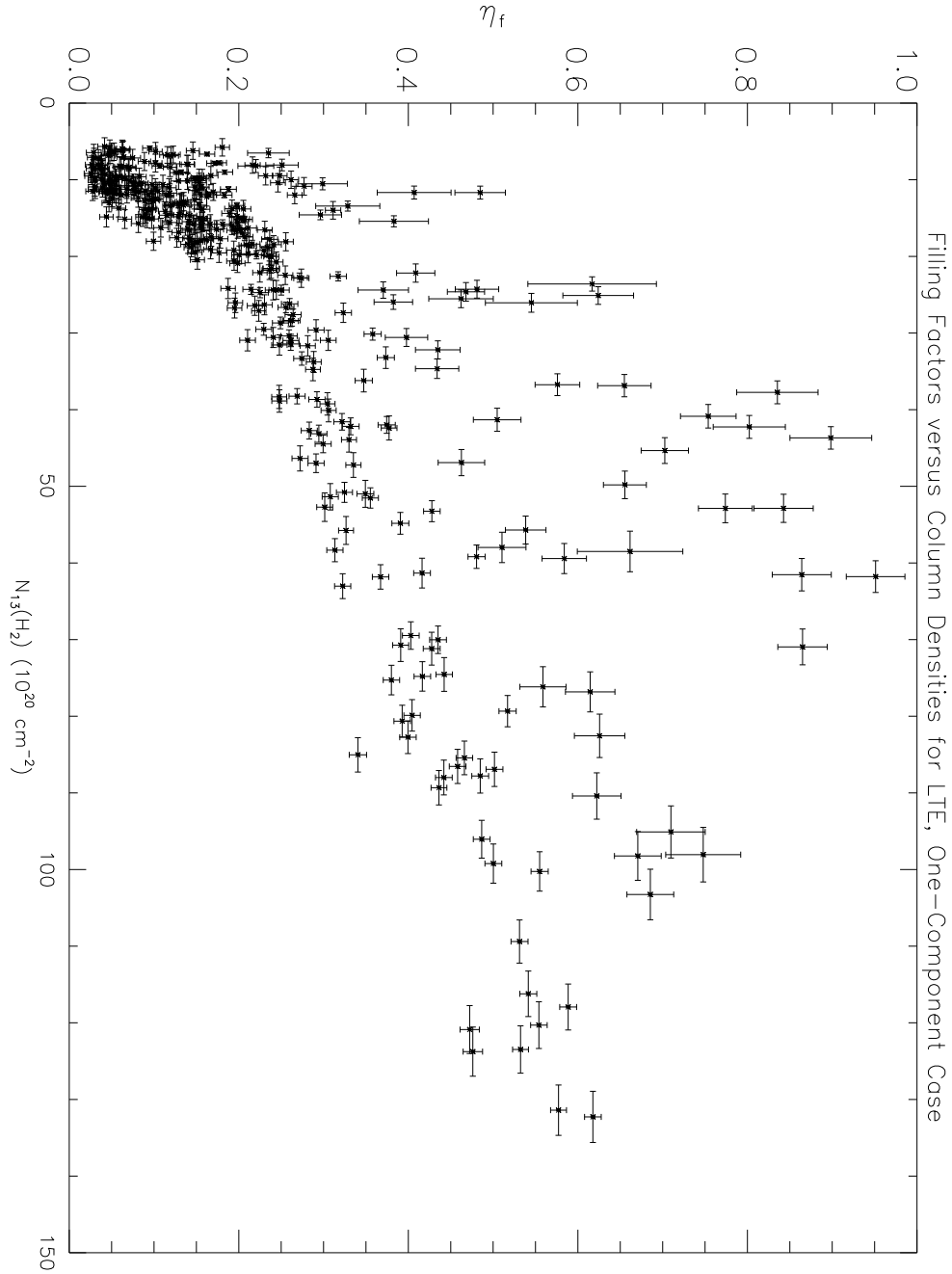


Fig. 11.— The area filling factors of substructures in the Orion clouds are plotted against the molecular gas column densities in the LTE, one-component case. The points in this plot represent the positions where $I_\nu(140 \mu\text{m})$, $I_\nu(240 \mu\text{m})$, and $I(^{13}\text{CO})$ are at more than $5\text{-}\sigma$ and where the peak radiation temperature of $^{12}\text{CO } J = 1 \rightarrow 0$ is at more than $3\text{-}\sigma$. This is a total of 372 points.

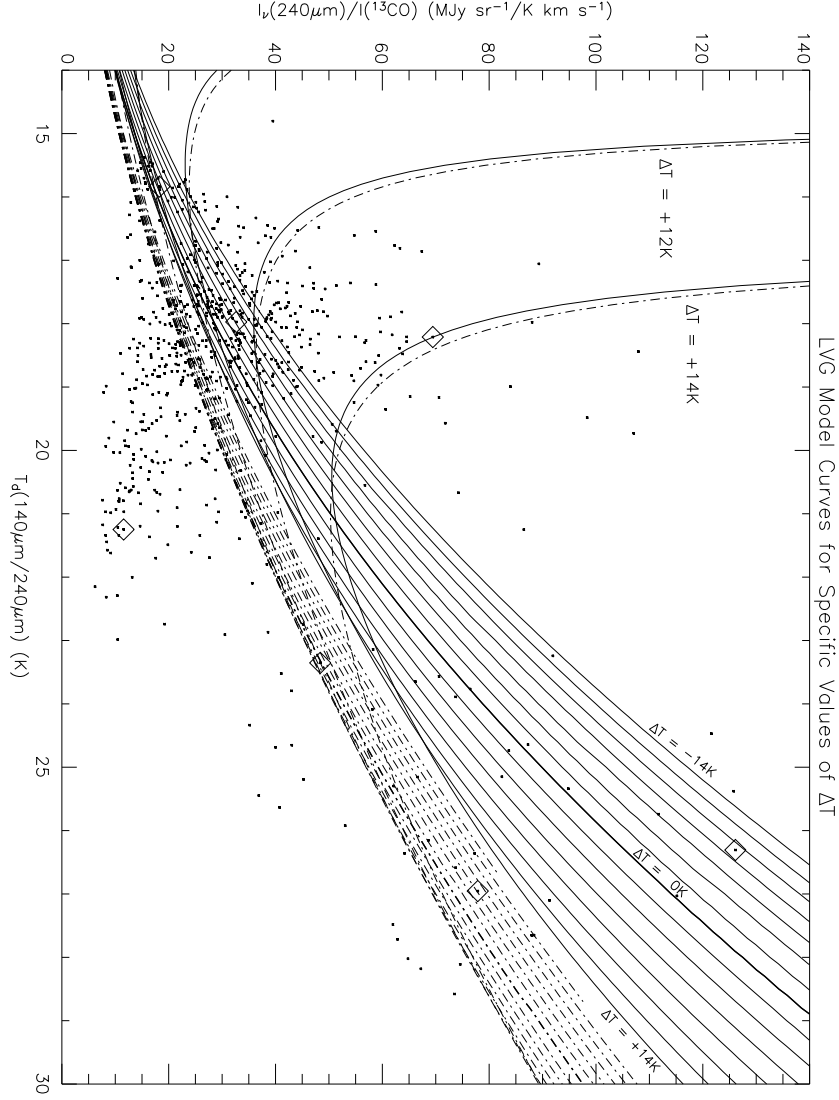


Fig. 12.— The model curves r_{240} versus T_d for different ΔT values are shown for the non-LTE, one-component case. For the solid curves, the $N(^{13}\text{CO})/\Delta v$ value is fixed at $3.2 \times 10^{15} \text{ cm}^{-2} \cdot (\text{km} \cdot \text{s}^{-1})^{-1}$ and the $n(\text{H}_2)$ value is fixed at $1 \times 10^5 \text{ cm}^{-3}$ — the best fit $N(^{13}\text{CO})/\Delta v$ and $n(\text{H}_2)$ values for model fits to all the points in the plot. For the dashed-dotted curves, the $N(^{13}\text{CO})/\Delta v$ value is fixed at $3.2 \times 10^{15} \text{ cm}^{-2} \cdot (\text{km} \cdot \text{s}^{-1})^{-1}$ and the $n(\text{H}_2)$ value is fixed at $5.6 \times 10^3 \text{ cm}^{-3}$ — the best fit $N(^{13}\text{CO})/\Delta v$ and $n(\text{H}_2)$ values for model fits to only the points with $T_d > 20 \text{ K}$. The curves (solid and dashed-dotted) shown range from $\Delta T = -14 \text{ K}$ to $+14 \text{ K}$ in steps of 2 K . The plot includes the same data points as in Figure 6 with error bars excluded for clarity. The diamonds in this figure are the fiducial points discussed in Section 3.5 and listed in Table 3.

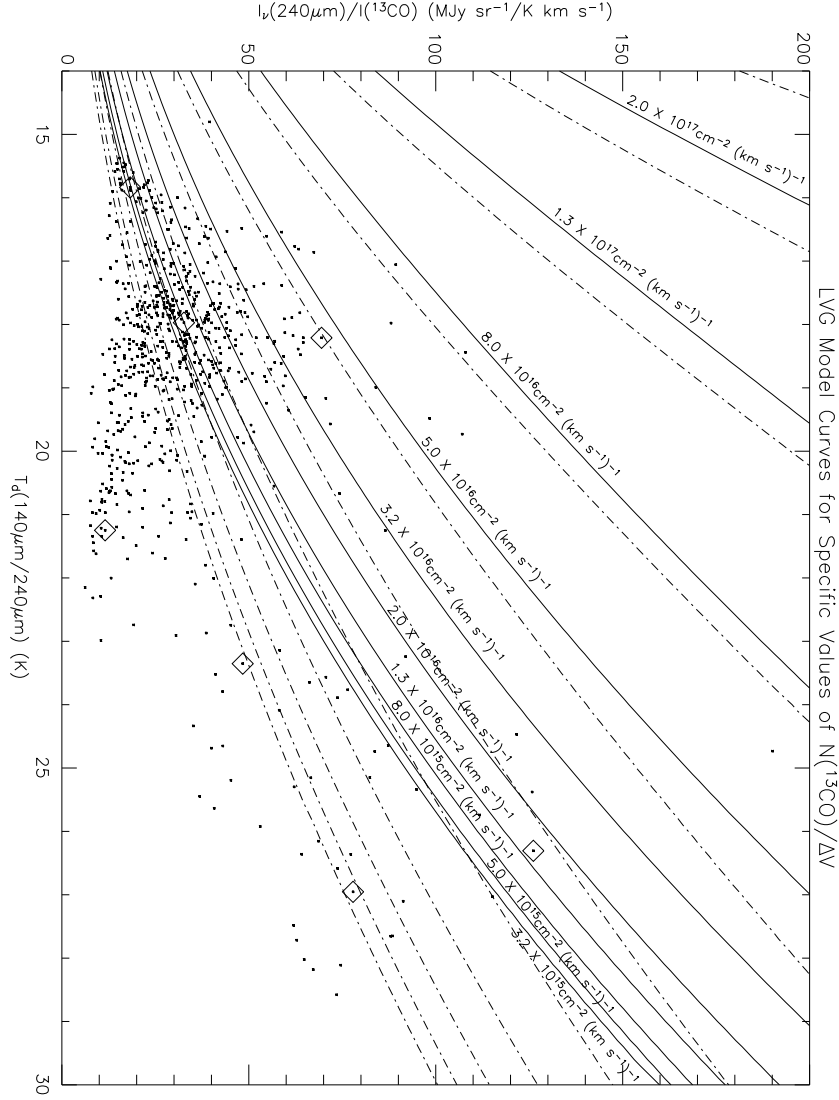


Fig. 13.— The model curves r_{240} versus T_d for different $N(^{13}\text{CO})/\Delta v$ values are shown for the non-LTE, one-component case. For the solid curves, the ΔT value is fixed at -1 K and the $n(\text{H}_2)$ value is fixed at $1 \times 10^5 \text{ cm}^{-3}$ — the best fit ΔT and $n(\text{H}_2)$ values for model fits to all the points in the plot. For the dashed-dotted curves, the ΔT value is fixed at -3 K and the $n(\text{H}_2)$ value is fixed at $5.6 \times 10^3 \text{ cm}^{-3}$ — the best fit ΔT and $n(\text{H}_2)$ values for model fits to only the points with $T_d > 20$ K. The solid curves are labelled with their corresponding values of $N(^{13}\text{CO})/\Delta v$. The $N(^{13}\text{CO})/\Delta v$ values for the dashed-dotted curves follow the same order as for the solid curves, i.e., from lower right to upper left. The plot includes the same data points as in Figure 6 with error bars excluded for clarity. The diamonds in this figure are the fiducial points discussed in Section 3.5 and listed in Table 3.

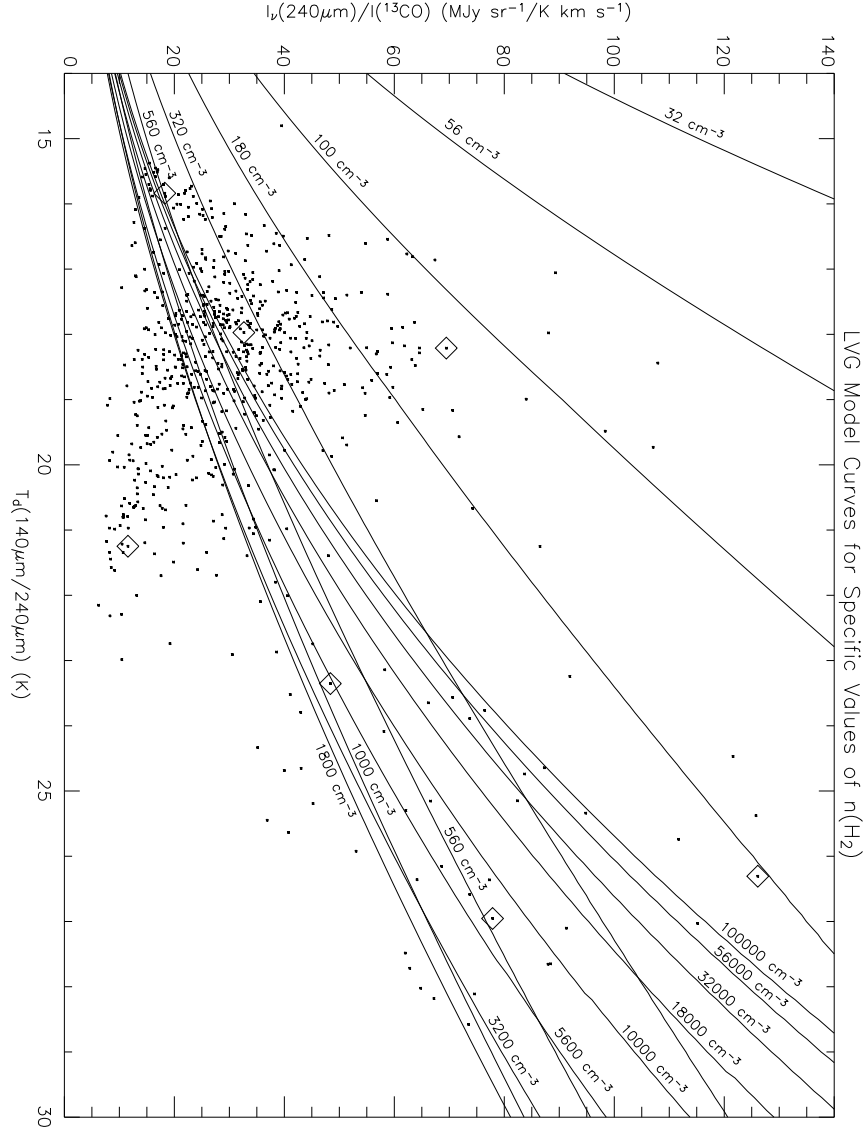


Fig. 14.— The model curves r_{240} versus T_d for different $n(\text{H}_2)$ values are shown for the non-LTE, one-component case. For the curves shown, the ΔT value is fixed at -1 K and the $N(^{13}\text{CO})/\Delta v$ value is fixed at $3.2 \times 10^{15} \text{ cm}^{-2} \cdot (\text{km} \cdot \text{s}^{-1})^{-1}$ — the best fit ΔT and $N(^{13}\text{CO})/\Delta v$ values for model fits to all the points in the plot. The best fit ΔT and $N(^{13}\text{CO})/\Delta v$ values for model fits to the points with $T_d > 20\text{ K}$ are similar or identical to those for all the points; consequently, those curves would be virtually identical to the solid curves above and are not shown. The plot includes the same data points as in Figure 6 with error bars excluded for clarity. The diamonds in this figure are the fiducial points discussed in Section 3.5 and listed in Table 3.

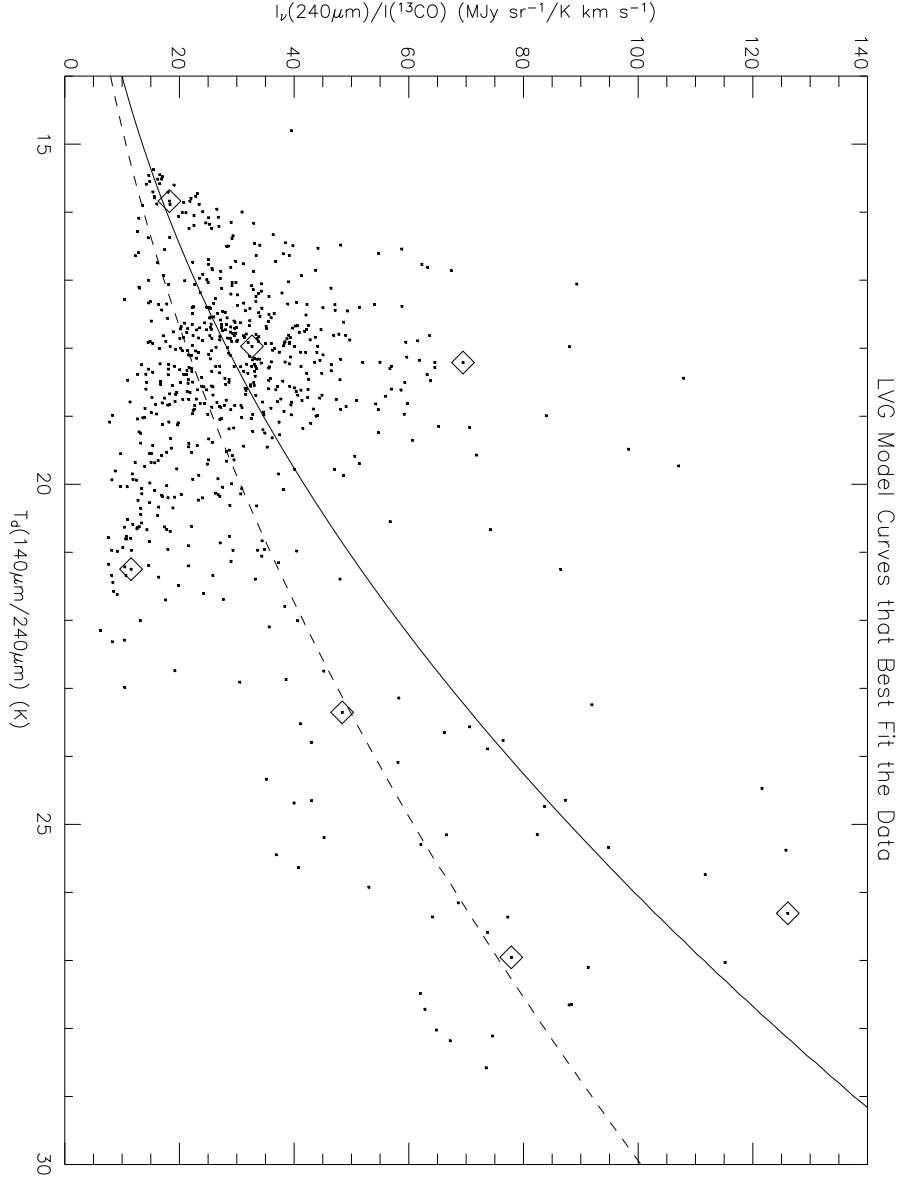


Fig. 15.— The model curves of r_{240} versus T_d that best fit the data are shown for the non-LTE, one-component case. The plot includes the same data points as in Figure 6 with error bars excluded for clarity. The solid curve represents $\Delta T = -1$ K, $N(^{13}\text{CO})/\Delta v = 3.2 \times 10^{15} \text{ cm}^{-2} \cdot (\text{km} \cdot \text{s}^{-1})^{-1}$, and $n(\text{H}_2) = 1 \times 10^5 \text{ cm}^{-3}$ and is the best fit to all the data points. The dotted curve represents $\Delta T = -3$ K, $N(^{13}\text{CO})/\Delta v = 3.2 \times 10^{15} \text{ cm}^{-2} \cdot (\text{km} \cdot \text{s}^{-1})^{-1}$, and $n(\text{H}_2) = 5.6 \times 10^3 \text{ cm}^{-3}$ and is the best fit to only the data points with $T_d > 20$ K. The diamonds in this figure are the fiducial points discussed in Section 3.5 and listed in Table 3.

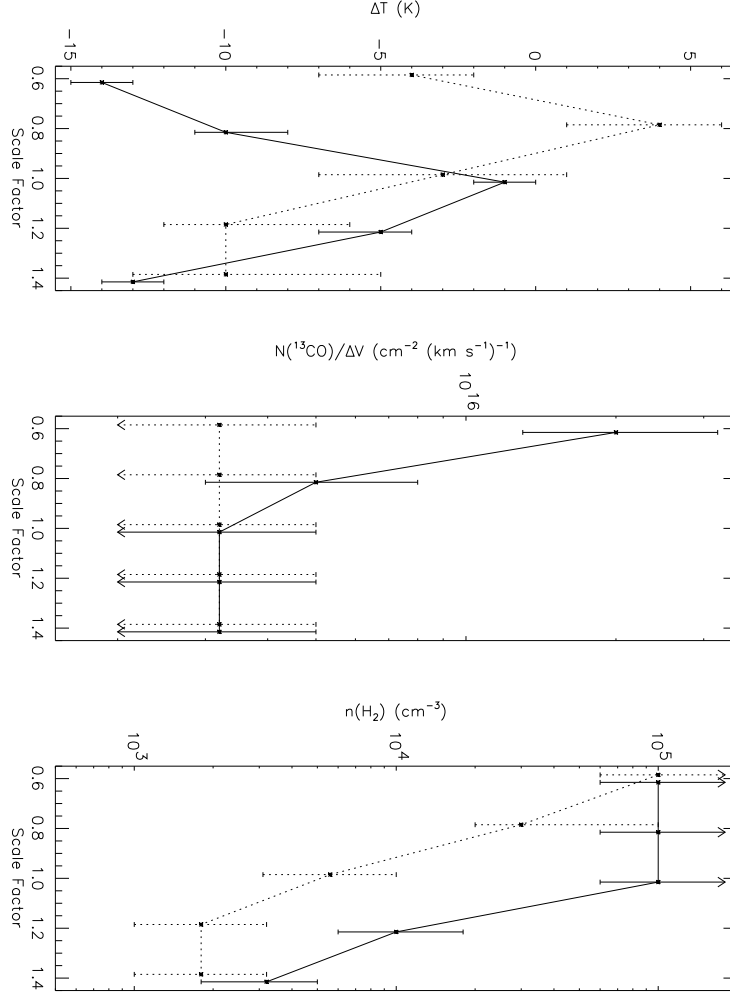


Fig. 16.— The effect of the systematic uncertainties on the resultant parameters from the fits of the LVG model curves is shown. The effect of these uncertainties was tested by applying the scale factors 0.6, 0.8, 1.0, 1.2, and 1.4 to the model curves and fitting the parameters for each scale factor. The left panel shows the resultant ΔT values, the center panel shows the resultant $N(^{13}\text{CO})/\Delta v$ values, and the right panel shows the $n(\text{H}_2)$ values. The solid line in each panel represents the resultant parameter values for the fits to all the data (i.e., all the data points shown in Figure 6). The dotted line represents the resultant parameter values for the fits to the data with $T_d \geq 20$ K. Notice that the plotted points have been slightly displaced horizontally from their true scale factor values for clarity. The error bars represent the formal error bars for each model fit and are the minimum grid spacing, for the grid of LVG models used, necessary to increase χ^2 by a *minimum* of χ^2_{ν} . These formal errors are therefore very conservative estimates of the true formal errors.

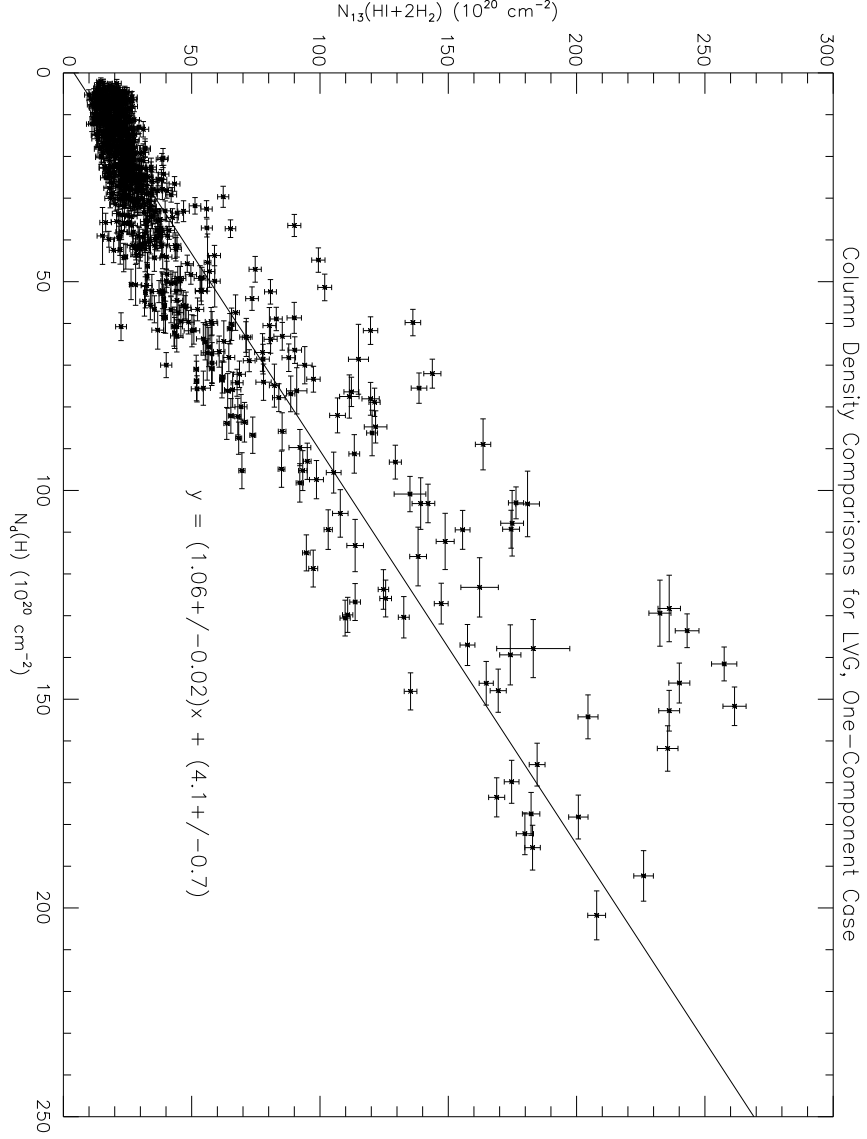


Fig. 17.— The plot above compares the gas column densities as derived from gas tracers and those derived from dust continuum emission for the case of non-LTE gas emission and a single component. The plot shows the gas column density as derived from $^{13}\text{CO } J = 1 \rightarrow 0$ using the results from the LVG method versus the gas column density as derived from the $140 \mu\text{m}$ and $240 \mu\text{m}$ continuum emission. The points in this plot represent the positions where $I_\nu(140 \mu\text{m})$, $I_\nu(240 \mu\text{m})$, and $I(^{13}\text{CO})$ are at more than $5\text{-}\sigma$, as in Figure 6.

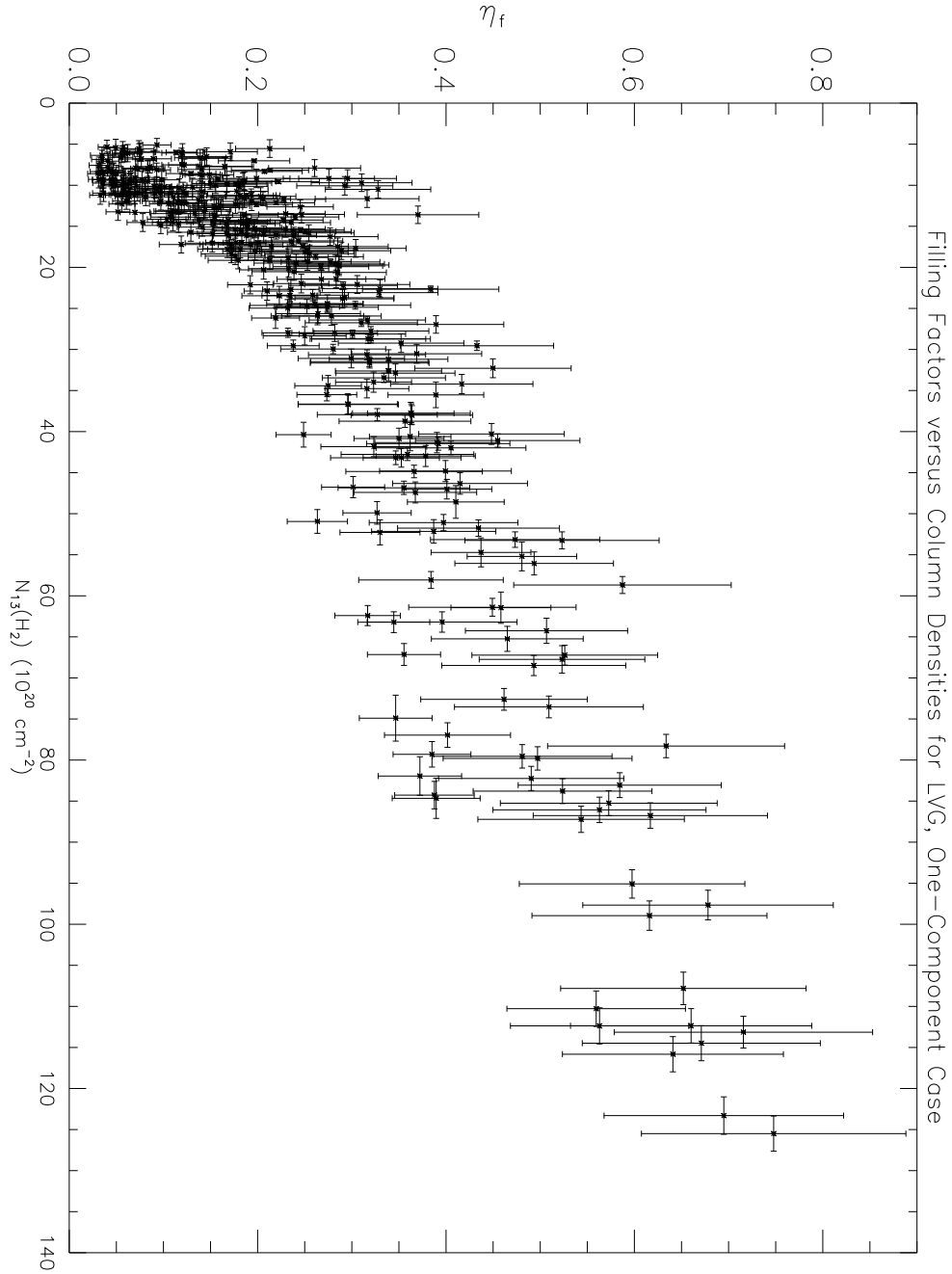


Fig. 18.— The area filling factors of substructures in the Orion clouds are plotted against the molecular gas column densities in the LVG, one-component case. The points in this plot represent the positions where $I_\nu(140 \mu\text{m})$, $I_\nu(240 \mu\text{m})$, and $I(^{13}\text{CO})$ are at more than $5\text{-}\sigma$ and where the peak radiation temperature of $^{12}\text{CO } J = 1 \rightarrow 0$ is at more than $3\text{-}\sigma$. This is a total of 372 points.

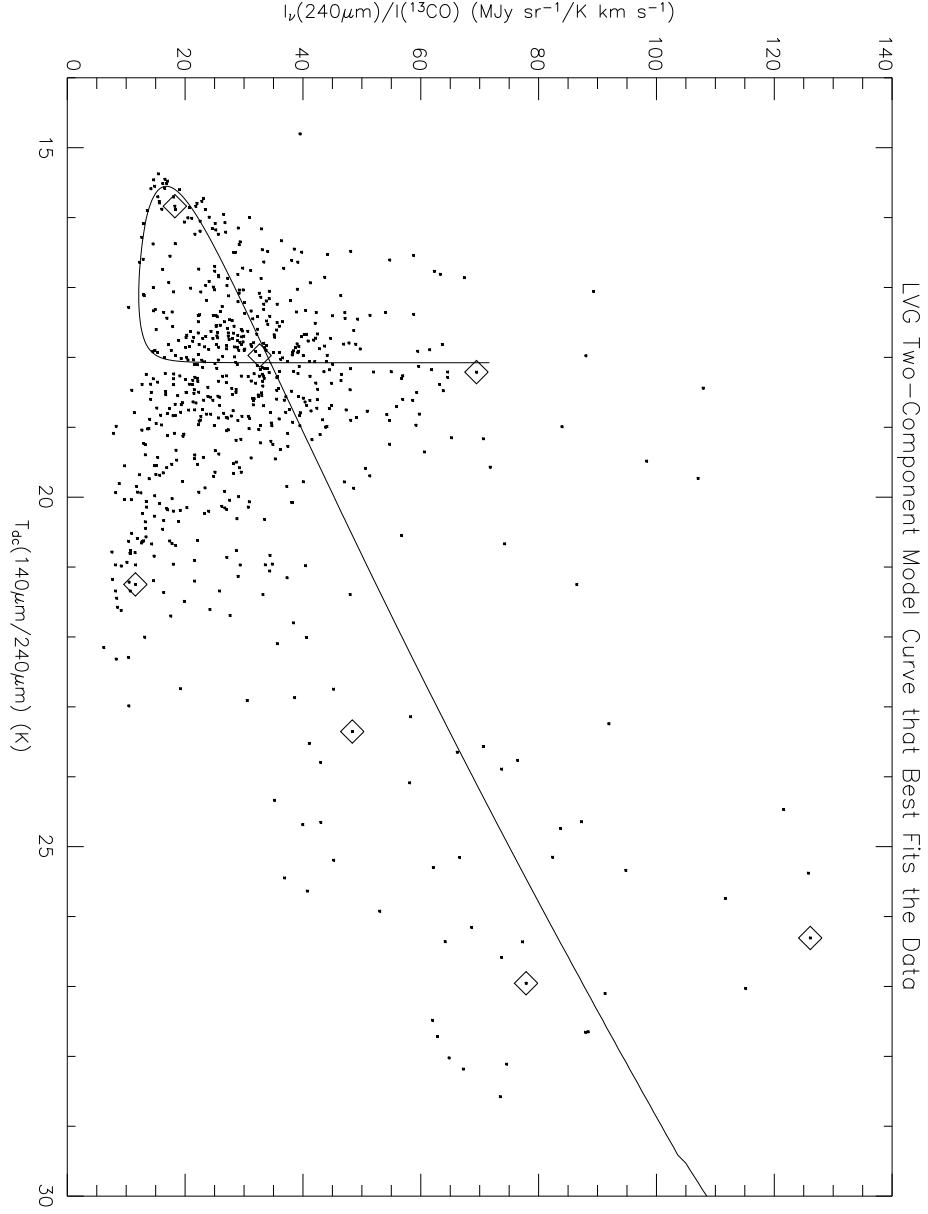


Fig. 19.— The model curve of r_{240} versus T_{dc} that best fits the data is shown for the non-LTE, two-component case. The plot includes the same data points as in Figure 6 with error bars excluded for clarity. The parameters and their values are listed in Table 1. The diamonds in this figure are the fiducial points discussed in Section 3.5 and listed in Table 3.

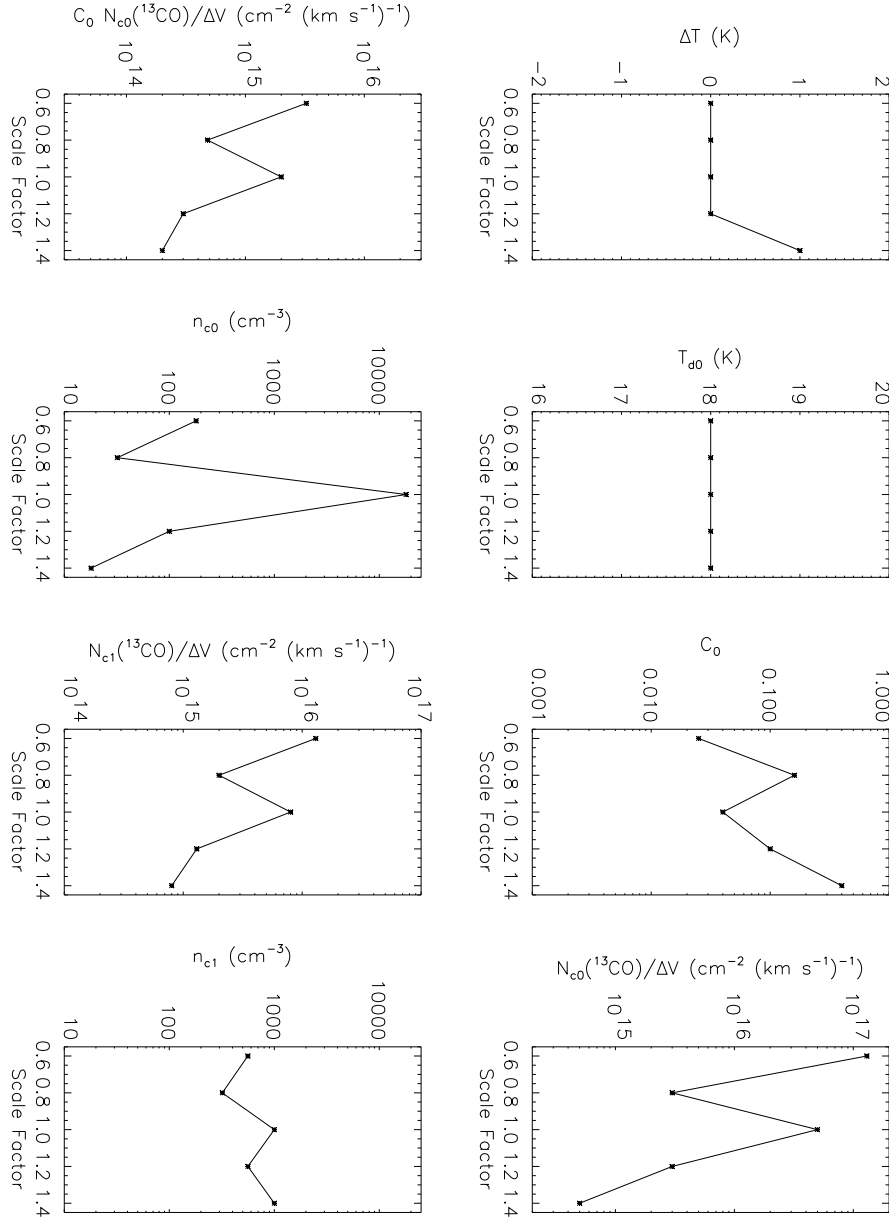


Fig. 20.— The effect of the systematic uncertainties on the resultant parameters from the fits of the two-component, LVG model curves is shown. The effect of these uncertainties was tested by applying the scale factors 0.6, 0.8, 1.0, 1.2, and 1.4 to the model curves and fitting the parameters for each scale factor. Except for the plots for ΔT and T_{d0} , all plots are semi-logarithmic where the vertical axes cover about the same logarithmic difference in range (about 3 orders of magnitude). This allows easy visual determination of which parameters have the smallest systematic uncertainties.

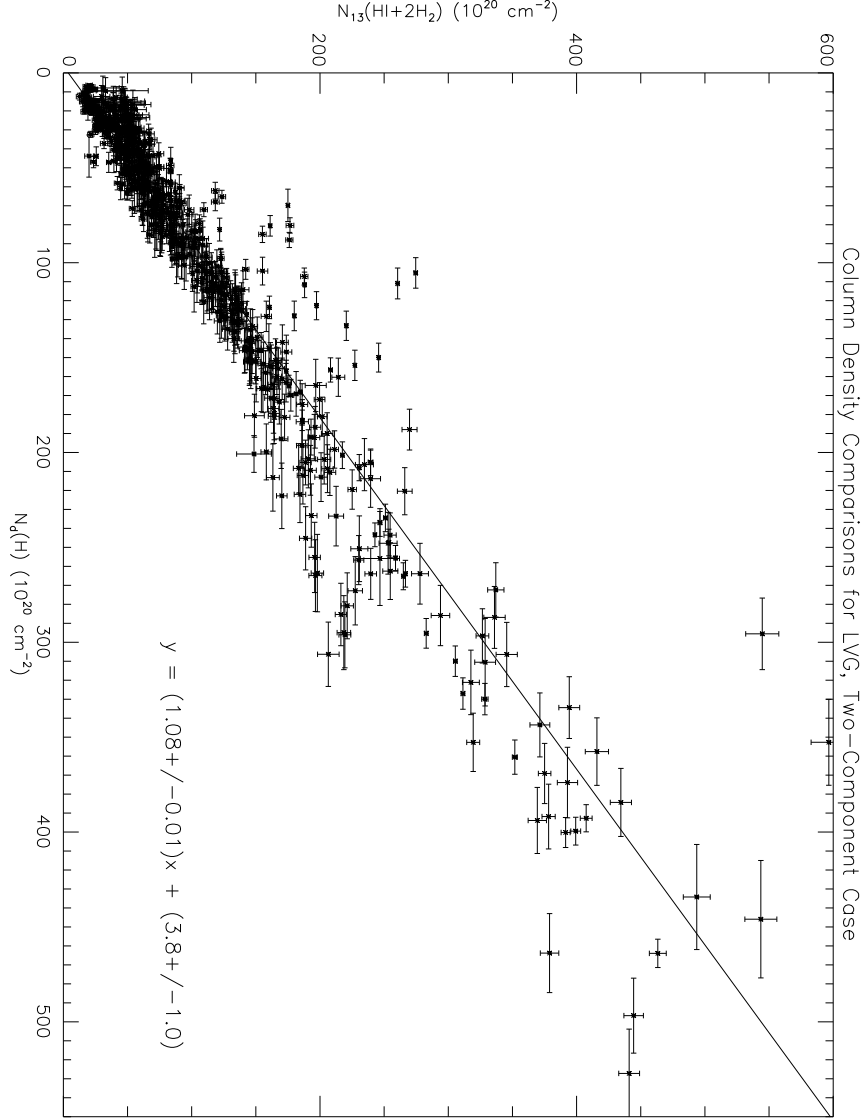


Fig. 21.— The plot above compares the gas column densities as derived from gas tracers and those derived from dust continuum emission for the case of non-LTE gas emission and two components. The plot shows the gas column density as derived from $^{13}\text{CO } J = 1 \rightarrow 0$ using the results from the LVG method versus the gas column density as derived from the $140 \mu\text{m}$ and $240 \mu\text{m}$ continuum emission. The points in this plot represent the positions where $I_{\nu}(140 \mu\text{m})$, $I_{\nu}(240 \mu\text{m})$, and $I(^{13}\text{CO})$ are at more than $5\text{-}\sigma$, as in Figure 6.

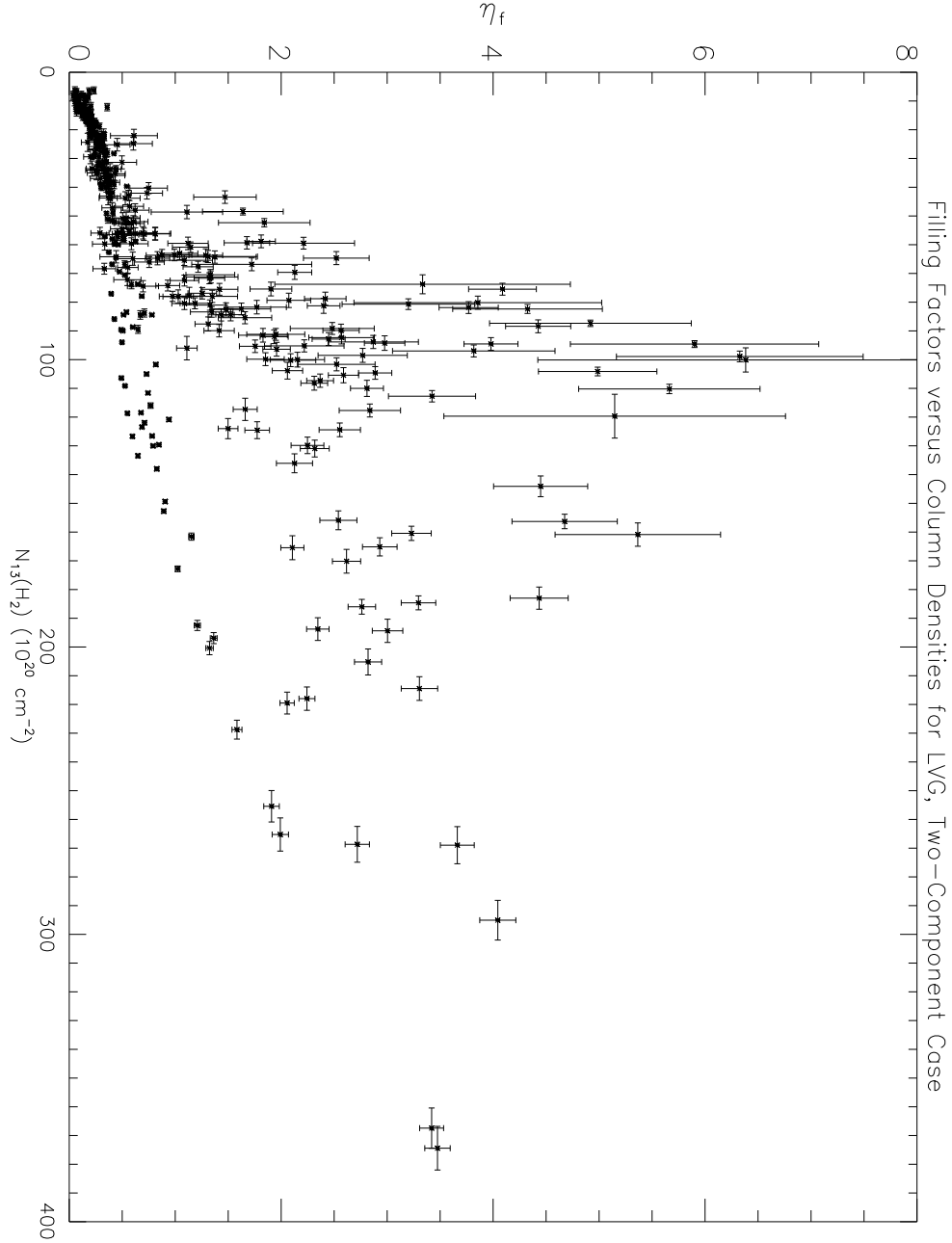


Fig. 22.— The area filling factors of substructures in the Orion clouds are plotted against the molecular gas column densities as computed in the LVG, two-component case. The points in this plot represent the positions where $I_\nu(140 \mu\text{m})$, $I_\nu(240 \mu\text{m})$, and $I(^{13}\text{CO})$ are at more than $5\text{-}\sigma$ and where the peak radiation temperature of $^{12}\text{CO } J = 1 \rightarrow 0$ is at more than $3\text{-}\sigma$. This is a total of 372 points.

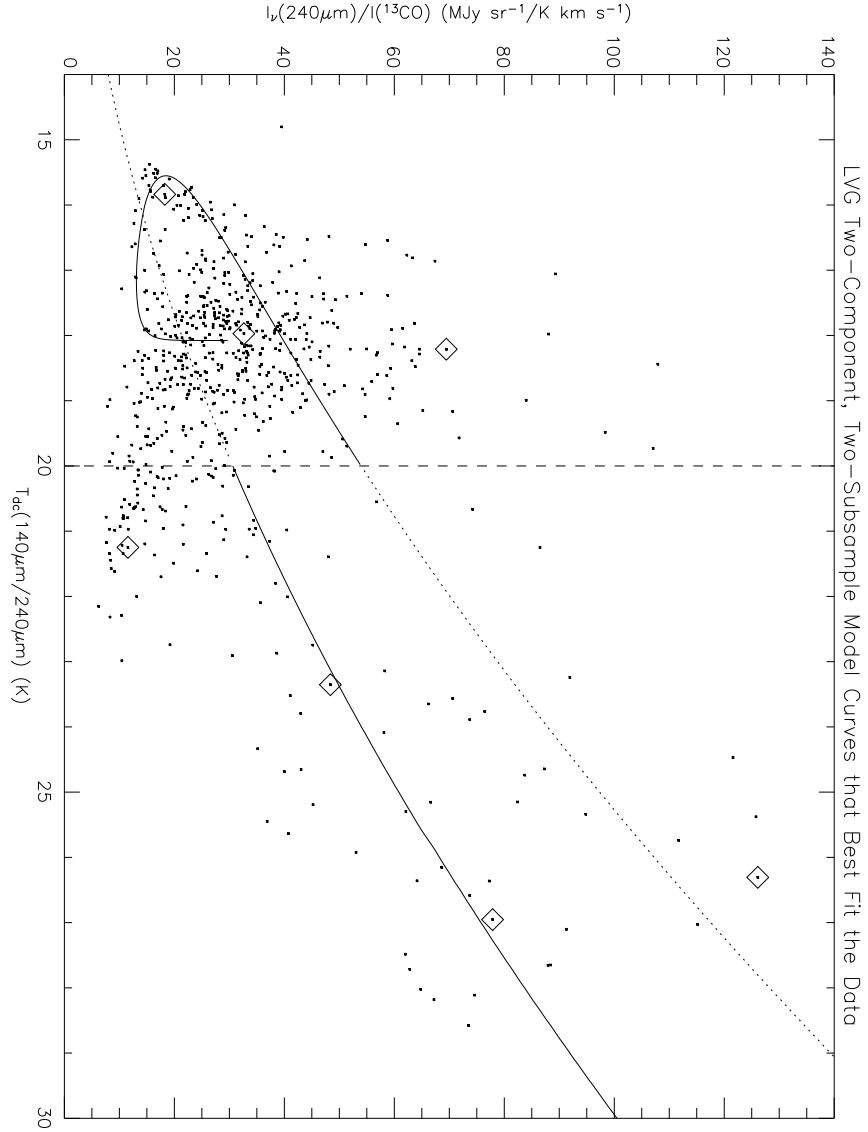


Fig. 23.— The model curves of r_{240} versus T_d that best fit the data are shown for the non-LTE, two-component, two-subsample case. The two solid curves represent fits to the $T_{dc} < 20$ K and $T_{dc} \geq 20$ K subsamples. The fit to the former is the curve from a LVG, two-component model with c_0 restricted to be ≥ 1 . The fit to the latter is an LVG, one component model with no such restriction. The dotted curves represent the extensions of the model curves across the $T_{dc} = 20$ K boundary, itself represented as a dashed line. The plot includes the same data points as in Figure 6 with error bars excluded for clarity. The parameters and their values are listed in Table 2. The diamonds in this figure are the fiducial points discussed in Section 3.5 and listed in Table 3.

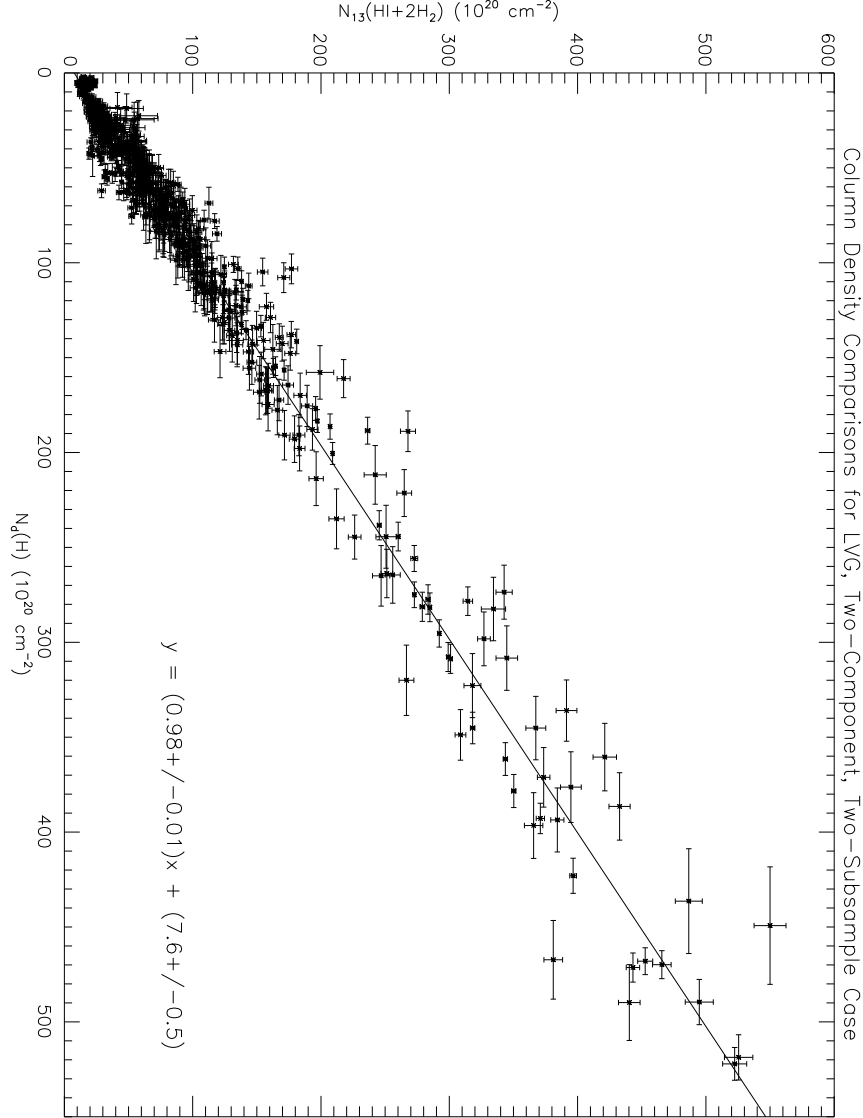


Fig. 24.— The plot above compares the gas column densities as derived from gas tracers and those derived from dust continuum emission for the case of non-LTE gas emission, two components, and two subsamples. The plot shows the gas column density as derived from the $^{13}\text{CO } J = 1 \rightarrow 0$ using the results from the LVG method versus the gas column density as derived from the $140 \mu\text{m}$ and $240 \mu\text{m}$ continuum emission. The points in this plot represent the positions where $I_\nu(140 \mu\text{m})$, $I_\nu(240 \mu\text{m})$, and $I(^{13}\text{CO})$ are at more than $5\text{-}\sigma$, as in Figure 6.

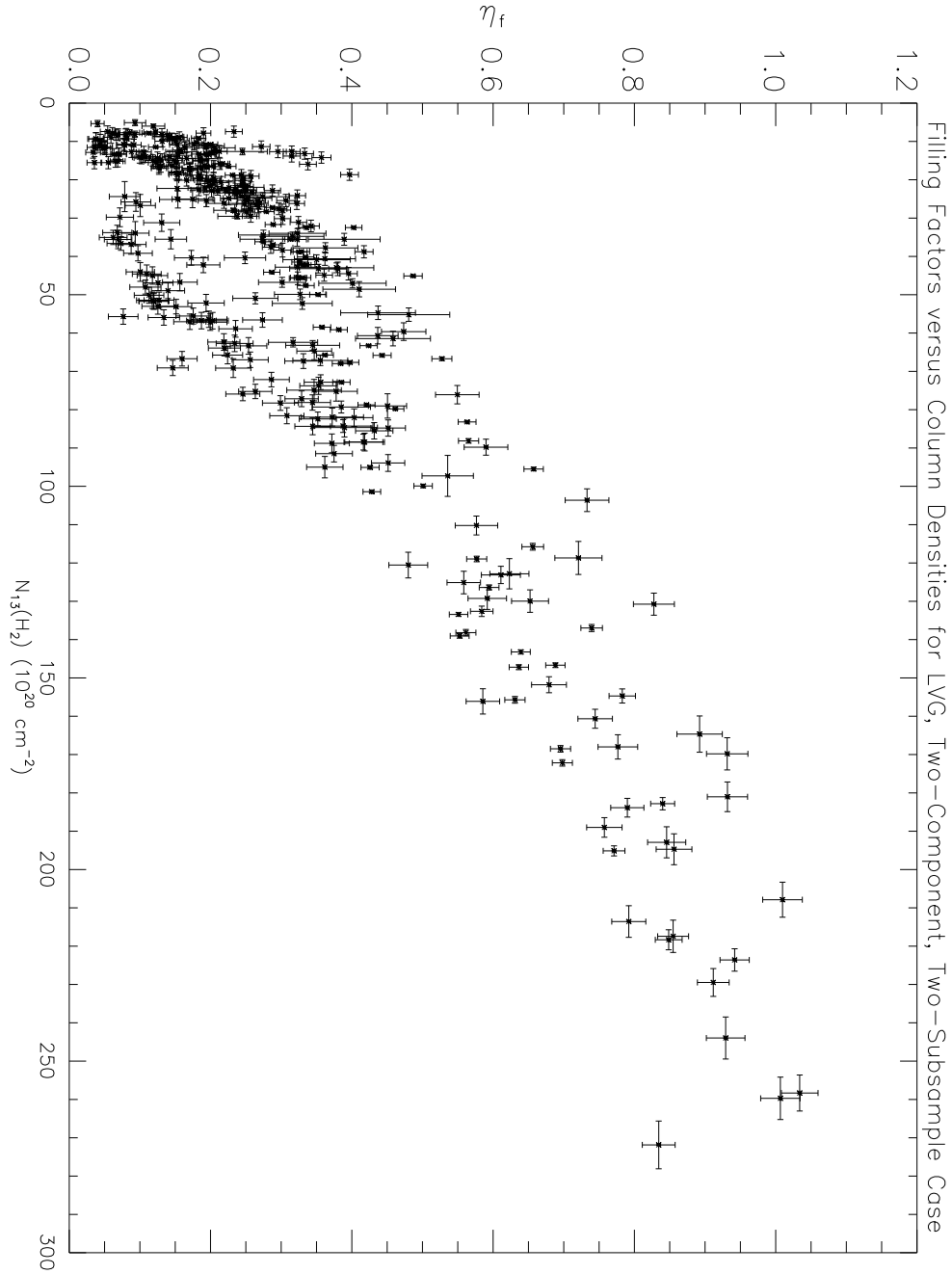


Fig. 25.— The area filling factors of substructures in the Orion clouds are plotted against the molecular gas column densities as computed in the LVG, two-component, two-subsample case. The points in this plot represent the positions where $I_\nu(140 \mu\text{m})$, $I_\nu(240 \mu\text{m})$, and $I(^{13}\text{CO})$ are at more than $5\text{-}\sigma$ and where the peak radiation temperature of $^{12}\text{CO } J = 1 \rightarrow 0$ is at more than $3\text{-}\sigma$. This is a total of 372 points.

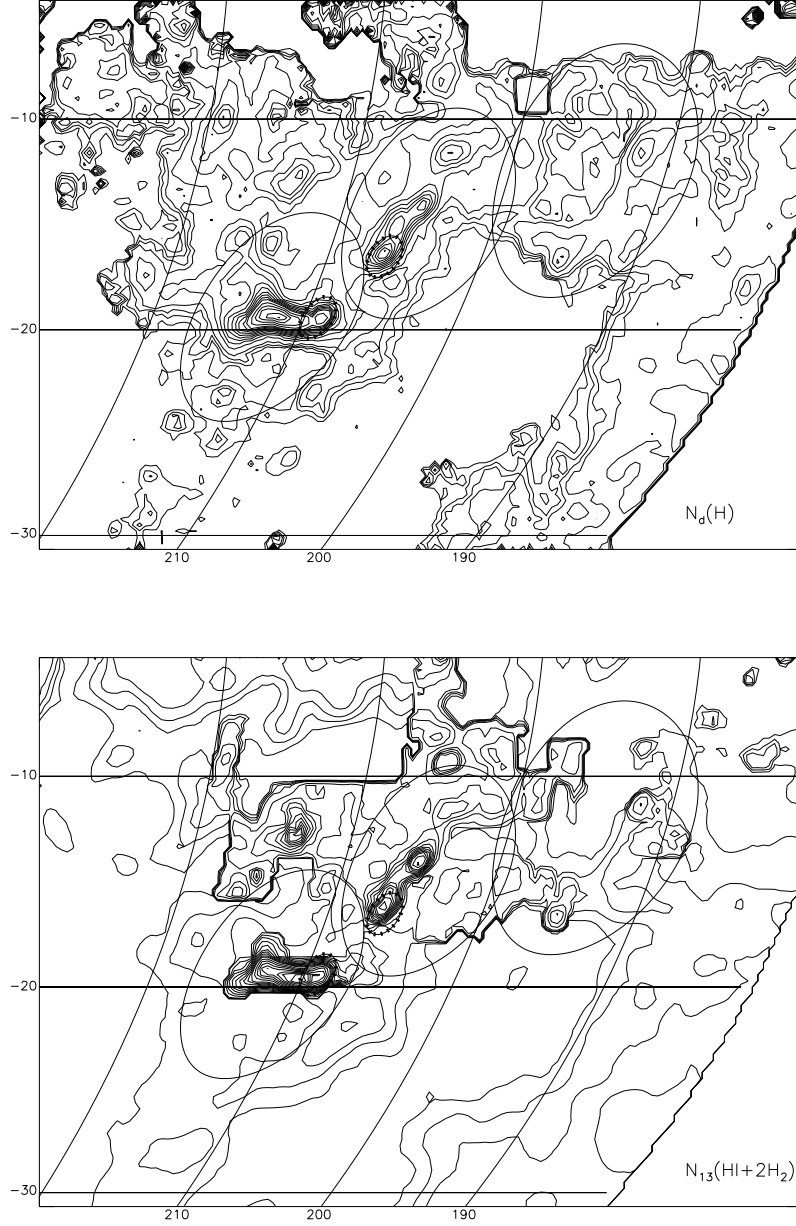


Fig. 26.— Contour maps of the column densities for the LVG, one-component case are shown above. The upper panel shows the map for the column densities derived from the $140\,\mu\text{m}$ and $240\,\mu\text{m}$ continuum observations. The contour levels are 3, 5, 7, 10, 20, 30,..., 100, 120, 140,..., 200 in units of $10^{20}\,H\,\text{nuclei}\cdot\text{cm}^{-2}$. The lower panel shows the map for the column densities derived from the $^{13}\text{CO}\,J=1\rightarrow 0$ and HI observations. The contour levels are 3, 5, 7, 10, 20, 30,..., 100, 120, 140,..., 240 in units of $10^{20}\,H\,\text{nuclei}\cdot\text{cm}^{-2}$.

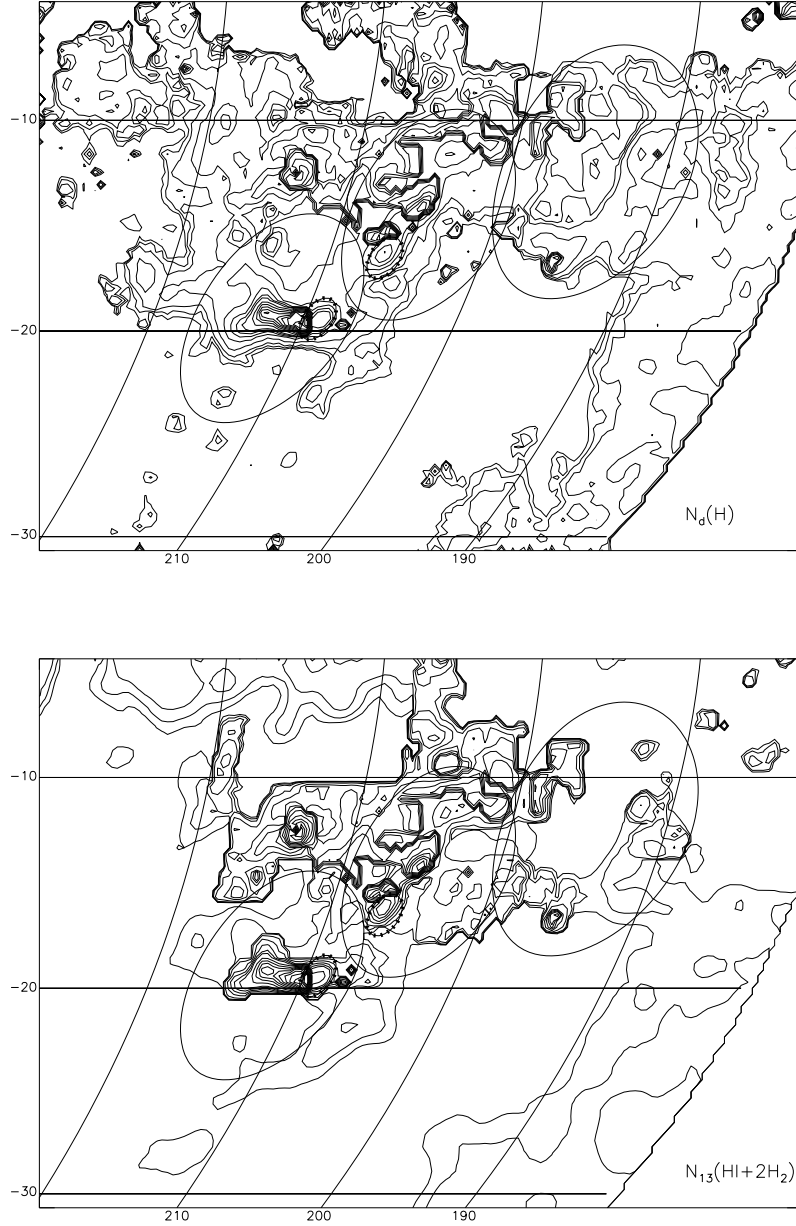


Fig. 27.— Contour maps of the column densities for the LVG, two-component, two-subsample case are shown above. The upper panel shows the map for the column densities derived from the 140 μm and 240 μm continuum observations. The lower panel shows the map for the column densities derived from the ^{13}CO $J = 1 \rightarrow 0$ and HI observations. The contour levels for both panels are 5, 7, 10, 20, 40, 60, 80, 100, 150, 200,..., 650 in units of $10^{20} \text{ H nuclei} \cdot \text{cm}^{-2}$.

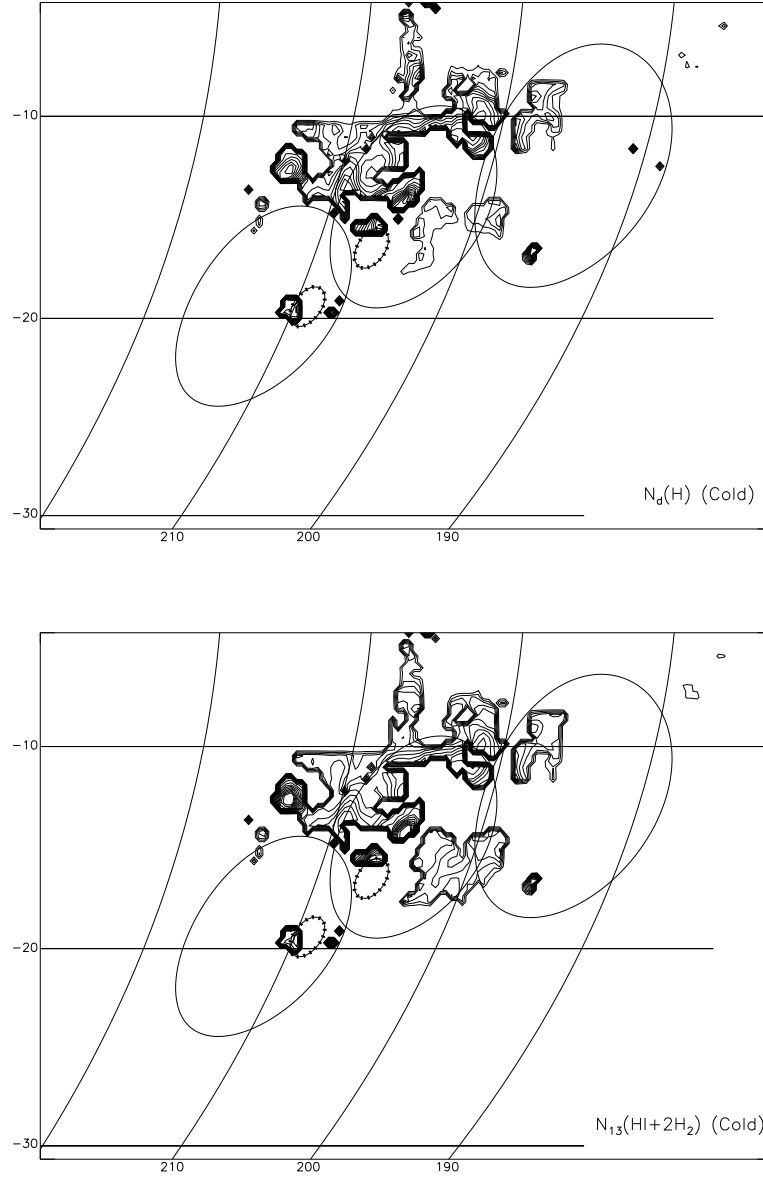


Fig. 28.— Contour maps of the column densities for the cold ($T_{d1} = T_{K1} \leq 10 \text{ K}$) dust and gas of component 1 in the LVG, two-component, two-subsample case are shown above. The upper panel shows the map for the column densities of the cold gas derived from the $140 \mu\text{m}$ and $240 \mu\text{m}$ continuum observations. The lower panel shows the map for the column densities of the cold gas derived from the $^{13}\text{CO } J = 1 \rightarrow 0$ observations. Along those lines of sight with this cold gas the HI column densities were also added. The contour levels for both panels are 10, 20, 30,..., 100, 120, 140,..., 200, 300, 400, 500 in units of $10^{20} H \text{ nuclei cm}^{-2}$.

Table 1. Two-Component Model Parameter Values.

Parameter	Best-Fit Value
ΔT	0 K
c_0	0.04
T_{d0}	18 K
$\frac{N_{c0}(^{13}\text{CO})}{\Delta v_c}$	$5 \times 10^{16} \text{ cm}^{-2} \cdot (\text{km} \cdot \text{s}^{-1})^{-1}$
n_{c0}	$1.8 \times 10^4 \text{ cm}^{-3}$
$\frac{N_{c1}(^{13}\text{CO})}{\Delta v_c}$	$8 \times 10^{15} \text{ cm}^{-2} \cdot (\text{km} \cdot \text{s}^{-1})^{-1}$
n_{c1}	$1 \times 10^3 \text{ cm}^{-3}$
χ^2_ν	5.69
ν	667

Note. — The *formal* uncertainties of ΔT and T_{d0} are both $\leq 3 \times 10^{-4}$ K. The *formal* relative uncertainties of the other parameters are $\leq 3 \times 10^{-4}$.

Table 2. Two-Component, Two-Subsample Model Parameter Values.

Parameter	Best-Fit Parameter Values	
	$T_{\text{dc}} < 20 \text{ K}$ Subsample	$T_{\text{dc}} \geq 20 \text{ K}$ Subsample
ΔT	0 K	$-3 \pm 4 \text{ K}$
c_0	1.0	—
T_{d0}	18 K	—
$\frac{N_{\text{c0}}(^{13}\text{CO})}{\Delta v_{\text{c}}}$	$5 \times 10^{15} \text{ cm}^{-2} \cdot (\text{km} \cdot \text{s}^{-1})^{-1}$	—
n_{c0}	$1.0 \times 10^5 \text{ cm}^{-3}$	—
$\frac{N_{\text{c1}}(^{13}\text{CO})}{\Delta v_{\text{c}}}$	$2 \times 10^{16} \text{ cm}^{-2} \cdot (\text{km} \cdot \text{s}^{-1})^{-1}$	$(3.2 \pm_{?}^{1.8}) \times 10^{15} \text{ cm}^{-2} \cdot (\text{km} \cdot \text{s}^{-1})^{-1}$
n_{c1}	$1 \times 10^5 \text{ cm}^{-3}$	$(5.6 \pm_{2.4}^{4.4}) \times 10^3 \text{ cm}^{-3}$
χ^2_{ν}	4.60	9.98
ν	525	139

Note. — The *formal* uncertainties of ΔT and T_{d0} for the $T_{\text{dc}} < 20 \text{ K}$ subsample are both $\leq 2 \times 10^{-4} \text{ K}$. The *formal* relative uncertainties of the other parameters for this subsample are $\leq 2 \times 10^{-4}$.

Table 3. Inferred Physical Conditions at the Fiducial Points^a

Coordinates ^a	Parameter ^b	Parameter Values ^c			
		Case 1 ^d	Case 2 ^d	Case 3 ^e	Case 4 ^e
15.84, 18.26	ΔT	−4	−1	0	0
	$N(^{13}\text{CO})/\Delta v$	—	3.2×10^{15}	$(2 \times 10^{15}) \ 8 \times 10^{15}$	$(2 \times 10^{14}) \ 5 \times 10^{15}$
	$n(\text{H}_2)$	—	1×10^5	$(1.8 \times 10^4) \ 1 \times 10^3$	$(1 \times 10^4) \ 5.6 \times 10^3$
	Distance	1.17	1.78	1.67	1.92
17.97, 32.65	Distance	0.72	1.06	0.31	0.93
18.21, 69.46	Distance	3.29	3.43	0.40	2.45
21.25, 11.56	ΔT	+9	−3	0	−3
	$N(^{13}\text{CO})/\Delta v$	—	3.2×10^{15}	$(2 \times 10^{15}) \ 8 \times 10^{15}$	3.2×10^{15}
	$n(\text{H}_2)$	—	5.6×10^3	$(1.8 \times 10^4) \ 1 \times 10^3$	5.6×10^3
	Distance	3.56	3.67	2.45	3.67
23.35, 48.37	Distance	0.99	0.47	5.52	0.47
26.31, 126.1	Distance	4.82	6.48	5.29	5.03
26.95, 77.87	Distance	0.88	0.45	1.71	1.05

^aAs depicted in the r_{240} versus T_d plots of Figures 6, 7, 8, 12, 13, 14, 15, ??, 19, and 23.

^b ΔT is in units of Kelvins, $N(^{13}\text{CO})/\Delta v$ is in units of $\text{cm}^{-2} \cdot (\text{km} \cdot \text{s}^{-1})^{-1}$, and $n(\text{H}_2)$ is in units of cm^{-3} . “Distance” is the orthogonal distance of the fiducial point from the theoretical curve in units of sigmas. The parenthesized quantities in Cases 3 and 4 are the parameter values for component 0. In particular, the parenthesized values for $N(^{13}\text{CO})/\Delta v$ are really the values for the product $c_0 * \frac{N_{\text{co}}(^{13}\text{CO})}{\Delta v_c}$.

^cThe parameter values for ΔT , $N(^{13}\text{CO})/\Delta v$, and $n(\text{H}_2)$ are not explicitly listed for some fiducial points. The parameter values for these points are the same as those of the points with the listed values [e.g. point (15.48, 18.26) or (21.25, 11.56)] that lie above the points without the listed values.

^dCase 1: LTE, one-component models. Case 2: LVG, one-component models.

^eCase 3: LVG, two-component models. Case 4: LVG, two-component, two-subsample models.

Table 4. Gas Masses Sampled by ^{13}CO , ^{12}CO , & HI (M_{\odot})

Field ^a	Case 1 ^b	Case 2 ^c	Case 3 ^d	Case 4 ^e	^{12}CO & HI ^f
Orion Nebula	21000	18000	35000	31000	20000
Orion A	88000	85000	146000	129000	122000
NGC 2024	10000	9100	18000	9200	17000
Orion B	93000	88000	248000	189000	104000
λ Orionis	38000	36000	92000	57000	45000
TOTAL ^g	220000	209000	486000	376000	271000

^aSee W96 for definitions of the fields.

^bUsing LTE, one-component models and observations of ^{13}CO and HI .

^cUsing LVG, one-component models and observations of ^{13}CO and HI .

^dUsing LVG, two-component models and observations of ^{13}CO and HI .

^eUsing LVG, two-component, two-subsample models and observations of ^{13}CO and HI .

^fAdopting an X-factor of $2.6 \times 10^{20} \text{ cm}^{-2} \cdot (\text{K} \cdot \text{km} \cdot \text{s}^{-1})^{-1}$.

^gSum of Orion A, Orion B, λ Orionis fields.

Table 5. Gas Masses Inferred from 140, 240 μm Continuum Emission (M_{\odot})

Field ^a	Cases 1 & 2 ^b	Case 3 ^c	Case 4 ^d
Orion Nebula	14000	29000	27000
Orion A	107000	169000	151000
NGC 2024	9700	14000	9700
Orion B	81000	225000	179000
λ Orionis	63000	122000	82000
TOTAL ^e	251000	516000	411000

^aSee W96 for definitions of the fields.

^bUsing one-component models and continuum observations.

^cUsing two-component models and continuum observations.

^dUsing two-component, two-subsample models and continuum observations.

^eSum of Orion A, Orion B, λ Orionis fields.

Table 6. Best Estimates of Total^a Gas Masses (M_{\odot})

Tracer	One-Component Case ^b	Two-Component Case ^c
Derived from Continuum	251000	411000
Derived from $^{13}\text{CO } J = 1 \rightarrow 0^{\text{d}}$	263000	429000

^aThe total *hydrogen* mass from the 3 big fields (i.e., sum of Orion A, Orion B, λ Orionis fields).

^bUsing LVG, one-component models.

^cUsing LVG, two-component, two-subsample models.

^dAfter correcting for insufficient coverage.

Table 7. Masses^a of Gas in a Cold ($T_K \leq 10$ K) Component (M_\odot)

Field ^b	Case 3 ^c	Case 4 ^d
Orion Nebula	14000	14000
Orion A	43000	28000
NGC 2024	5700	6600
Orion B	155000	126000
λ Orionis	54000	28000
TOTAL ^e	252000	181000

^aInferred from ^{13}CO and H I observations.

^bSee W96 for definitions of the fields.

^cUsing LVG, two-component models and observations of ^{13}CO and H I.

^dUsing LVG, two-component, two-subsample models and observations of ^{13}CO and H I.

^eSum of Orion A, Orion B, λ Orionis fields.